

| | | | | | |
|---|-------------------|-----------------------------|---|-----------------------------------|--|
| REPORT DOCUMENTATION PAGE | | | Form Approved OMB NO. 0704-0188 | | |
| <p>The public reporting burden for this collection of information is estimated to average 1 hour per response, including the time for reviewing instructions, searching existing data sources, gathering and maintaining the data needed, and completing and reviewing the collection of information. Send comments regarding this burden estimate or any other aspect of this collection of information, including suggestions for reducing this burden, to Washington Headquarters Services, Directorate for Information Operations and Reports, 1215 Jefferson Davis Highway, Suite 1204, Arlington VA, 22202-4302. Respondents should be aware that notwithstanding any other provision of law, no person shall be subject to any penalty for failing to comply with a collection of information if it does not display a currently valid OMB control number.</p> <p>PLEASE DO NOT RETURN YOUR FORM TO THE ABOVE ADDRESS.</p> | | | | | |
| 1. REPORT DATE (DD-MM-YYYY) 10-08-2015 | | 2. REPORT TYPE MS Thesis | | 3. DATES COVERED (From - To) - | |
| 4. TITLE AND SUBTITLE Effect of Material Ion Exchanges on the Mechanical Stiffness Properties and Shear Deformation of Hydrated Cement Material Chemistry Structure C-S-H Jennit - A Computational Modeling Study | | | 5a. CONTRACT NUMBER W911NF-11-2-0043 | | |
| | | | 5b. GRANT NUMBER | | |
| | | | 5c. PROGRAM ELEMENT NUMBER 611104 | | |
| 6. AUTHORS Babatunde Adebisi | | | 5d. PROJECT NUMBER | | |
| | | | 5e. TASK NUMBER | | |
| | | | 5f. WORK UNIT NUMBER | | |
| 7. PERFORMING ORGANIZATION NAMES AND ADDRESSES North Carolina A&T State University 1601 East Market Street Greensboro, NC 27411 -0001 | | | 8. PERFORMING ORGANIZATION REPORT NUMBER | | |
| 9. SPONSORING/MONITORING AGENCY NAME(S) AND ADDRESS (ES) U.S. Army Research Office P.O. Box 12211 Research Triangle Park, NC 27709-2211 | | | 10. SPONSOR/MONITOR'S ACRONYM(S) ARO | | |
| | | | 11. SPONSOR/MONITOR'S REPORT NUMBER(S) 59544-MA-PIR.23 | | |
| 12. DISTRIBUTION AVAILABILITY STATEMENT Approved for public release; distribution is unlimited. | | | | | |
| 13. SUPPLEMENTARY NOTES The views, opinions and/or findings contained in this report are those of the author(s) and should not be construed as an official Department of the Army position, policy or decision, unless so designated by other documentation. | | | | | |
| 14. ABSTRACT Material properties and performance are governed by material molecular chemistry structures and molecular level interactions. Methods to understand relationships between the material properties and performance and their correlation to the molecular level chemistry and morphology, and thus find ways of manipulating and adjusting matters at the atomistic level in order to improve material performance are required. A computational material modeling methodology is investigated and demonstrated for a key cement hydrated component material chemistry structure of Calcium Silicate Hydrate (C-S-H) Jennite in this work. | | | | | |
| 15. SUBJECT TERMS Material chemistry, Calcium Silicate Hydrate, Magnesium Ion Exchange, Mechanical Stiffness Modulus, Shear deformation and failure | | | | | |
| 16. SECURITY CLASSIFICATION OF: | | | 17. LIMITATION OF ABSTRACT UU | 15. NUMBER OF PAGES | 19a. NAME OF RESPONSIBLE PERSON Ram Mohan |
| a. REPORT UU | b. ABSTRACT UU | c. THIS PAGE UU | | | 19b. TELEPHONE NUMBER 336-285-2867 |

Report Title

Effect of Material Ion Exchanges on the Mechanical Stiffness Properties and Shear Deformation of Hydrated Cement Material Chemistry Structure C-S-H Jennit - A Computational Modeling Study

ABSTRACT

Material properties and performance are governed by material molecular chemistry structures and molecular level interactions. Methods to understand relationships between the material properties and performance and their correlation to the molecular level chemistry and morphology, and thus find ways of manipulating and adjusting matters at the atomistic level in order to improve material performance are required. A computational material modeling methodology is investigated and demonstrated for a key cement hydrated component material chemistry structure of Calcium-Silicate-Hydrate (C-S-H) Jennite in this work.

The effect of material ion exchanges on the mechanical stiffness properties and shear deformation behavior of hydrated cement material chemistry structure of Calcium Silicate Hydrate (C-S-H) Jennite was studied. Calcium ions were replaced with Magnesium ions in Jennite structure of the C-S-H gel. Different level of substitution of the ions was used. The traditional Jennite structure was obtained from the American Mineralogist Crystal Structure Database and super cells of the structures were created using a Molecular Dynamics Analyzer and Visualizer Material Studio. Molecular dynamics parameters used in the modeling analysis were determined by carrying out initial dynamic studies. 64 unit cell of C-S-H Jennite was used in material modeling analysis studies based on convergence results obtained from the elastic modulus and total energies. NVT forcite dynamics using compass force field based on 200 ps dynamics time was used to determine mechanical modulus of the traditional C-S-H gel and the Magnesium ion modified structures. NVT Discover dynamics and COMPASS forcefield was used in the material modeling studies to investigate the influence of ionic exchange on the shear deformation of the associated material chemistry structures. A prior established quasi-static deformation method to emulate shear deformation of C-S-H material chemistry structure that is based on a triclinic crystal structure was used, by deforming the triclinic crystal structure at 0.2 degree per time step for 75 steps of deformation.

It was observed that there is a decrease in the total energies of the systems as the percentage of magnesium ion increases in the C-S-H Jennite molecular structure systems. Investigation of effect of ion exchange on the elastic modulus shows that the elastic stiffness modulus tends to decrease as the amount of Mg in the systems increases, using either compass or universal force field. On the other hand, shear moduli obtained after deforming the structures computed from the stress-strain curve obtained from material modeling increases as the amount of Mg increases in the system. The present investigations also showed that ultimate shear stress obtained from predicted shear stress – strain also increases with amount of Mg in the chemistry structure. Present study clearly demonstrates that computational material modeling following molecular dynamics analysis methodology is an effective way to predict and understand the effective material chemistry, and additive changes on the stiffness and deformation characteristics in cementitious materials and extendable to others.

Effect of Material Ion Exchanges on the Mechanical Stiffness Properties and Shear
Deformation of Hydrated Cement Material Chemistry Structure C-S-H Jennite – A
Computational Modeling Study

Babatunde Matthew Adebisi
North Carolina A&T State University

A thesis submitted to the graduate faculty
in partial fulfillment of the requirements for the degree of

MASTER OF SCIENCE

Department: Nanoengineering

Major: Nanoengineering

Major Professor: Dr. Ram Mohan

Greensboro, North Carolina

2014

The Graduate School
North Carolina Agricultural and Technical State University
This is to certify that the Master's Thesis of

Babatunde Matthew Adebisi

has met the thesis requirements of
North Carolina Agricultural and Technical State University

Greensboro, North Carolina
2014

Approved by:

Dr. Ram Mohan
Major Professor

Dr. Albert Hung
Committee Member

Dr. Lifeng Zhang
Committee Member

Dr. John Rivas
Committee Member

Dr. Ajit Kelkar
Department Chair

Dr. Sanjiv Sarin
Dean, The Graduate School

© Copyright by

Babatunde Matthew Adebisi

2014

Biographical Sketch

Babatunde Matthew Adebisi was born in Lagos, Nigeria. He epitomizes the symbol of hard work and diligence. He had his first degree from the Obafemi Awolowo University, Ile-Ife, where he graduated with a first class honors in Chemical Engineering. He then proceeded to work as a Project Engineer with Exxon Mobil, and as a Miller with Honeywell Groups in Nigeria.

His quest for knowledge brought him to North Carolina Agricultural and Technical State University to continue his graduate studies in Nanoengineering. Besides this, he is an entrepreneur, and has also pioneered several business endeavors. He is the first graduate of the professional future leadership program jointly organized by the University of North Carolina – Greensboro and North Carolina A&T State University. He is a 6-Sigma greenbelt holder and a stickler to quality work. He loves to play golf and soccer and also loves teaching and the things of God.

Dedication

This work is dedicated to God almighty the giver of life and strength. It is also dedicated to my parents Mr. and Mrs. Olajide Adebiyi for their unconditional love and prayers.

Acknowledgments

I will like to use this opportunity to acknowledge all those who have contributed to the success of my program. I will like to thank my advisor Dr. Ram Mohan for his relentless effort, and input in making sure the research is completed. To Dr. John Rivas for always proffering solutions to my several questions and Dr. Mohamed for his initial input that brought me up to speed in my research; My host families; Mr. and Mrs. Yekini Olatunji, the Oresanya family and Mr. and Mrs. Olanrewaju Ogedengbe. I will also like to acknowledge my friends, Ayo Ajinola, Jubril Davies, Bolaji Adesanya and Timothy Adekoya and Blessing Ihedioha for making me feel at home. Special thanks go to Mr. Wayne Hodo, Research Engineer, Engineering Research and Development Center (ERDC) for his perspectives and insight on material chemistry level changes with magnesium in traditional cement for specialized applications.

In addition, I will like to appreciate my parents and my sisters; Keji, Funmilola, Taiwo and Kehinde Adebisi for believing in me and for their prayers and patience without which I will not be able to achieve this feat.

The financial support for this work by the U.S. Army Research Office under a cooperative agreement award contract number W911NF-11-2-0043 (Program Manager: Dr. Joseph Myers; Co-CAM: Mr. Wayne Hodo, ERDC). Discussions with other researchers at Engineering Research and Development Center, Vicksburg, MS, and U. S. Army Research Laboratory are greatly acknowledged. In addition, support of Joint School of Nanoscience and Nanoengineering is acknowledged.

Table of Contents

| | |
|---|----|
| List of Figures | x |
| List of Tables | xv |
| Abstract | 1 |
| 1 CHAPTER 1 Introduction | 3 |
| 1.1 Cement: Evolution of Material Chemistry | 3 |
| 1.2 Cement: Multi-Scale Nature | 6 |
| 1.3 Objectives | 8 |
| 1.4 Computational Modeling | 10 |
| 2 CHAPTER 2 Computational Modeling Methods – Background | 11 |
| 2.1 Molecular Dynamics Techniques | 11 |
| 2.2 Force Field/Interatomic Potential | 13 |
| 2.2.1 Universal force field (UFF) | 16 |
| 2.2.2 COMPASS force field (COMPASS) | 17 |
| 2.3 Ensembles and Controls | 17 |
| 2.3.1 Andersen thermostat | 18 |
| 2.3.2 Velocity scaling | 18 |
| 2.3.3 <i>Nosé</i> thermostat | 19 |
| 2.3.4 Berendsen thermostat | 19 |
| 2.3.5 Andersen barostat | 20 |
| 2.3.6 Parinelo barostat | 20 |
| 2.3.7 Berendsen barostat | 20 |
| 2.4 Energy Minimization | 21 |
| 2.5 Time Integration Method | 21 |

| | | |
|---------|---|----|
| 2.6 | Periodic Boundary Condition | 22 |
| 2.7 | Dynamic Simulations and Post-Analysis of Physical Quantities | 23 |
| 2.8 | Predictive Mechanical Properties | 25 |
| 2.9 | Estimation of Material Property Based on Deformation and Stress-Strain Behavior | 27 |
| 3 | CHAPTER 3 Computational Material Modeling Analysis of C-S-H Jennite | 30 |
| 3.1 | Software Analysis Codes for Molecular Dynamics Modeling | 30 |
| 3.2 | C-S-H Gel | 30 |
| 3.2.1 | Jennite..... | 31 |
| 3.3 | Molecular Dynamics Modeling Process..... | 32 |
| 3.3.1 | Molecular Structural Magnesium Exchange Approach. | 33 |
| 3.4 | Parameter Determination Analysis | 36 |
| 3.4.1 | Dynamic time average..... | 36 |
| 3.4.1.1 | Determination of dynamic time..... | 36 |
| 3.4.2 | Thermodynamic temperature and pressure control. | 39 |
| 3.4.2.1 | Determination of temperature control method..... | 39 |
| 3.4.2.2 | Determination of dynamic pressure control method..... | 40 |
| 3.4.3 | Material system size. | 42 |
| 3.4.3.1 | Determination of material system size..... | 42 |
| 3.4.4 | Influence of forcefield. | 45 |
| 3.4.5 | MD parameters summary. | 47 |
| 4 | CHAPTER 4 Results and Discussions | 48 |
| 4.1 | Elastic Stiffness Modulus | 48 |
| 4.1.1 | Mechanical properties summary..... | 54 |
| 4.2 | Shear Deformation..... | 55 |

| | |
|--|-----|
| 4.2.1 Shear deformation, <i>cb</i> -plane..... | 58 |
| 4.2.2 Shear deformation, <i>ba</i> -plane. | 62 |
| 4.2.3 Shear deformation, <i>ac</i> -plane..... | 65 |
| 4.2.4 Shear deformation analysis results summary. | 68 |
| 4.3 Shear Deformation Atom Trajectory Study..... | 69 |
| 5 CHAPTER 5 Discussion and Future Research..... | 80 |
| 5.1 Discussion of Results..... | 80 |
| 5.2 Recommendations for Future Work | 81 |
| References..... | 82 |
| Appendix A1 | 88 |
| Appendix A2..... | 90 |
| Appendix A3..... | 92 |
| Appendix B1 | 96 |
| Appendix B2 | 98 |
| Appendix C1 | 100 |
| Appendix C2 | 104 |

List of Figures

| | |
|--|----|
| Figure 1. Schematics of multi-scale material structure of cement-based materials..... | 7 |
| Figure 2. Multiscale nature of cement-based materials. | 7 |
| Figure 3. Atomic positions and interaction forces on a 3-atom system..... | 12 |
| Figure 4. Bonded and unbonded interactions. | 14 |
| Figure 5. Molecular dynamics process. | 15 |
| Figure 6. Time average. Quantities of interest are obtained as average over a dynamic time. | 15 |
| Figure 7. Typical stress-strain response..... | 27 |
| Figure 8. Shear deformation | 29 |
| Figure 9. Jennite structure..... | 32 |
| Figure 10. MD material modeling process | 33 |
| Figure 11. Traditional and modified Jennite structures. | 35 |
| Figure 12. Total energy versus simulation time - Nosé thermostat | 37 |
| Figure 13. Total energy versus simulation time - Andersen thermostat | 38 |
| Figure 14. Total energy versus simulation time - Velocity Scale thermostat | 38 |
| Figure 15. Total energy versus simulation time – Berendsen thermostat..... | 39 |
| Figure 16. Total energy versus simulation time - Parinelo barostat | 40 |
| Figure 17. Total energy versus simulation time – Andersen barostat..... | 41 |
| Figure 18. Total energy versus simulation time - Berendsen barostat..... | 41 |
| Figure 19. Material system sizes, 1, 8 and 64 unit cells of a Mg modified Jennite | 42 |
| Figure 20. Normalized average total energy for traditional C-S-H structures: 1, 8, 27, 64, 125 unit cells | 43 |

| | |
|--|----|
| Figure 21. Normalized average total energy for 55%Mg modified structures: 1, 8, 27, 64, 125 unit cells | 43 |
| Figure 22. Elastic stiffness modulus (Hill average) for traditional C-S-H structures: 1, 8, 27, 64 and 125 unit cells. | 44 |
| Figure 23. Elastic stiffness modulus (Hill average) for 55%Mg Modified C-S-H structures: 1, 8, 27 and 64 unit cells | 44 |
| Figure 24. Total energy profile for 64 unit cell traditional and modified Jennite (55%Mg) using COMPASS and universal forcefields. | 45 |
| Figure 25. Total energy profile for 64 unit cell traditional and modified Jennite (33%Mg) using COMPASS and UNIVERSAL forcefields. | 46 |
| Figure 26. Total energy profile for 64 unit cell traditional and modified Jennite (83%Mg) using COMPASS and universal forcefields. | 47 |
| Figure 27. Initial and final Jennite structures – Traditional and Mg Ion Exchanged C-S-H..... | 48 |
| Figure 28. Change in total energy per mole for various Mg ion exchange percentages..... | 49 |
| Figure 29. Predicted elastic modulus (Hill Average) for various Mg ion exchange percentages of 64 unit cell C-S-H Jennite structures-COMPASS forcefield..... | 50 |
| Figure 30. Total energy per mole for various Mg ion exchange percentages..... | 51 |
| Figure 31. Predicted elastic modulus (Hill Average) for various Mg ion exchange with the variants and associated errors-COMPASS forcefield..... | 51 |
| Figure 32. Predicted elastic modulus (Hill Average) for various Mg ion exchange percentages of 64 unit cell C-S-H Jennite structures-Universal forcefield..... | 52 |
| Figure 33. Predicted shear modulus (Hill Average) variations for various magnesium ion exchange percentages studied. | 53 |

| | |
|---|----|
| Figure 34. Predicted bulk modulus (Hill Average) variations for various magnesium ion exchange percentages studied. | 53 |
| Figure 35. Predicted Poisson ratio (Hill Average) variations for various Magnesium ion exchange percentage studied..... | 54 |
| Figure 36. Shear deformation modeling along three crystallographic planes of triclinic C-S-H structure..... | 56 |
| Figure 37. MD implementation of shear deformation. Showing an NPT relaxation of the initial structure, followed by an incremental angular change - the deformation step, corresponding NVT equilibration of the deformed structure to obtained the shear stress of the deformed structure and continuation of the iterative process. | 57 |
| Figure 38. Predicted Shear Stress-strain deformation behavior for shearing along the cb-plane for traditional Jennite. Ref [50] | 58 |
| Figure 39 . Predicted Shear Stress-strain deformation behavior for shearing along the cb-plane for 33% magnesium modified Jennite | 59 |
| Figure 40. Predicted Shear Stress-strain deformation behavior for shearing along the cb-plane for 83% magnesium modified Jennite | 59 |
| Figure 41. Shear Modulus variations due to Mg Ion Exchange, cb-plane..... | 61 |
| Figure 42. Ultimate shear stress variations due to Mg Ion Exchange, cb-plane..... | 61 |
| Figure 43. Predicted Shear Stress-strain deformation behavior for shearing along the <i>ba</i> -plane for traditional Jennite. Ref [50] | 62 |
| Figure 44. Predicted Shear Stress-strain deformation behavior for shearing along the <i>ba</i> -plane for 33% magnesium modified Jennite | 63 |

| | |
|--|----|
| Figure 45. Predicted Shear Stress-strain deformation behavior for shearing along the ba-plane for 83% magnesium modified Jennite | 63 |
| Figure 46. Shear Modulus variations due to Mg Ion Exchange, ba-plane..... | 64 |
| Figure 47. Ultimate shear stress variations due to Mg Ion Exchange, ba-plane..... | 64 |
| Figure 48. Predicted Shear Stress-strain deformation behavior for shearing along the ac-plane for traditional Jennite. Ref [50] | 65 |
| Figure 49. Predicted Shear Stress-strain deformation behavior for shearing along the ac-plane for 33% magnesium modified Jennite..... | 66 |
| Figure 50. Predicted Shear Stress-strain deformation behavior for shearing along the ac-plane for 83% magnesium modified Jennite | 66 |
| Figure 51. Shear Modulus variations due to Mg Ion Exchange, ac-plane..... | 67 |
| Figure 52. Ultimate shear stress variations due to Mg Ion Exchange, ac-plane..... | 67 |
| Figure 53. Atomic Centroid Displacement-Strain Curves for Layers 3-6 along x-axis for Traditional Jennite when sheared along ba-plane..... | 71 |
| Figure 54. Atomic Centroid Displacement-Strain Curves for Layers 7-10 along x-axis for Traditional Jennite when sheared along ba-plane..... | 72 |
| Figure 55. Stress-Strain Curve for Traditional Jennite when sheared along the ba-Plane | 73 |
| Figure 56. Atomic Centroid Displacement-Strain Curves for Layers 3-6 along x-axis for 33% Magnesium Modified Jennite when sheared along ba-plane..... | 74 |
| Figure 57. Atomic Centroid Displacement-Strain Curves for Layers 7-10 along x-axis for 33% Magnesium Modified Jennite when sheared along ba-plane..... | 75 |
| Figure 58. Stress-Strain Curve for 33% Mg Modified Jennite when sheared along the ba-Plane | 76 |

| | |
|---|----|
| Figure 59. Atomic Centroid Displacement-Strain Curves for Layers 3-6 along x-axis for 83% Magnesium Modified Jennite when sheared along ba-plane | 77 |
| Figure 60. Atomic Centroid Displacement-Strain Curves for Layers 7-10 along x-axis for 83% Magnesium Modified Jennite when sheared along ba-plane | 78 |
| Figure 61. Stress-Strain Curve for 83% Mg Modified Jennite when sheared along the ba-Plane | 79 |

List of Tables

| | |
|---|----|
| Table 1 Unhydrated Cement Constituent..... | 4 |
| Table 2 Hydrated Cement Constituent..... | 5 |
| Table 3 Cell Parameters of a Single Unit Cell Jennite..... | 31 |
| Table 4 Traditional and Modified Jennite Structures (% Weight)..... | 34 |
| Table 5 Shear Modulus, Strength and Maximum Shear Deformation of cb-plane | 60 |
| Table 6 Predicted Shear Modulus (GPa) all planes | 68 |
| Table 7 Ultimate Shear Stress (GPa) all planes | 69 |

Abstract

Material properties and performance are governed by material molecular chemistry structures and molecular level interactions. Methods to understand relationships between the material properties and performance and their correlation to the molecular level chemistry and morphology, and thus find ways of manipulating and adjusting matters at the atomistic level in order to improve material performance are required. A computational material modeling methodology is investigated and demonstrated for a key cement hydrated component material chemistry structure of Calcium-Silicate-Hydrate (C-S-H) Jennite in this work.

The effect of material ion exchanges on the mechanical stiffness properties and shear deformation behavior of hydrated cement material chemistry structure of Calcium Silicate Hydrate (C-S-H) Jennite was studied. Calcium ions were replaced with Magnesium ions in Jennite structure of the C-S-H gel. Different level of substitution of the ions was used. The traditional Jennite structure was obtained from the American Mineralogist Crystal Structure Database and super cells of the structures were created using a Molecular Dynamics Analyzer and Visualizer Material Studio. Molecular dynamics parameters used in the modeling analysis were determined by carrying out initial dynamic studies. 64 unit cell of C-S-H Jennite was used in material modeling analysis studies based on convergence results obtained from the elastic modulus and total energies. NVT forcite dynamics using COMPASS force field based on 200 ps dynamics time was used to determine mechanical modulus of the traditional C-S-H gel and the Magnesium ion modified structures. NVT Discover dynamics and COMPASS forcefield was used in the material modeling studies to investigate the influence of ionic exchange on the shear deformation of the associated material chemistry structures. A prior established quasi-static deformation method to emulate shear deformation of C-S-H material chemistry structure that is

based on a triclinic crystal structure was used, by deforming the triclinic crystal structure at 0.2 degree per time step for 75 steps of deformation.

It was observed that there is a decrease in the total energies of the systems as the percentage of magnesium ion increases in the C-S-H Jennite molecular structure systems. Investigation of effect of ion exchange on the elastic modulus shows that the elastic stiffness modulus tends to decrease as the amount of Mg in the systems increases, using either compass or universal force field. On the other hand, shear moduli obtained after deforming the structures computed from the stress-strain curve obtained from material modeling increases as the amount of Mg increases in the system. The present investigations also showed that ultimate shear stress obtained from predicted shear stress – strain also increases with amount of Mg in the chemistry structure. Present study clearly demonstrates that computational material modeling following molecular dynamics analysis methodology is an effective way to predict and understand the effective material chemistry, and additive changes on the stiffness and deformation characteristics in cementitious materials and extendable to others.

CHAPTER 1

Introduction

Research has suggested that at least 20% of all product innovation is based on the introduction of new and innovative materials. It has also been established that material properties and performance is governed by molecular structures and molecular level interactions [1]. Hence it behooves engineers and scientists to find ways of understanding the relationships between the material properties and performance that are influenced by molecular level chemistry and morphology, and thus find innovative ways of manipulating and adjusting matters at the atomistic/molecular level in order to improve material performances. For example, cementitious materials that are the binders for mortar and concrete have material, geometrical features ranging from material chemistry/molecular/nano, micro, meso, and macro scales. Features and changes at the material chemistry/nanoscale level influence the hydration process, formed micro scale morphology, associated properties and behavior at engineering length scales. In order to engineer the material, it is required to develop a thorough understanding of the material chemistry and processes that define the material structure, this is particularly important for complex material systems such as cement. A brief background discussion of the material chemistry of cement and its multi-scale features is presented next.

1.1 Cement: Evolution of Material Chemistry

Because of its chemical durability, remarkable mechanical properties and high versatility, cement has remained the most widely utilized material in the world [2]. The starting material of cement is the clinker phase which is the unhydrated cement. The unhydrated cement phase is comprised of tri-calcium silicate (alite), di-calcium silicate (belite), tri-calcium aluminate, tetra-calcium aluminoferrite, and additional trace compounds [3]. *Table 1* below shows the various

cement clinker constituents and their corresponding mass percentages in a typical Portland cement clinker.

Table 1

Unhydrated Cement Constituent

| Cement Clinker | Chemical Formula | Oxide Formula | Shorthand Notation | Mass % |
|---------------------------------------|--|---|-----------------------|-----------|
| Tri-Calcium Silicate (alite) | Ca_3SiO_5 | $(\text{CaO})_3\text{SiO}_2$ | C_3S | 50-70 |
| Di-Calcium Silicate (belite) | Ca_2SiO_4 | $(\text{CaO})_2\text{SiO}_2$ | C_2S | 10-30 |
| Tri-Calcium Aluminate | $\text{Ca}_3\text{Al}_2\text{O}_5$ | $(\text{CaO})_3\text{Al}_2\text{O}_3$ | C_3A | 3-13 |
| Tetra-Calcium Aluminoferrite | $\text{Ca}_4\text{Al}_2\text{Fe}_2\text{O}_{10}$ | $(\text{CaO})_4.\text{Al}_2\text{O}_3\text{Fe}_2\text{O}_3$ | C_4AF | 5-15 |
| Calcium Sulfate Dehydrate (Gypsum) | $\text{CaSO}_4.2\text{H}_2\text{O}$ | $(\text{CaO})(\text{SO}_3)(\text{H}_2\text{O})_2$ | C-S-H_2 | 3-7 |

Source: ref [3].

Cement paste is made by combining dry Portland cement and water. The process of making cement paste is referred to as hydration, during which, there is loss of workability, solidification and hardening. The hydration of the different clinker phases results in different hydration product phases, which makes up the cement paste. The hydrated cement phases include; calcium silicate hydrate (C-S-H), calcium aluminum hydrate (C-A-H) and calcium hydroxide (C-H) [3, 4], see *Table 2* for the common components of hydrated cement paste.

Table 2

Hydrated Cement Constituent

| Name or Mineral Phase | Chemical Formula | Cement Chemical Notation (CCN) |
|------------------------------|---|--------------------------------|
| Calcium Silicate Hydrate | $2(\text{CaO}).\text{SiO}_2.0.9-1.25(\text{H}_2\text{O})$ and/or $\text{CaO}.\text{SiO}_2.1.1(\text{H}_2\text{O})$ and/or $0.8-1.25(\text{CaO}).\text{SiO}_2.1.0-2.5(\text{H}_2\text{O})$ | C-S-H |
| Calcium Hydroxide | $\text{Ca}(\text{OH})_2$ OR CaOH_2O | CH |
| Calcium Aluminium Hydrate | More complex than C-S-H | C-A-H |
| Aluminate Ferrite Trisulfate | $\text{C}_3\text{AS}_3\text{H}_{30-32}$ | Aft |
| Aluminate Ferrite | $\text{C}_2\text{ASH}_{12}$ | AFm |
| Hydrogarnet | $3\text{CaO}.\text{Al}_2\text{O}_3.6(\text{H}_2\text{O})$ | C_3AH_6 |

The C-S-H phase which constitutes a significant percentage of the hydrated cement paste is of interest because it is primarily responsible for the strength and load bearing attributes of cement [3, 5]. However, because of its complex material chemistry [6], C-S-H molecular structural representation is still inconclusive, and hence has been described by different molecular model crystal structures [7]. Some of these molecular structures are discussed in chapter 3.

The interest and motivation of the present work is to understand the effect of material ion exchange and material chemistry level changes on mechanical stiffness properties and shear deformation behavior obtained through computational material chemistry level modeling of hydrated cement constituent C-S-H Jennite.

1.2 Cement: Multi-Scale Nature

A phase in continuum micromechanics, is a material domain that can be identified at a given length scale with homogenous deformation state and constant material properties.

Continuum micromechanics have made it possible to represent heterogeneous regions with homogeneous phases, with equivalent mechanical properties [8]. Individual homogenous phases at microscopic state have, on-average, a constant strain state; and classical homogenization techniques helps to predict the overall behavior of heterogeneous materials from that of their constituents [9]; hence the possibility of homogenizing the lower scale into higher scale and delivering specific scale phase properties, volume fraction and specific morphologies [3].

Cement paste exhibit multi-scale features; it has a complex nature with random microstructure at different length scales and the concept of the continuum micromechanics have been used in cement structure studies [8-10]. Several application properties, have utilized the continuum micromechanics length scale framework; including heterogeneous thermoelasticity, rate-independent elastoplasticity, nonlinear elasticity, viscoplasticity, viscoelastic coupling and rate-dependent effects [4], these are primarily at the microstructure level. However, in cement paste, four levels of scales have been identified [8] i.e. molecular /nano-scale level determined by the material chemistry features, micro-scale with microstructural morphology features, meso-scale and macro-scale. Distinct length scales and features are based on the requirement that each scale should be separated from the next scale by at least one order of length magnitude, which is also stated in the literature as a prerequisite for the application of continuum micromechanics [3, 4]. As a result of the multi-scale nature of cement paste, the properties and material composition of the macro and engineering scale cement can be controlled or affected by the molecular level. A

potential ability to alter and manipulate the chemistry level structure of hydrated component of traditional C-S-H, a structure predominantly influenced by calcium - a major constituent of the cement paste at the fundamental material chemistry level - will imply that the elastic and shear deformation properties of the paste would be impacted. *Figures 1 and 2* shows the different levels of scale associated with cementitious materials. *Figure 1* shows a schematic of the multi-scale material structure while *Figure 2* shows the associated forms of cement in engineering applications.

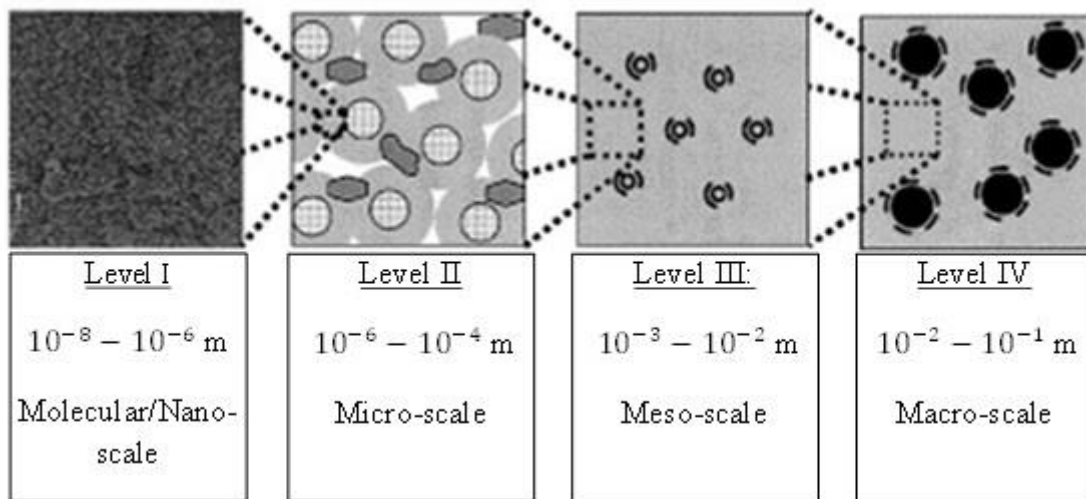


Figure 1. Schematics of multi-scale material structure of cement-based materials.

source ref [8].



Figure 2. Multiscale nature of cement-based materials.

1.3 Objectives

Traditional cement paste is primarily calcium-based, but engineering community, the cement-producing industry, and government establishments such as the U.S. Department of Defense are looking for alternate formulations of cement; which may provide tailored properties for specific applications, could utilize local, and cheaper materials. Another factor influencing the alternate forms cement cited in the literature is the need to reduce the energy required to produce the clinker phase, and the carbon foot print of the cement industry [2]. Hence there have been efforts to look for alternate cement formulations that are not calcium-based, might be cheaper, and have the potential for reducing carbon footprint in the manufacturing stage of calcium based cement. Several forms of cement formulations has been sought, for instance, other forms of belitic cements are sought by trial and error to improve the reactivity of the clinker phase. Some additional approaches that have been used trying to improve the properties of cement-based materials include thermal processing [11, 12] and addition of new chemical compounds and ions [2, 11, 12]. Most common types of ionic substitution which has been used in cement phases include; Mg^{2+} for Ca^{2+} , 2Al^{3+} and 2Fe^{3+} for 3Ca^{2+} , and 2Ca^{2+} for Si^{4+} [2, 13]. The present work investigates the influence of replacement of calcium ion with magnesium ion in the material chemistry level of C-S-H with a focus on mechanical stiffness and shear deformation characteristics via computational material modeling.

Several studies have focused on different aspects of cement material improvement. Hegoi and co-workers [2] studied the effects of the presence of chemical substitution on the physicochemical properties of cement clinker phases - alite and belite. They incorporated Mg^{2+} , Al^{3+} and Fe^{3+} into the structure using classical forcefield methods and reported that the crystallographic site within the unit cell is equally probable for Mg, Al and Fe substitution. It has

also been reported that Mg incorporation does not change the electronic structure appreciably compared to Al and Fe incorporation [2], and that there are no preferential substitution for any calcium sites, when Mg^{2+} , Al^{3+} and Fe^{3+} were incorporated. The main focus of their research was on the reactivity of the clinker phase for reduced energy production. Research efforts to study the effect of Mg ion exchange on the mechanical stiffness and deformation have not been reported.

As discussed in the literature, Mg provides a feasible incorporation option in cement paste. In their study of the hydration process of cement, Stephan and co-workers [13], provided analytical evidences that in low concentrations, Mg^{2+} does not change the hydration process of C_3S – a component of cement (*Table 1*), although the reactivity may increase with weight percent and with cement age. Also, because of the relative availability and the ionic similarities to Calcium, Mg can be considered as a potential candidate for ionic replacement. Additionally, with the replacement of Ca by Mg a lower temperature for processing the clinker phase can be achieved.

The objective of this work is to understand the influence of the effects of the exchange of Calcium ion with Magnesium ions in hydrated cement material chemistry structure based on the shear deformation behavior and mechanical stiffness properties of the modified material using computational material modeling and simulations. Different computational simulation methods have been employed in the past to study heterogeneous materials. Hegoi et al [2] used a combination of forcefield and DFT atomistic simulation in their mentioned prior mentioned study, others have used ab initio methods to study the structure of C-S-H [14, 15]. There are also studies of the mechanical behavior of heterogeneous materials using multi-scale modeling, and studies to understand cement hydration with finite element modeling as well as temperature dependency of the microstructure of cement hydrates [8, 16-18] reported in the literature. To the

best knowledge of the author, no other studies have been focused on the effects of chemistry level ion exchange on the mechanical stiffness and deformation behavior of cement hydrates. The present study focuses on the effect of Calcium ion substitution with Magnesium on chemistry level structure of C-S-H and to understand the variations on the predicted mechanical stiffness and shear deformation.

1.4 Computational Modeling

In order to move nanotechnology research from the nascent exploratory research which was initiated mostly to understand underlining principles to designing new materials that will meet existing and new needs, and thus become commercially viable; a rational nanomaterial design and rigorous engineering design would be required. The knowledge and understanding of the properties based on atoms and molecules that form the material chemistry structure at a nano-scale is very critical to achieving this rational design. At the bottom line of this understanding is the use of computational algorithms and relevant analysis code developments that would help in predicting the behavior of new material performances even before they are formed and subjected to any laboratory efforts. Material chemistry level modeling following the principles and techniques commonly grouped under Computational Material Science is one of the key facilitator of material science that is experiencing fast growth pace and forms the basis of the present work [19].

The background of computational modeling methods and framework followed in the present research is presented and discussed in Chapter 2.

CHAPTER 2

Computational Modeling Methods – Background

This chapter presents the background details of the computational modeling methods employed in the present work. In particular, material chemistry level modeling is based on molecular configurations formed with atoms and bonds and their interactions. A brief discussion of the background of Molecular Dynamics (MD) modeling techniques is presented next.

2.1 Molecular Dynamics Techniques

Quantum mechanics offers an accurate solution to the position-space wave function of electron level systems. However, it is computationally complex and difficult to solve the wave function for larger systems [20]. Hence, Molecular Dynamics (MD) methods has been developed and used to solve atomic/ molecular level systems. Unlike quantum mechanics, molecular dynamics can be applied to larger and complex systems; it is also computationally less expensive and faster. Molecular Dynamics helps to fill the gap created when statistical mechanics –which uses partition function of systems in equilibrium, meets a roadblock due to essentially lack of system equilibrium. This is because, once out of equilibrium, theory cannot provide quantitative solutions unless several approximations are applied; hence simulations like Molecular Dynamics are employed to solve this equilibrium challenges [21]. A particular subset of Molecular dynamics modeling techniques is the one denoted as Classical Molecular Dynamics, which is a numerical technique that uses classical mechanics to model atomic scale systems. In it, the position and velocities of atoms forming a molecular system are estimated based on the solution of the classical equations of motion, Newton's laws of motion. This technique cannot be used to study the chemical reactions or predict chemical reactivity of molecules.

Unlike lattice-based simulation methods like cellular automata, MD simulations operates in continuum and are not spatially discrete [22], hence problems like unfavorable effects due to lattice symmetry and lack of range of particle velocities are not encountered in MD, although it is computationally more demanding [21]. Other simulations techniques, like Monte-Carlo simulations, eliminate the momentum part of the phase space and considers only configuration space, hence, can only be used to study systems in equilibrium and process consequences. However, MD enables a detailed study of the dynamics (path and consequences) of a molecular system [23]. In Classical MD, atoms are viewed as mass points, and are described by mass (m), charge (q), position (x, y, z) and velocities (V_x, V_y, V_z) – this has been described by the particle model with the particles carrying the properties of physical objects [20]. By virtue of their existence and vicinity, these particles/atoms interact with one another (bonds can be viewed as springs and the bond strength are related to the spring constant), and these interactions are referred to as interatomic potential. *Figure 3* shows a 3-atom system with their various interactions. In molecular dynamics, the interatomic potentials are evaluated via force-field calculations [21, 24].

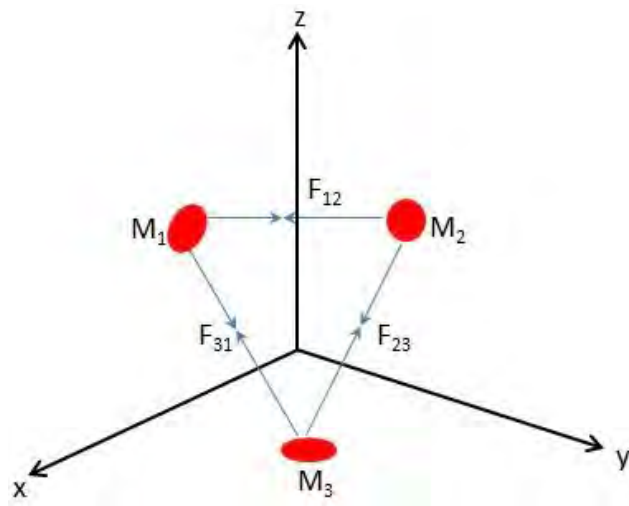


Figure 3. Atomic positions and interaction forces on a 3-atom system.

2.2 Force Field/Interatomic Potential

In Classical MD, the energy associated with molecular systems is based upon energy associated with the atomic level interactions of different atoms in a molecular system. The potential energy of atomic system is expressed as the sum of various interactions that exist in a given molecular [25] system as;

$$E_{Total} = E_{Bonded} + E_{Non-bonded} + E_{Cross\ terms} \quad \text{Equation 1}$$

$$E_{Bonded} = E_{Stretch} + E_{Angle} + E_{Torsion} + E_{Out-of-plane} \quad \text{Equation 2}$$

$$E_{Non-bonded} = E_{VDW} + E_{Electrostatic} \quad \text{Equation 3}$$

where E_{Total} is the total energy of an atomic system accounted for by a combination of both bonded and non-bonded components of the interactions of the atoms. The bonded component of the interaction potential comprise of; the bond stretching component ($E_{stretch}$), which views the bonds as springs under harmonic oscillation and thus the relation in *figure 4* below. The bond angle bending, and dihedral angle torsion components of the angular distortion (E_{Angle} and $E_{Torsion}$) [25], relate the interactions between three and four atoms, with respect to the angles between three atoms and the angles between different planes of four atoms, and the inversion term ($E_{Out-of-plane}$). The non-bonded component is comprised of Vander Waals interactions (E_{VDW}) which relates the long range attractive and short range repulsive effects on neutral atoms using the Lennard-Jones potential [21, 25], *figure 4*, and electrostatic interactions ($E_{Electrostatic}$) [26].

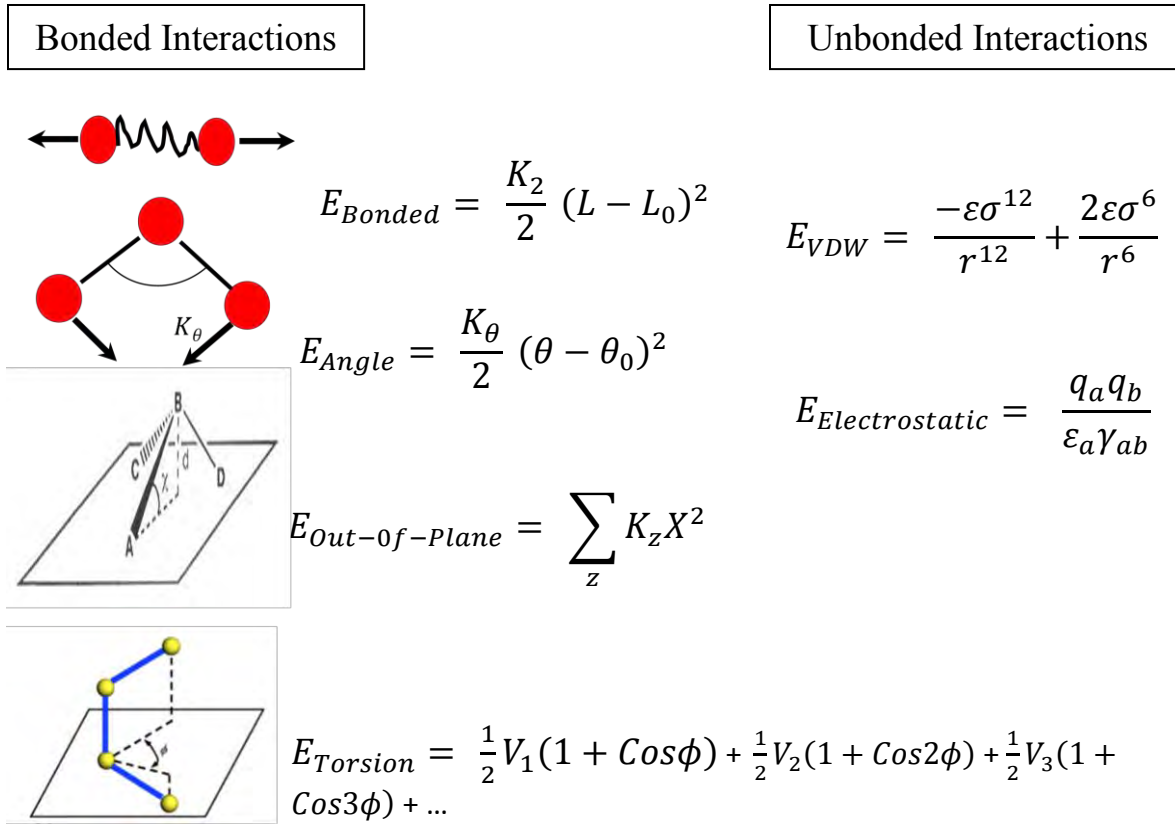


Figure 4. Bonded and unbonded interactions.

The interatomic force can then be obtained as the spatial gradient of the total potential energy of the system [20, 21, 27].

$$F_i = - \frac{dU}{dr_i} \quad \text{Equation 4}$$

The trajectories of individual particles, $r_i(t)$ of the system can be estimated solving the Newton's equation of motion [20, 21, 27].

$$F_i = m_i a_i = m_i \frac{dv_i}{dt} = m_i \frac{d^2 r_i}{dt^2} \quad \text{Equation 5}$$

During the time-evolution of the dynamics of a molecular system the positions and velocities are updated after each time step. Since all the thermodynamic properties of the molecular system can be estimated based on the set of positions and velocities, a time-profile of

them can be created during the time-evolution of the molecular system. The physical properties under thermodynamic conditions employed in the simulations can, therefore, be average of large enough periods of time as to satisfy the conditions required by the Ergodic hypothesis. *Figure 5* shows a typical molecular dynamic process step.

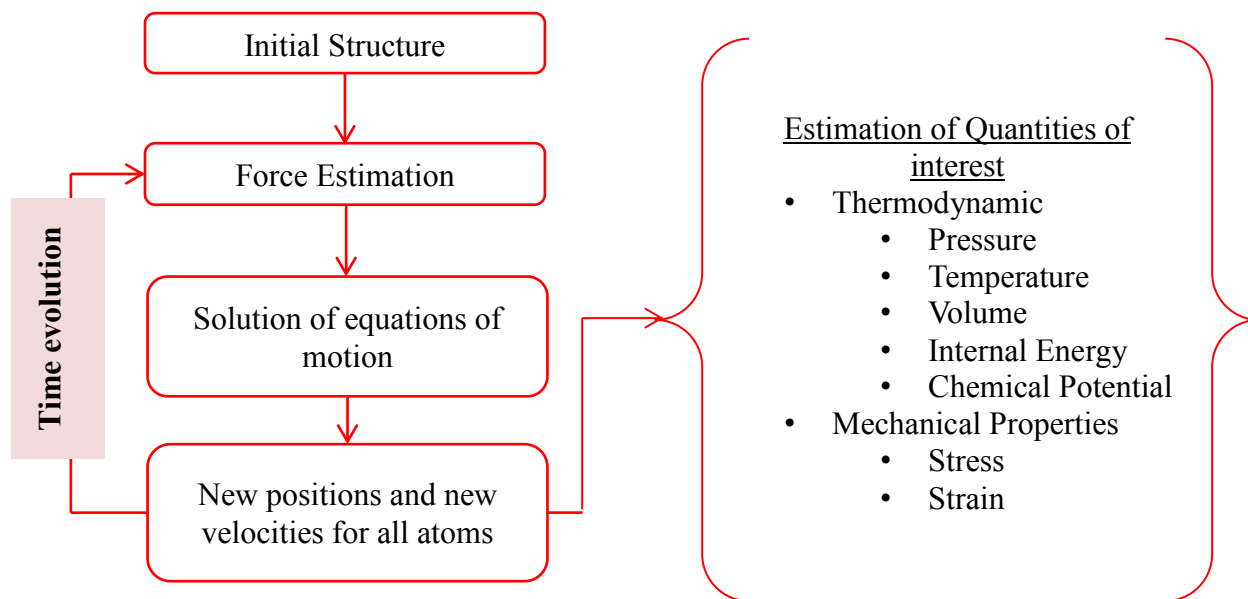


Figure 5. Molecular dynamics process.

Figure 6 shows a time average line for a thermodynamic or physical quantity. Section 2.5 discusses the approaches used in executing this transient dynamic process.

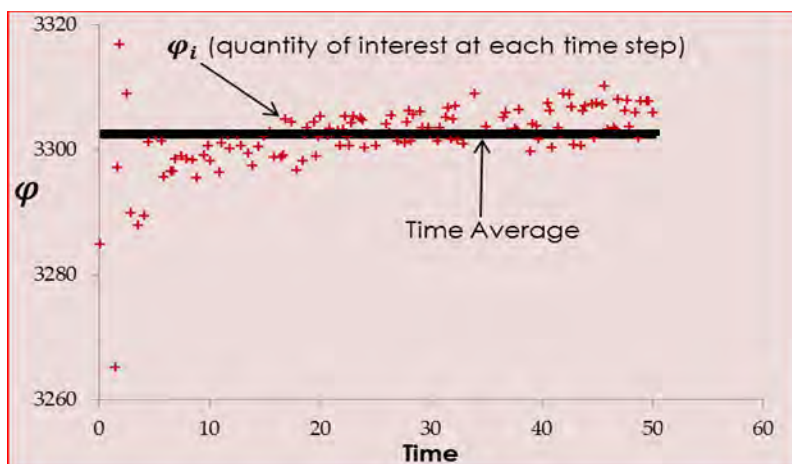


Figure 6. Time average. Quantities of interest are obtained as average over a dynamic time.

The solutions to the equations of motion are based on constraints such that certain thermodynamic properties are controlled. Hence, the system under investigation can be subjected to constraints such as constant temperature, pressure and volume. The combination of these thermodynamic constraints is called ensembles which are discussed later. In Molecular dynamics, the potential energy for bonded and non-bonded interactions of different material atoms has been defined by different forcefields that have been developed and applicable to material atoms involved in the molecular system. The predicted properties of a molecular dynamics analysis for material modeling are influenced by the underlying forcefields used in analysis. Two such force fields have been employed in the present study on material modeling based on material chemistry structure of hydrated C-S-H Jennite.

2.2.1 Universal force field (UFF). Universal Force Field (UFF) provides the possibility of constructing and defining most structural features across the elements in the periodic table. The limitation of prior existing forcefield applications to proteins, nucleic acids and organic molecules deepened the efforts resulting in the development of the Universal force field which could be applied to the entire periodic table. It is generated using parameters which include hybridization dependent atomic radii, Van der Waals parameters, hybridization angles, effective nuclear charges, as well as inversion and torsional barriers. UFF has 126 atom types, which are described by a five character mnemonics. The force field assigns potential energy related to the geometry of the molecules as a superposition of various two, three or four body interactions. For atoms that are bonded to each other in a 1, 2 interaction or those bonded to a common atom in a 1, 3 interactions, UFF follows the convention of excluding Van der Waals and electrostatic interaction [28].

2.2.2 COMPASS force field (COMPASS). Condensed-phase optimized molecular potentials for atomistic simulation studies or COMPASS force field was developed as a general all-atom forcefield for atomistic simulations of common organic, small inorganic molecules and polymers. This is a proprietary forcefield within the MD analysis and visualizer code Materials Studio. Ab-initio and empirical parameterization techniques were used [29], and validated using condensed-phase properties for molecules in isolation. This force field can be used for a broad range of molecules in isolation and in condensed phases. It is capable of predicting numerous solid state properties, unit cell structures, lattice energies, elastic constants and vibrational frequencies [30] and under a wide range of conditions of temperature and pressure.

2.3 Ensembles and Controls

Molecular dynamics is based on the integration of classical equations of motion on molecular systems to simulate their kinetic and thermodynamic properties. It samples micro-canonical ensembles (NVE) [31], since a system is usually characterized by a time-independent, translationally and rotationally invariant Hamiltonian. The integration of the classical equations of motion leads to a trajectory that maps several dynamic micro-canonical ensembles (NVE), where all the forces which appear in the Newton's equations of motion, are related to the potential energy of the system, and the total energy of the system ($E_{Total} = E_{Kinetic} + E_{Potential}$) is conserved (NVE – fixed number of particles, volume and energy). But there are cases when it is desirable to make a system comparable with experiments. For instance when average temperature must be at desirable values, this leads to a canonical sample configuration with fixed number of particles and volume and with the temperature having a specified macroscopic average but with fluctuating instantaneous total energy or Hamiltonian (NVT ensembles). Other possibilities include, grand canonical ensembles (μVT) where there is a

constant volume and temperature as in canonical ensembles but it is however open to particle exchange with the surrounding bath. In grand canonical ensembles, the chemical potential of different species have a specified average [31]. In isothermal-isobaric (Gibbs) ensembles (NPT), the pressure has a specified average and the instantaneous volume of the system can fluctuate [31]. Thermostats algorithms are the various computational based methods in molecular dynamics which are introduced to modify the time dependent changes in atom positions and velocities to achieve this temperature controls [31, 32]. The purpose of these thermostat controls is to ensure the average temperature of a molecular system is maintained at and close to a desired temperature [32]. A brief background of the different thermostats employed in molecular dynamics analysis and studied in the present work is presented next.

2.3.1 Andersen thermostat. It works by coupling the molecular system to a heat bath, by an occasional stochastic collision that acts randomly on selected particles, imposing a desired temperature on the system [32]. The instantaneous stochastic collision affects the momentum (velocity) of one particle and other particles are unaffected by the collision [32, 33]. The Hamiltonian equations for all the particles are integrated until the time for next instantaneous collision [32-34]. Andersen thermostat can be used for non-equilibrium processes where large amount of heat is liberated for systems with low heat capacity, and for processes such as nucleation and phase separations which require large energy and density fluctuations [34].

2.3.2 Velocity scaling. It is probably the most straight forward temperature control method. Maxwell-Boltzmann distribution is used to draw the distribution of velocities of material components. The average kinetic energy of each component per degree of freedom can be obtained and related to the temperature using equipartition theorem, and this is averaged over all the particles to obtain the instantaneous temperature of the finite sized material system. If the

temperature used to generate the velocity distribution does not coincide with the instantaneous temperature, then the velocity is rescaled until the temperature coincides [35]. Velocity scaling does not reproduce the canonical ensembles [35, 36], and it is not deterministic or time reversible and does not remove localized and unwanted correlation motions [36].

2.3.3 Nosé thermostat. Instead of using stochastic collision to introduce energy fluctuations into the simulation system, a Lagrangian with artificial coordinates and velocities also referred to as extended Lagrangian method are used in Nosé thermostat. A Nosé thermostat controlled system has more independent variables than equivalent statistical mechanics approach giving more accurate results for static quantities [32, 37, 38]. It has also been shown that the simulations of extended systems (which includes a real micro-canonical system and a heat bath) produces a canonical ensemble in the real systems due to heat exchange between fictitious degree of freedom and real systems, with coupling between the two controlled by a fictitious mass [35]. The method offers a stable and efficient approach to molecular dynamics analysis simulations. However, its more expensive to carry out each optimization steps [32], and it is not Ergodic (i.e. the system does not have has a finite chance to go everywhere in phase-space in a finite time) in some difficult cases such as in harmonic systems [33].

2.3.4 Berendsen thermostat. Berendsen et al [39] introduced weak coupling of system to heat bath thereby limiting the temperature fluctuations in canonical ensembles found in velocity scaling. In this temperature control method, the coupling adds or removes energy form the system to maintain the temperature and the velocities are scaled at each step such that the rate of temperature change is proportional to the difference between the target and instantaneous temperature given by;

$$\frac{dT}{dt} = \frac{1}{\tau} (T_0 - T)$$

Equation 6

When the target temperature T_0 is less than desired system temperature T , the temperature will increase and if $T > T_0$, heat will be removed from the system. A generally employed value for τ is 0.4ps, which result in modest temperature fluctuations in most MD analysis simulations [35, 39]. Berendsen thermostat leads to exponential relaxation of the temperature to a target one, it does not strictly fix the temperature [35]. Also when the coupling is weak ($\tau = 0.01ps$) there may be perturbation of the various quantities that will not lead to correct canonical averages [35].

2.3.5 Andersen barostat. The methods in MD by which the time dependent changes in atomic configurations can be modified as a function of pressure are called the barostat. Andersen barostat mimics the action of a piston by coupling the system to external variable [27], by addition of an extra degree of freedom to the volume of the simulation box as well as associated potential and kinetic energy terms. It allows for volume change within the simulation with average volume determined by a balance between the internal pressure of the system and the desired external pressure of the system.

2.3.6 Parinelo barostat. Parinelo barostat controls the pressure by the introduction of additional degrees of freedom to the whole system of atoms in time and space, via the transformation of the spatial coordinates x_i into scaled positional coordinates, $\dot{x}_i \in [0,1)^3$. This is possible by transforming the Lagrangian describing the system into the corresponding Hamiltonian [20].

2.3.7 Berendsen barostat. Similar to the Berendsen thermostat, the barostat is coupled with a pressure bath by a weak coupling with coupling constant τ_p and the volume of the system is scaled by a scaling factor λ . The rate of change of pressure is given by *Equation 7* and scaling factor is defined by *Equation 8*.

$$\frac{dP(t)}{dt} = \frac{1}{\tau_p} (P_{bath} - P(t)) \quad \text{Equation 7}$$

$$\lambda = 1 - k \frac{\delta t}{\tau_p} = \frac{1}{\tau_p} (P - P_{bath}) \quad \text{Equation 8}$$

where; P_{bath} is the pressure of bath, $P(t)$ is the actual pressure at time t and atomic coordinates are scaled by a factor of $\lambda^{1/3}$, new atom position is defined as;

$$r_{iscale} = \lambda^{1/3} r_i \quad \text{Equation 9}$$

2.4 Energy Minimization

Consider a simulation box with the atoms of the molecular structure located on certain defined locations in the x,y,z space. The structures that define the molecular material model configuration are assigned specific locations for each of their atoms which may not necessarily be the equilibrium positions with a minimal energy. In order to evaluate the energy of the system, we need a force-field or interaction potential which is nothing but a mathematical expression of the relationships that are dependent upon the atom type, locations of each atoms and the resulting energy based on bonded and non-bonded interactions. Hence, the potential energy is $E = E(x_i)$ in general. In the present work, we use the UNIVERSAL and COMPASS force fields to relate the above interactions. Before any dynamics run in a molecular dynamics analysis, energy minimization is employed to get a low energy stable configuration of the material system. There are numerous mathematical algorithms that can be employed for energy minimization of the multi-dimensional energy function: conjugated gradient, Newton-Rapson iteration etc. The numerical integration method used for solving the classical equation of motion is presented next.

2.5 Time Integration Method

The integration of the equations of motion is done numerically and there are different methods of doing this in principle [21, 40]. However, there are selection criteria which include limited calculation of the force component, a corresponding increase in time step if force

components are calculated but without crossing the upper bound limit constraints placed by Lennard-Jones repulsive force at short distances [21]. Hence Runge-Kutta and adaptive methods of time integration which could not increase their time steps beyond the Lennard-Jones limits are quickly discarded in most MD analysis. Of common use are the leap frog methods, Verlet methods and the predictor corrector methods.

Leap frog and Verlet method are algebraically equivalent [21] and are perhaps the most widely used time integration methods in molecular dynamics, easy to implement, stable and time reversible. Verlet method is used in the MD simulations performed in this study. It is a direct solution to the second order equation 5 [21, 27]. It follows from the Taylor's series expansion of coordinates and based on the previous particle position $r(t - \delta t)$, present position $r(t)$ and acceleration $a(t)$. The next position can be written without necessarily evaluating velocity the term as:

$$r(t + \delta t) = 2r(t) - r(t - \delta t) + \delta t^2 a(t) \quad \text{Equation 10}$$

The velocity term which is not needed for trajectory calculations have been eliminated by Taylor series expansion about $r(t)$. It can however be computed when needed for kinetic energy calculations as [21, 27].

$$V(t) = \frac{r(t+\delta t) - r(t-\delta t)}{2\delta t} \quad \text{Equation 11}$$

2.6 Periodic Boundary Condition

Finite and infinite systems behave in different manner [21]. The aim of Periodic Boundary conditions (PBC) in the molecular dynamics analysis is to ensure that the molecular system does not have an abrupt boundary with a vacuum, to remove any significant peripheral surface effects [30]. In order to capture the typical state of interior atoms, wall/boundary effects are eliminated [21] using PBC. Periodic boundary can be viewed as an array of infinite identical

copies of a simulation region implemented in order to reduce the fraction of atoms near the walls/boundary [27, 41]. Particles that leave a simulation boundary reenters through the opposite face, hence the boundary of the central cell are not rigid and there are no particle reflection in the central cell [20], but the periodic images of the central cell behaves in the same way. It is important to know if the properties of both macroscopic and small infinite periodic system are the same. The common practice in computational simulation is to ensure the choice of periodic size has little effect on the equilibrium thermodynamic properties of the structure, and depending on computational resources available, to increase the box size to maintain constant density. Cubic box is usually used in most periodic repetition [27].

2.7 Dynamic Simulations and Post-Analysis of Physical Quantities

The positions and velocities of molecular system, as a result of their molecular interactions, carry information that can be used to evaluate their instantaneous thermodynamic properties such as their temperature, pressure, kinetic energy and potential energy (*Equations 1-5 and figure 4*). From section 2.5 above, we saw that we can evaluate new positions of particles based on the numerical time integration methods. Hence, at each time steps the required thermodynamic properties can be computed and profiled.

The positions and velocities of the molecular system in their initial state are chosen such that no particles occupy exactly the same position [21, 27, 42]. Lattice locations are often used to place particles and velocity components are attributed to the particles [42] from Gaussian distribution (*Equation 13*), with magnitudes conforming to the required temperature of the system. This is then corrected such that overall momentum is zero [27].

$$P = \sum_{i=1}^N m_i V_i = 0 \quad \text{Equation 12}$$

$$\rho(v_{ix}) = \left(\frac{m_i}{2\pi K_B T} \right)^{\frac{1}{2}} \exp - \left(\frac{-m_i V_{ix}^2}{2K_B T} \right) \quad \text{Equation 13}$$

where $\rho(v_{ix})$ is the probability density function of the velocity component v_{ix} [27].

Most times the simulation is started from disordered configuration at different density and temperature. Equilibration is done to bring the molecular system to a new equilibrium state. This is done up to a satisfactory time where there is small oscillation of tracked properties such as potential energy about a steady mean value [27].

The interatomic potential is dependent on the positions and velocities of the atoms. As shown in the equations in *figure 4*.

Also, the kinetic energy of the molecular system can be derived from equation 14 [27];

$$K.E = \sum_i \frac{1}{2} m_i V_i^2 \quad \text{Equation 14}$$

Base on the velocities of the atoms, the molecular system temperature can be obtained from the average of a kinetic temperature function derived from Virial theorem and equipartition principle for N atoms with N_c internal molecular constraints as [27, 43];

$$T = \frac{2\mathcal{K}}{(3N-N_c)k_B} = \frac{1}{(3N-N_c)k_B} \sum_{i=1}^N |P_i|^2 / m_i \quad \text{Equation 15}$$

where; \mathcal{K} is the kinetic energy in phase function, k_B is the Boltzmann constant and P_i is the momentum of the particle. The pressure can also be obtained from the average of the pressure function [27, 43, 44].

$$p = \rho k_B T + \mathcal{W} / \mathcal{V} \quad \text{Equation 16}$$

where; \mathcal{W} is defined as the internal virial restricted for intermolecular interactions, and \mathcal{V} is the potential energy in phase function.

Virial expression can also be used to obtain the internal stress and strain tensors of molecular systems in atomistic simulations [30, 45], these are also based on the position and velocities of the atoms (*Equations 17, 18*).

$$\sigma = -\frac{1}{V_0} \left[\left(\sum_i^N m_i (\mathcal{V}_i \mathcal{V}_i^T) \right) + \left(\sum_{i<j} r_{i,j} f_{i,j}^T \right) \right] \quad \text{Equation 17}$$

where V_0 is the un-deformed system volume and f_i is the force acting on particle i . In order to obtain the stress tensor of the molecular structure in its static state, applied force stress term, $(\sum_{i<j} r_{i,j} f_{i,j}^T)$ in Equation 17 is omitted [30, 45]. The virial expression for the strain tensor is given by;

$$\varepsilon = \frac{1}{2} [(h_0^T)^{-1} (h^T h) h_0^{-1} - 1] \quad \text{Equation 18}$$

where h_0 , and h are the matrices formed by the column vectors defining the material system at a reference state and at corresponding new state. When Hooke's law is applied on the stress and strain tensors, elastic compliance and stiffness matrices can be obtained for the molecular material configuration [30].

$$C_{ijkl} = \frac{\partial \sigma_{ij}}{\partial \varepsilon_{kl}} \quad \text{Equation 19}$$

derivations of how the elastic constants of continuum particle can be obtained from the material strain tensor for either isothermal or adiabatic process can be obtained in dedicated textbooks [45]. The next section gives the summary of the elastic constraint matrix used for elastic stiffness property determinations.

2.8 Predictive Mechanical Properties

Computational simulation enables prediction of the mechanical stiffness properties of materials (bulk modulus, shear modulus and young's modulus) using their elastic constants which can be determined using [45, 46];

$$C_{ij} = \frac{1}{V} \frac{\partial^2 U}{\partial \varepsilon_i \partial \varepsilon_j} \quad \text{Equation 20}$$

Where: ε_i , ε_j are lattice strain components, U is potential energy, V is simulation cell volume.

The 6×6 elastic stiffness matrix, C can be obtained from the above relation.

$$C_{ij} = \begin{pmatrix} C_{11} & \cdots & C_{16} \\ \vdots & \ddots & \vdots \\ C_{61} & \cdots & C_{66} \end{pmatrix} \quad \text{Equation 21}$$

And elastic compliance matrix, $S = C^{-1}$ can also be obtained.

$$S_{ij} = \begin{pmatrix} S_{11} & \cdots & S_{16} \\ \vdots & \ddots & \vdots \\ S_{61} & \cdots & S_{66} \end{pmatrix} \quad \text{Equation 22}$$

Hence the mechanical stiffness properties for the homogeneous stiffness modulus can be predicted following Voight, Reuss or Hill elastic stiffness relations from the elastic and compliance matrix coefficients as [47]:

$$K_R = \frac{1}{(S_{11}+S_{22}+S_{33})+2(S_{12}+S_{23}+S_{31})} \quad \text{Equation 23}$$

$$K_v = \frac{(C_{11}+C_{22}+C_{33})+2(C_{12}+C_{23}+C_{31})}{9} \quad \text{Equation 24}$$

$$K_H = \frac{(K_v+K_R)}{2} \quad \text{Equation 25}$$

$$G_R = \frac{15}{4(S_{11}+S_{22}+S_{33})-4(S_{12}+S_{23}+S_{31})+3(S_{44}+S_{55}+S_{66})} \quad \text{Equation 26}$$

$$G_v = \frac{(C_{11}+C_{22}+C_{33})-(C_{12}+C_{23}+C_{31})+3(C_{44}+C_{55}+C_{66})}{15} \quad \text{Equation 27}$$

$$G_H = \frac{(G_v+G_R)}{2} \quad \text{Equation 28}$$

$$\nu = \frac{3K-2G}{6K+2G} \quad \text{Equation 29}$$

$$E = 2G(1 + \nu) \quad \text{Equation 30}$$

where; K_R = Reuss bulk modulus, K_v = Voight bulk modulus, K_H = Hill bulk modulus, G_R = Reuss shear modulus, G_v = Voight shear modulus, G_H = Hill shear modulus, E = Young's Modulus, ν = Poisson ratio [48] and C_{ij} and S_{ij} are the components of the stiffness and compliance matrix respectively [47, 49] .

2.9 Estimation of Material Property Based on Deformation and Stress-Strain Behavior

Most of the present work in molecular dynamics modeling of mechanical properties is determination of stiffness modulus as discussed earlier. Material characteristics are defined by their stress-strain behavior under deformation loading and the elastic properties of a material during deformation can be obtained from the stress-strain curve. Subjecting a material to shear, compressional or tensile force are ways of implementing such deformation. For material under a loading condition, an increase in the load results in an increase of the strain, first linearly following Hooke's law in the elastic deformation region, after which a slippage, non-linear, plastic deformation occurs [48] that causes response that is observed in a typical stress-strain curve, as shown in *figure 7*.

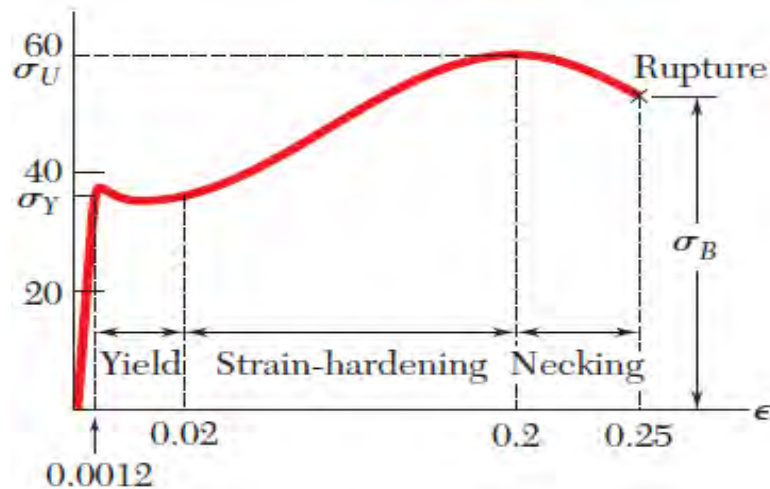


Figure 7. Typical stress-strain response

Source: Ref [48]

Computational material modeling of this stress-strain behavior based on material chemistry is still limited and has not been fully studied and understood. Recently, shear deformation versus strain behavior was recently investigated in our research group [50]. Other

recent literature had studied the unidirectional tensile, quasi-static shear deformation for nanoscale C-S-H Tobermorite. Molecular Dynamics modeling of the stress-strain behavior based on material chemistry molecular structures provides a fundamental methodology to understand the predicted behavior of a material solely based on its material chemistry, and provides an avenue to investigate the effect of the changes in the material chemistry on the mechanical behavior.

Following the molecular dynamics modeling methodology established in our research group, the effect of material chemistry of Magnesium-modified Jennite on shear deformation of nanoscale traditional Jennite is investigated in the present study. In the current work, shear deformation is implemented by deforming the molecular structure by increasing a particular angle of the crystalline structure while adjusting the length of the system to guarantee that the volume remain constant during the deformation process. *Figure 8* shows a triclinic structure under shear, along the cb -plane by a gradual change in the angle- α , thus subjecting the structure to deformation with resulting shear strain given by $\epsilon_{cb} = \delta\alpha_{cb}$. For every increment of the angle- α , the material experiences a shear strain , $\delta\alpha$ given by *Equation 31*.

$$\alpha_i = \alpha_{i-1} + \delta\alpha \quad \text{Equation 31}$$

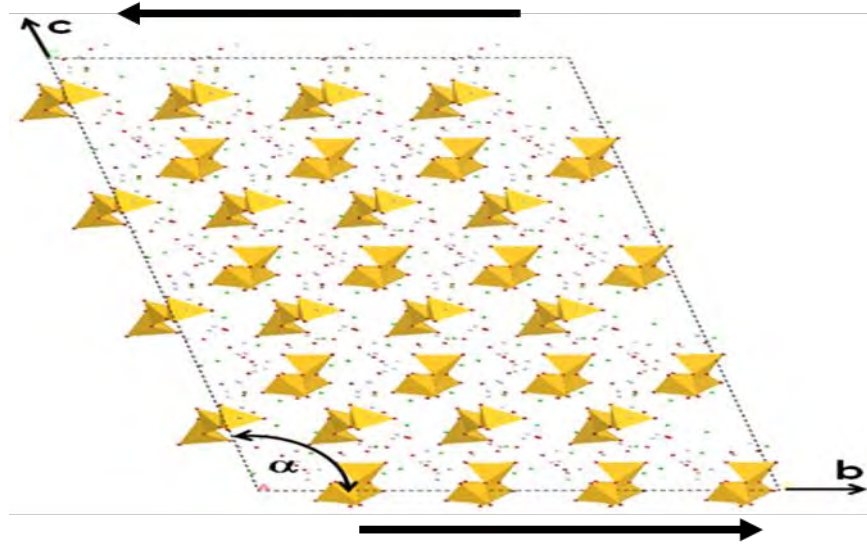


Figure 8. Shear deformation

The resulting stress strain curve from the computation model can then be used to estimate and predict the stress-strain behavior and elastic properties of the material under deformation loading for all the three crystallographic planes as discussed later in chapter 4.

CHAPTER 3

Computational Material Modeling Analysis of C-S-H Jennite

3.1 Software Analysis Codes for Molecular Dynamics Modeling

Different molecular dynamics modeling analysis codes have been developed and are available [21]. Some of which are open source codes or commercial codes. Large-scale Atomic/Molecular Massively Parallel Simulator (LAMMPS) and GRONingen Machine for Chemical Simulations (GROMACS) are examples of open source MD modeling analysis codes. Accelrys Material Studio is an example of commercial analysis code [21]. In the present work, MD modeling computational analysis was conducted using Materials Studio.

3.2 C-S-H Gel

As mentioned in chapter 1, C-S-H gel is a major component in the cement paste that is responsible for the load bearing attributes and strength of cement. C-S-H has a complex material chemistry [6]. The molecular structural representations of the C-S-H gel are still inconclusive, hence more than one structural representations are available [7]. Some of these molecular representations include:

- Wollastonite group which comprises of Foshagite ($\text{Ca}_4(\text{Si}_3\text{O}_9)(\text{OH})_2$) [51], Hillebrandite ($\text{Ca}_2(\text{SiO}_3)(\text{OH})_2$) [52], Xonotlite ($\text{Ca}_6\text{Si}_6\text{O}_{17}(\text{OH})_2$) [53], Okenite ($[\text{Ca}_8(\text{Si}_6\text{O}_{16})(\text{Si}_6\text{O}_{15})_2(\text{H}_2\text{O})_6]^{4-}[\text{Ca}_2(\text{H}_2\text{O})_9]3\text{H}_2\text{O}$) [54], and others that are compiled by Richardson [7]
- Tobermorite group which comprises of Clinotobermorite^c ($\text{Ca}_5\text{Si}_6\text{O}_{17} \cdot 5\text{H}_2\text{O}$), Clinotobermorite^d ($\text{Ca}_5\text{Si}_6\text{O}_{17} \cdot 5\text{H}_2\text{O}$), Clinotobermorite 9 A^{o,c} ($\text{Ca}_5\text{Si}_6\text{O}_{16}(\text{OH})_2$), Clinotobermorite 9 A^{o,d} ($\text{Ca}_5\text{Si}_6\text{O}_{16}(\text{OH})_2$) [55, 56], anomalous and normal

Tobermorite 11A° ($\text{Ca}_4\text{Si}_6\text{O}_{15}(\text{OH})_2 \cdot 5\text{H}_2\text{O}$ and $\text{Ca}_{4.5}\text{Si}_6\text{O}_{16}(\text{OH})_2 \cdot 5\text{H}_2\text{O}$ respectively) [57, 58] and Tobermorite 14A° [59]

- Jennite group comprising Jennite and Metajennite ($\text{Ca}_9\text{Si}_6\text{O}_{18}(\text{OH})_6 \cdot 8\text{H}_2\text{O}$). Most of the crystal structures are similar to one another than might seem apparent at first look, and a complete composition and crystal information for most of the C-S-H and other related phases has been tabulated by Richardson [7].

From the various molecular chemistry structural representations, Tobermorite 14A° and Jennite structures are the traditionally accepted, widely used and adapted molecular structural representation for most C-S-H cement paste studies [4, 6, 7, 60, 61]. For this study, Jennite structure of the material chemistry configuration of hydrated cement C-S-H was used.

3.2.1 Jennite. Jennite is a representative mineral form of calcium silicate hydrate (C-S-H). It has a chemical formula of $\text{Ca}_9\text{Si}_6\text{O}_{18}(\text{OH})_6 \cdot 8(\text{H}_2\text{O})$ [7, 60, 61]. It was named after Clarence Marvin Jenni (1896-1973) for its discovery [62]. Jennite is composed of single chains with repeating unit of three SiO_4 (Wollastonite-type dreier single chains), ribbons of edge sharing CaO_6 octahedral and additional CaO_6 octahedral on inversion centers [60, 62]. Jennite has a triclinic structure (*figure 9*) with dimensions of a single unit cell shown in *table 3* [60]. The MD modeling analysis employed in the present study is based on the material chemistry structure configuration of C-S-H Jennite.

Table 3

Cell Parameters of a Single Unit Cell Jennite

| a | b | c | α | β | γ |
|----------------------|---------------------|----------------------|-------------|------------|-------------|
| 10.576\AA^0 | 7.265\AA^0 | 10.931\AA^0 | 101.300^0 | 96.980^0 | 109.650^0 |

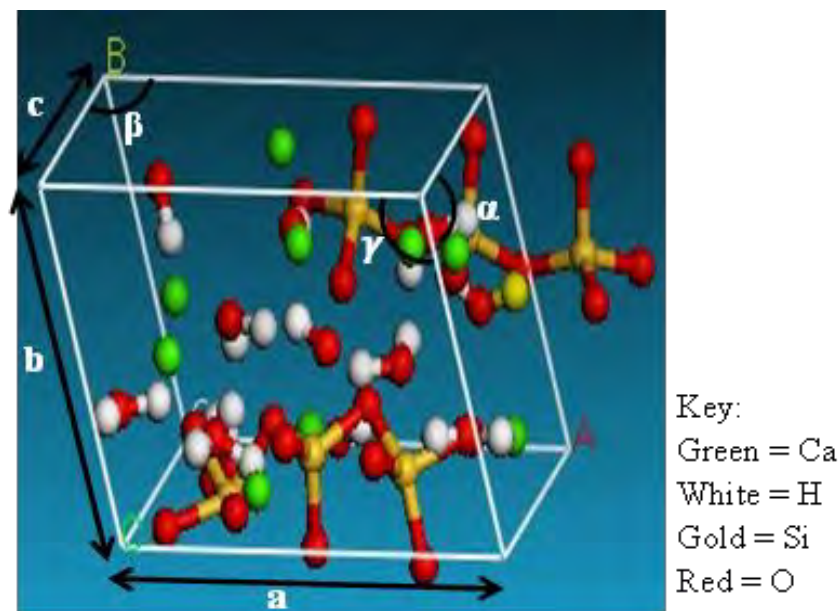


Figure 9. Jennite structure

The MD modeling analysis methodology employed in the present study with Accelrys Materials Studio is briefly presented next.

3.3 Molecular Dynamics Modeling Process

To initiate a MD simulation, the initial positions of the atoms forming the molecular structure is subjected to energy minimization and geometric optimization using Material Studio. The minimal energy configuration is then subjected to thermodynamic pressure and temperature constraints followed by a dynamic analysis (time evolution of the system). The flow diagram of the general MD simulation scheme is presented in *figure 10*.

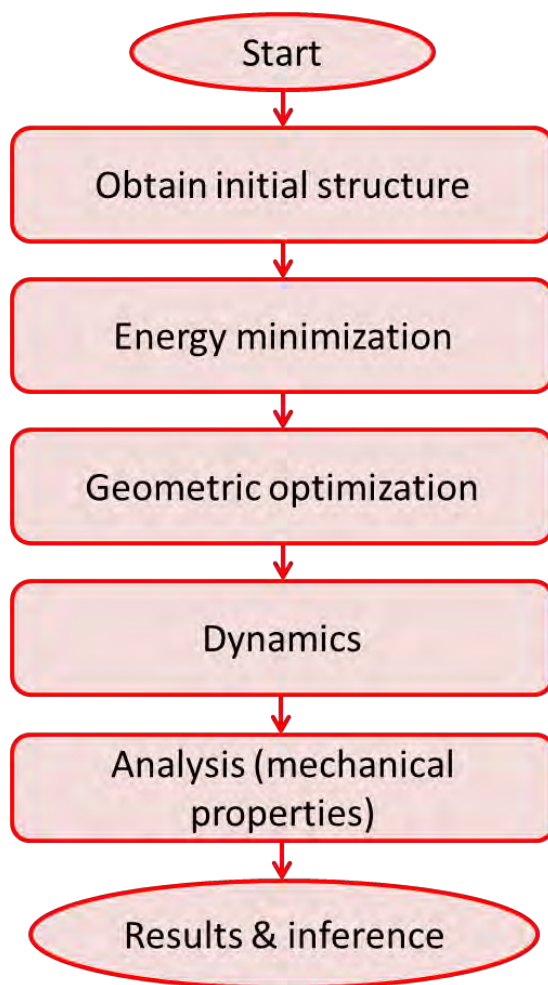


Figure 10. MD material modeling process

The present study focuses on the understanding the effect of material chemistry changes in C-S-H Jennite via MD analysis and development of relevant MD based material modeling methodology. The exchange of Calcium ions with Magnesium as discussed earlier was achieved in MD modeling with Accelrys Materials Studio as follows.

3.3.1 Molecular Structural Magnesium Exchange Approach. The traditional Jennite unit cell molecular structure was obtained from the American Mineralogist Crystal Structure Database [63]. This initial molecular structure configuration was loaded into Material Studio and was labeled as *J0*. For supercell structures to be made in Material Studio, a P1 space group must be used to impose the symmetry and was followed. The C-S-H Jennite unit cell structure

contains 9 calcium ions. The Magnesium-modified C-S-H Jennite molecular structure was obtained by successively replacing the calcium atoms by magnesium atoms. The Magnesium-modified molecular structures were then employed in the present work to understand the influence of the ion exchange.

A systematic study of replacing the different number of Magnesium ions in place of Calcium ions was conducted in the present work starting with the replacement of 2 Magnesium ions. Manzano et al, had established that there are no significant preferential tendencies about where the Ca ions are replaced by Mg ions, i.e. a random substitution pattern in the MD model accounts for the molecular structures expected in physical experimentation [2]. In the first modified C-S-H Jennite configuration with Magnesium atoms, two calcium ions were randomly replaced with magnesium ions, creating a modified Jennite structure, *J1*. The two Magnesium ions configuration resulted in a 14.8% Mg/(Mg+Ca) ratio. Additional Magnesium modified structures were created by the exchange of 4 – 9 calcium ions resulting in different magnesium concentrations by weight. The various Magnesium modified molecular structural configurations of C-S-H Jennite considered for the present study are shown in *table 4*.

Table 4

Traditional and Modified Jennite Structures (% Weight)

| Jennite | n-Ca | n-Mg | n-H | n-O | n-Si | Atomic Mass | %Weight = $\frac{\text{Mg}}{\text{Ca}+\text{Mg}} \times 100$ |
|----------------|-------------|-------------|------------|------------|-------------|--------------------|--|
| J0 | 9 | 0 | 20 | 33 | 6 | 1077.35 | 0.0 |
| J1 | 7 | 2 | 20 | 33 | 6 | 1045.80 | 14.8 |
| J2 | 5 | 4 | 20 | 33 | 6 | 1014.25 | 32.7 |

Table 4

Cont.

| | | | | | | | |
|---|---|---|----|----|---|--------|-------|
| J3 | 3 | 6 | 20 | 33 | 6 | 982.71 | 54.8 |
| J4 | 1 | 8 | 20 | 33 | 6 | 951.16 | 82.9 |
| J5 | 0 | 9 | 20 | 33 | 6 | 935.39 | 100.0 |
| Molecular Mass: Ca = 40.08, Mg = 24.31, H = 1.01, O = 16.00, Si = 28.09 | | | | | | | |

Figure 11 shows the traditional and modified structures of the single unit cell of C-S-H Jennite with different color representations to distinguish the atoms.

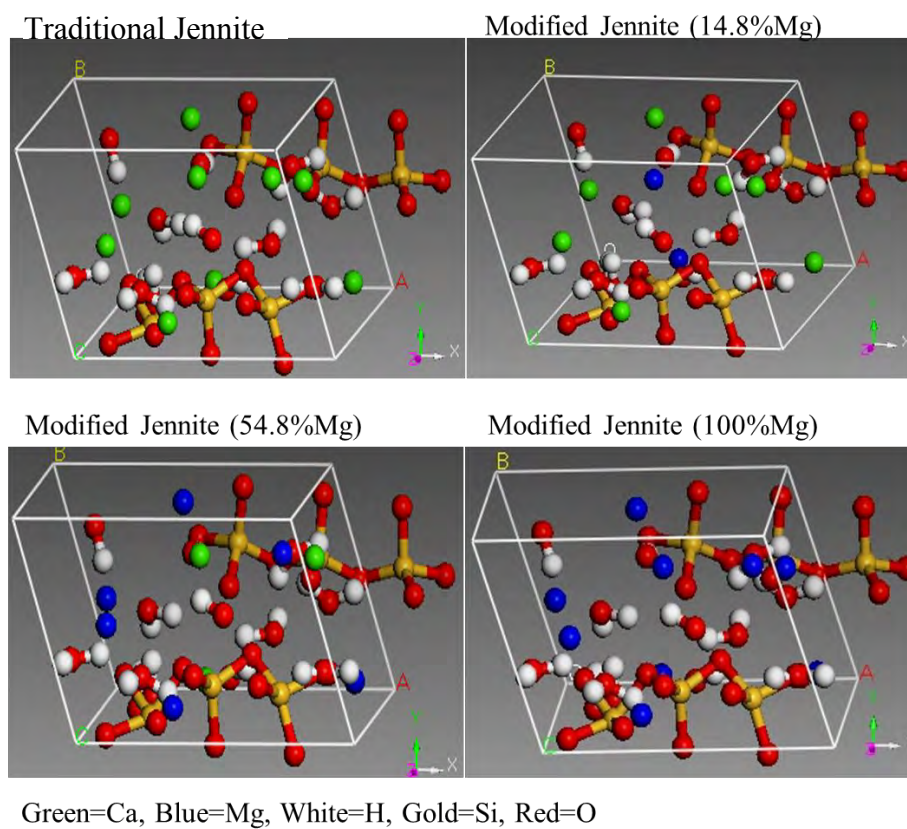


Figure 11. Traditional and modified Jennite structures.

A systematic MD analysis study of these different molecular structures was conducted. As discussed earlier, several computational MD simulation parameters were determined for this material system prior to full MD analysis. These different MD parameters that were investigated and established is discussed next.

3.4 Parameter Determination Analysis

There are several parameters that need to be established for specific material system when using MD simulations. Further, in Material Studio, the configurations for the specific material system need be established. Hence several preliminary MD simulation analysis runs were used to test and obtain the appropriate dynamics analysis time, appropriate pressure and temperature controls to be used as well as the appropriate material system size.

3.4.1 Dynamic time average. As discussed in the background sections, MD simulations are based on time-averaged values of the computed thermodynamic and physical properties of the molecular system. The longer the time dynamic duration of a MD simulation, the better the time average would be. However, in order to make effective use of the available and limited computational resources, an appropriate duration of the simulation must be established.

3.4.1.1 Determination of dynamic time. The dynamic simulation time was chosen based on the dynamics time duration of 100 ps, 200 ps and 300 ps. In order to choose an appropriate dynamic time for the C-S-H Jennite material system, the 1x1x1 unit cell of the traditional Jennite molecular structure was subjected to energy relaxation using COMPASS forcefield and NVT ensemble using different temperature controls. The dynamics time was obtained based on the convergence of the energy.

Figure 12, shows the energy fluctuation during the dynamics analysis for these different dynamic times durations with *Nosé* thermostat. As shown in *figure 12*, there was a good

convergence in the energy values for all these three dynamic durations. *Figures 12 and 13* (simulations run using Andersen and Velocity Scale thermostat) also showed good convergence for all the three transient dynamic analysis durations. However, with Berendsen thermostat as shown in *figure 14*, a longer dynamic time was required for the energy convergence. Based on the above simulation results, in order to provide a good accuracy and computational efficiency, the dynamic duration of 200 ps was chosen for all the full analysis studies. In the case of Magnesium modified Jennite, the systematic study of the dynamics time duration was performed with Universal Force Field and was found to show similar behavior as in the case of traditional C-S-H Jennite. See Appendix A1 for the NVT dynamics for the data on 54.8% Mg modified Jennite.

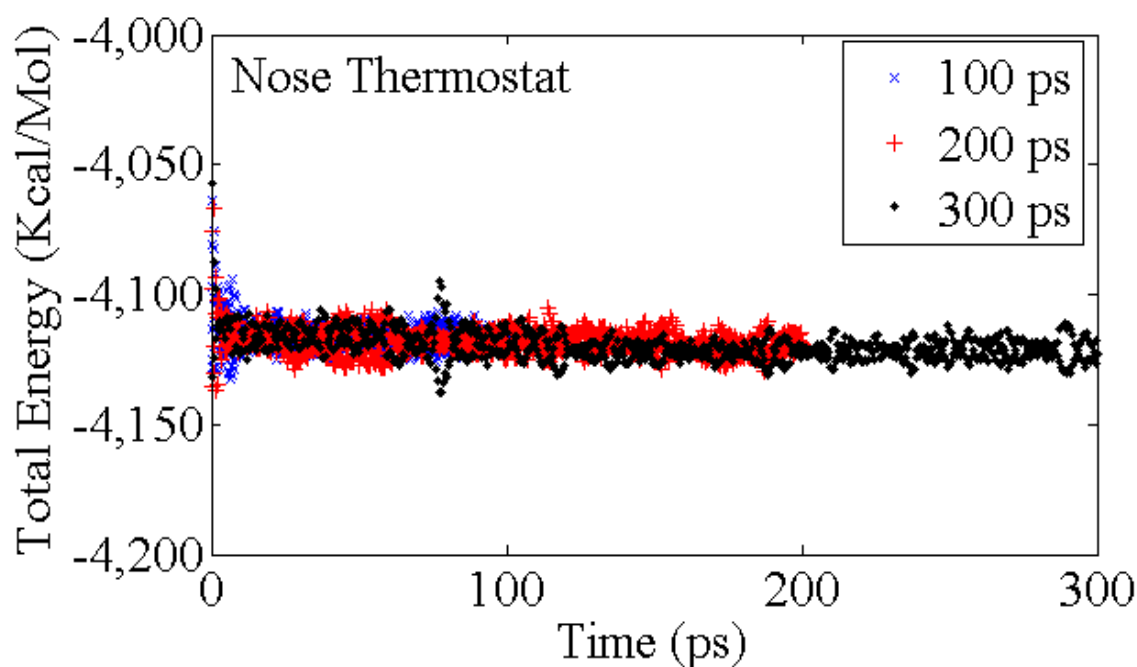


Figure 12. Total energy versus simulation time - *Nosé* thermostat

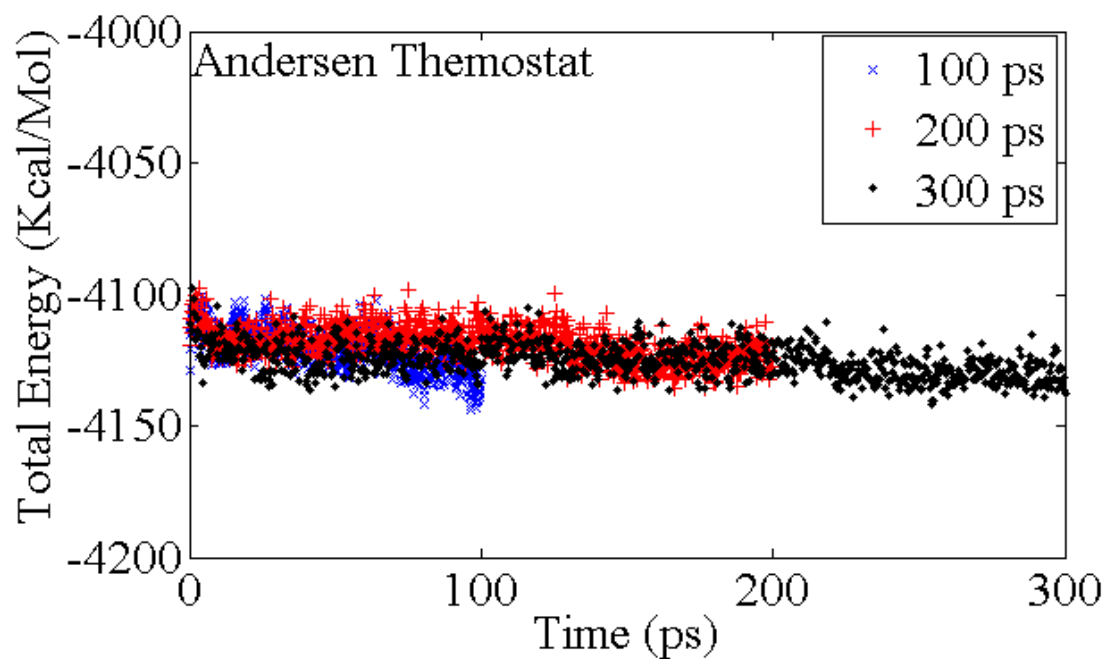


Figure 13. Total energy versus simulation time - Andersen thermostat

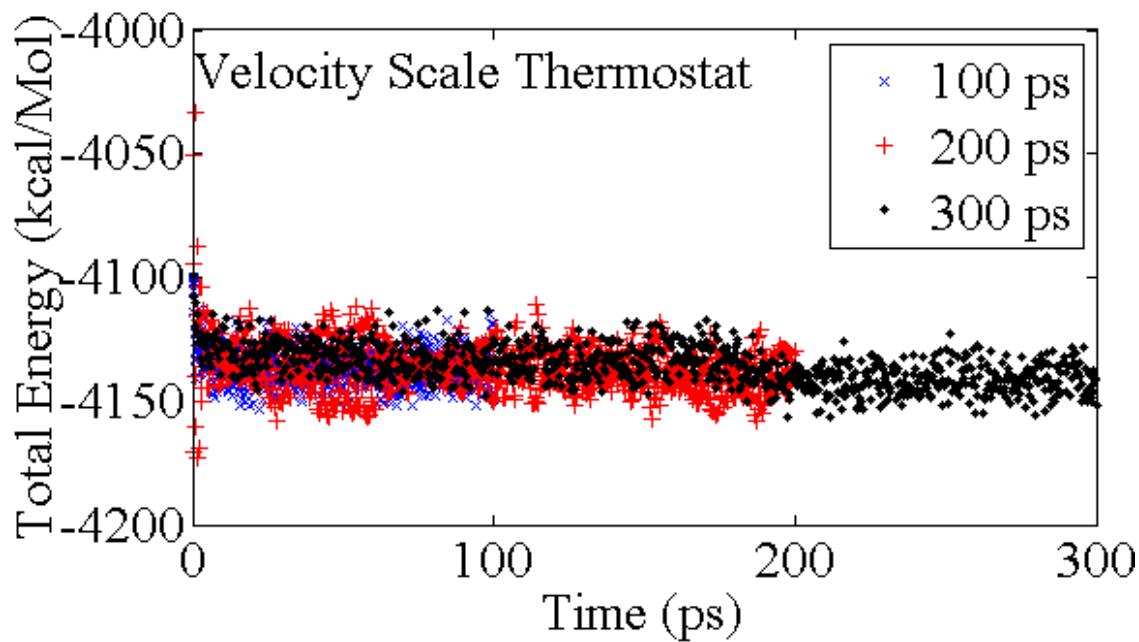


Figure 14. Total energy versus simulation time - Velocity Scale thermostat

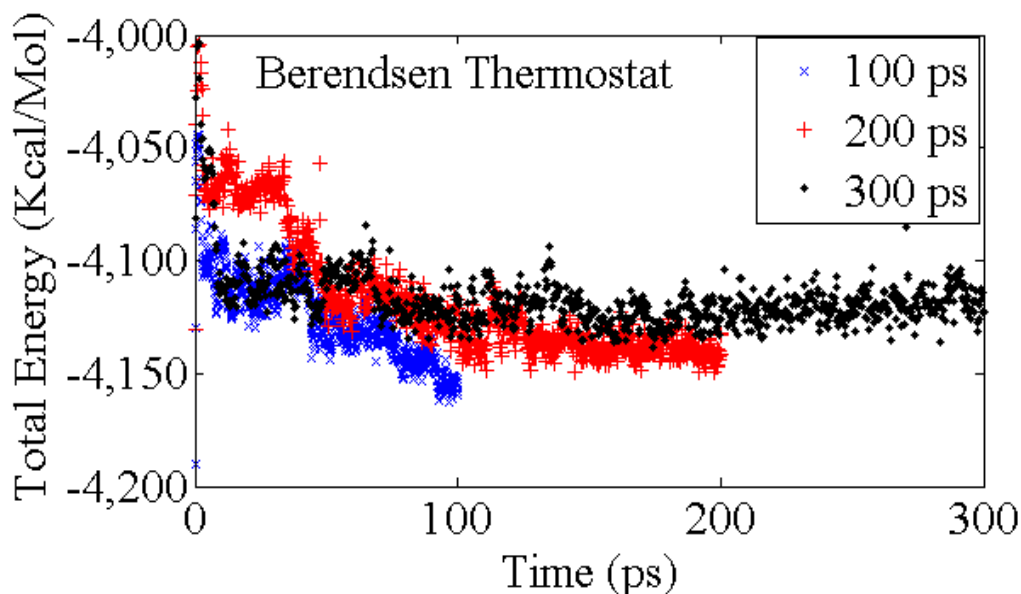


Figure 15. Total energy versus simulation time – Berendsen thermostat

3.4.2 Thermodynamic temperature and pressure control. The thermodynamic parameter of temperature and pressure in MD simulations is based on kinetic energy of the atom configurations. A stable temperature control is obtained by different computational temperature control methods. A choice needs to be made from the various temperature and pressure control algorithms that was discussed in section 2.3. In order to do this, MD system equilibration using NVT and NPT ensembles were used.

3.4.2.1 Determination of temperature control method. To determine the temperature control algorithm to be used, the NVT dynamic runs discussed earlier (*figures 12 to 15*) were used. From these figures, the dynamic energy fluctuations in *Nosé* thermostat tends to be smooth and less noisy than the Andersen and Velocity Scale thermostat. The Berendsen result showed a larger fluctuation and is noisy, and was not selected.

3.4.2.2 Determination of dynamic pressure control method. The already established dynamic time of 200ps and *Nosé* thermostat were used to determine the pressure control method to use. An NPT equilibration dynamics based on a single unit cell traditional Jennite, using COMPASS forcefield was conducted with different pressure control algorithms. The results are shown in the *figures 16 -18*.

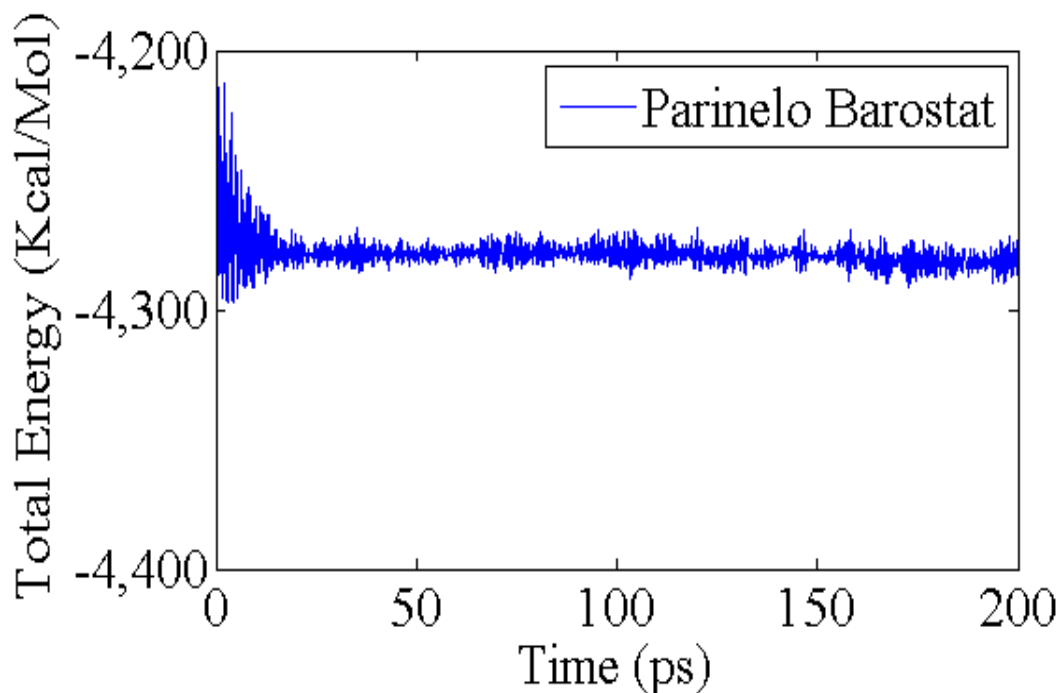


Figure 16. Total energy versus simulation time - Parinello barostat

It is seen that using the Parinello barostat provides a smoother and less noisy total energy profile during pressure equilibration than those from the Andersen and Berendsen barostat.

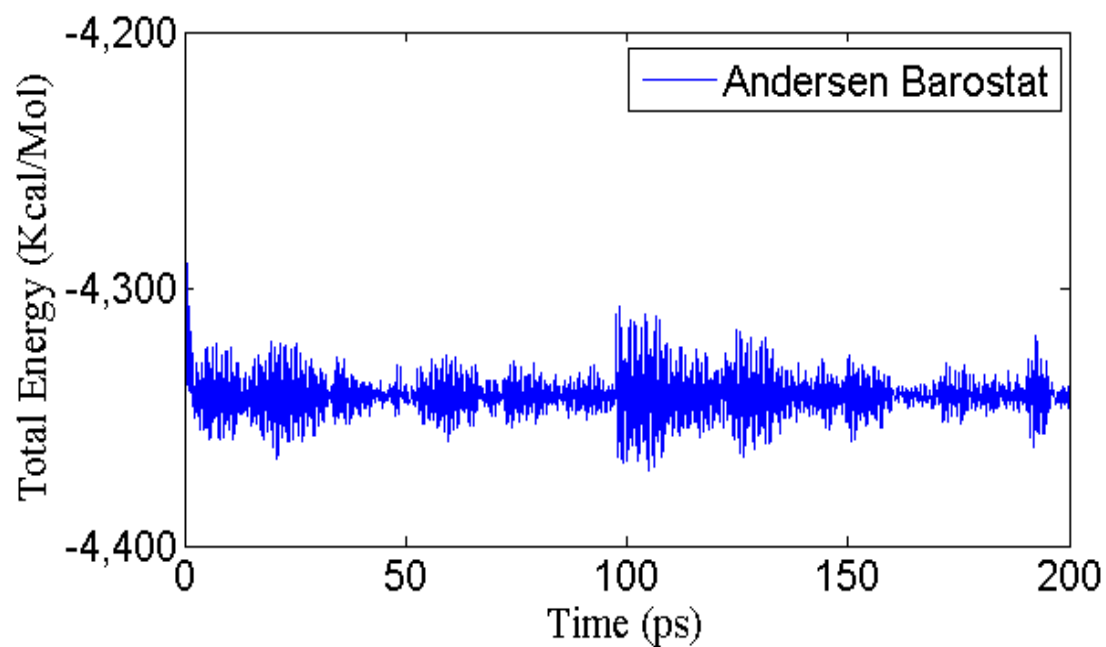


Figure 17. Total energy versus simulation time – Andersen barostat

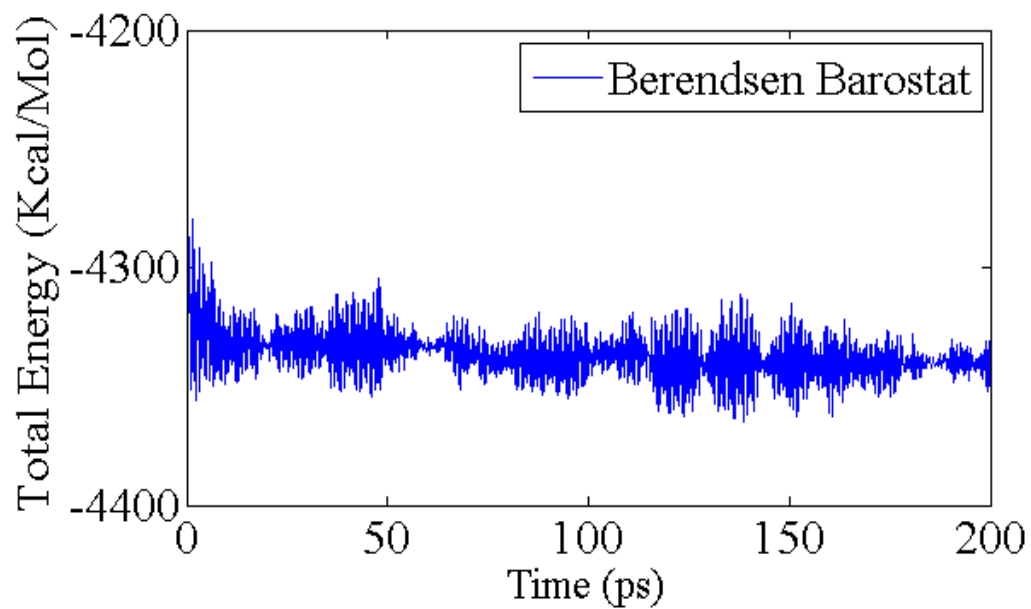


Figure 18. Total energy versus simulation time - Berendsen barostat

3.4.3 Material system size. The MD simulation uses periodic boundary conditions in order to minimize the boundary effects on boundary atoms, and simulate a larger material configuration. However, a critical system size that shows a convergence of the physical properties should be established for a given molecular system. In the present study, we seek a material system size that gives a good convergence on elastic stiffness modulus and total energies as the material system size increases. The appropriate cell size was chosen from the following possibilities using the MD simulations conducted for these sizes: 1 unit cell (1x1x1), 8 unit cells (2x2x2), 27 unit cells (3x3x3), 64 unit cells (4x4x4), and 125 unit cells (5x5x5).

3.4.3.1 Determination of material system size. In addition to a single unit cell configuration, 8 units, 27 units, 64 units and 125 units supercells were created from single unit cell traditional Jennite and one of the modified Jennite (54.8%Mg) in the present work. *Figure 19* shows the pictures of 1, 8 and 64 unit cells of 54.8% modified Jennite structure.

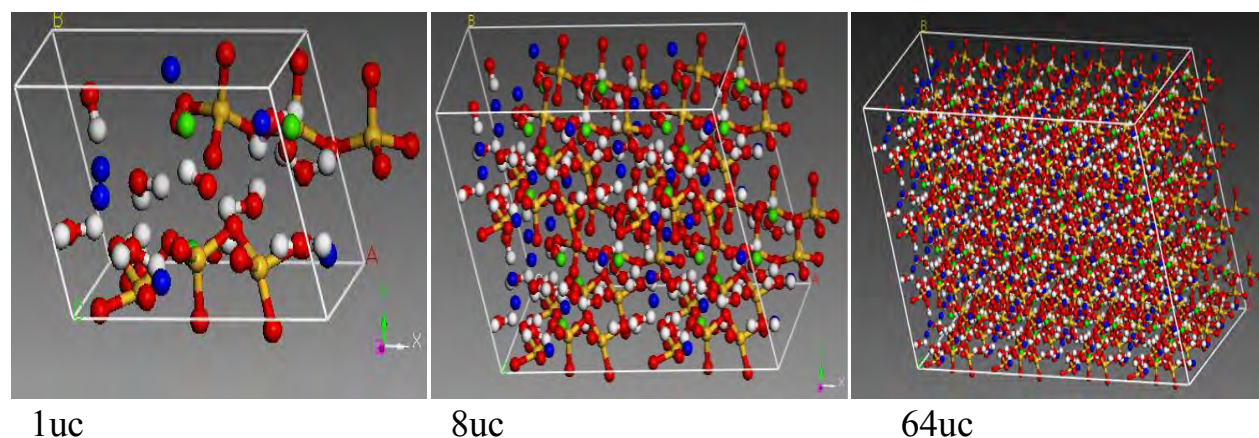


Figure 19. Material system sizes, 1, 8 and 64 unit cells of a Mg modified Jennite

All these different configurations for both traditional C-S-H Jennite and Magnesium modified C-S-H Jennite were employed for the MD analysis. The time averaged total energies

and the elastic moduli obtained were compared. *Figures 20 and 21* show that there is a convergence of the average total energies per Mol of the structure as the size increases.

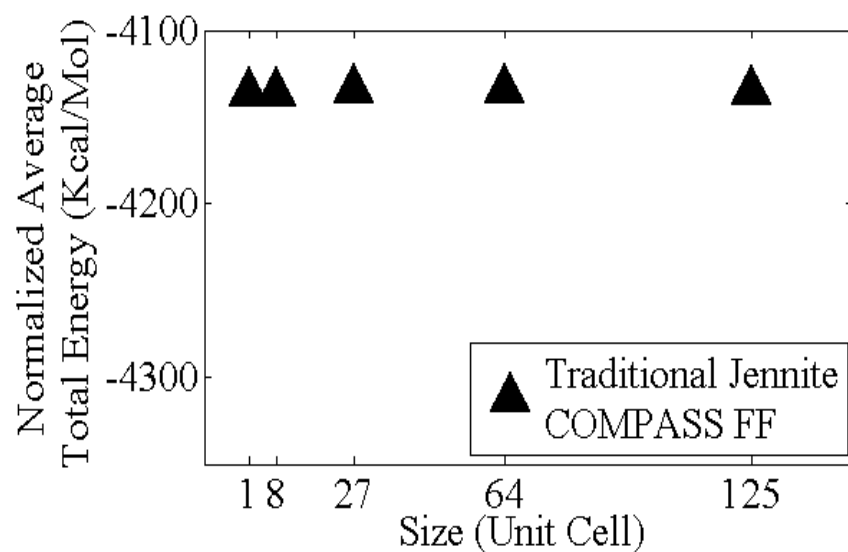


Figure 20. Normalized average total energy for traditional C-S-H structures: 1, 8, 27, 64, 125 unit cells

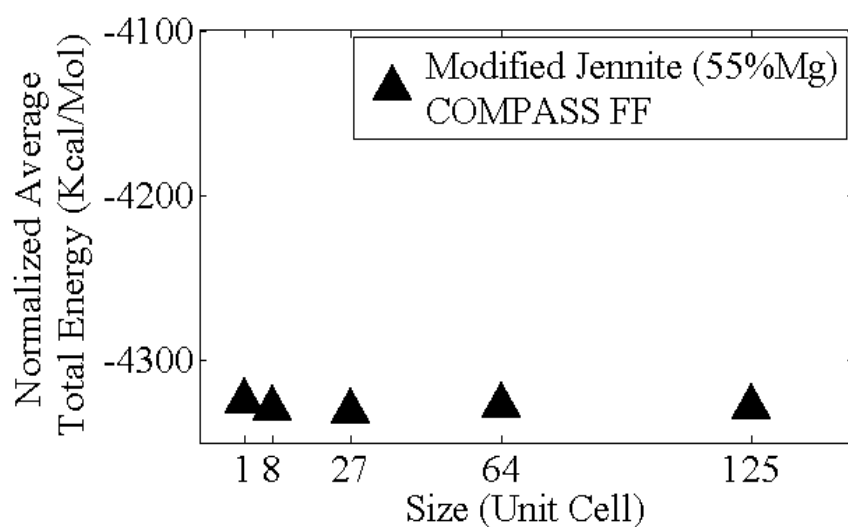


Figure 21. Normalized average total energy for 55%Mg modified structures: 1, 8, 27, 64, 125 unit cells

Likewise the elastic stiffness modulus, determined using the Hill average, shows that as the size of the cell increases the moduli converges for both traditional and modified Jennite. See *figures 22 and 23*.

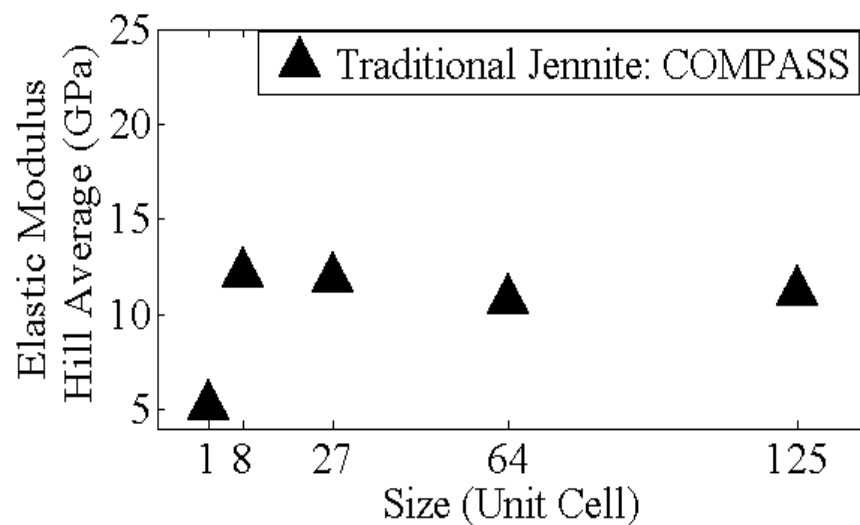


Figure 22. Elastic stiffness modulus (Hill average) for traditional C-S-H structures: 1, 8, 27, 64 and 125 unit cells.

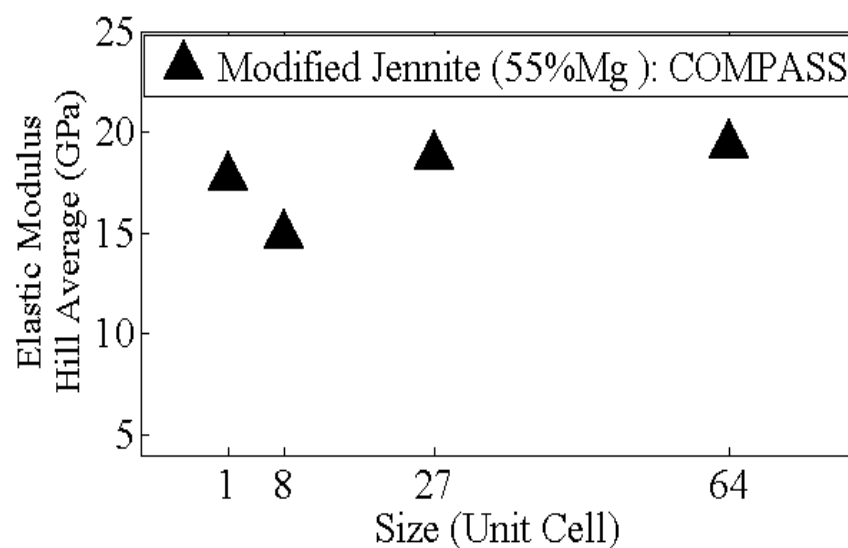


Figure 23. Elastic stiffness modulus (Hill average) for 55%Mg Modified C-S-H structures: 1, 8, 27 and 64 unit cells

From *figures 20-23*, the system size of 64 unit cells was chosen as the size of the material molecular structure configuration to work with in future MD analysis simulations for the material modeling. This material system size showed good convergence and is within the computational capacity available to us in the present time. This molecular system size will be sufficient to handle the dynamics analysis within reasonable computational time, while giving reliable results to understand the effect of magnesium ion exchanges.

3.4.4 Influence of forcefield. As discussed earlier on the background of MD, the choice of forcefield plays an important role in the fidelity of results obtained from MD simulations. Hence in order to choose between the UNIVERSAL and COMPASS forcefields, a NVT dynamic simulation was performed on two of modified and traditional Jennite structures using the 64 unit cell size, *Nosé* thermostat and 200ps dynamics analysis time, results obtained is shown in *figure 24*.

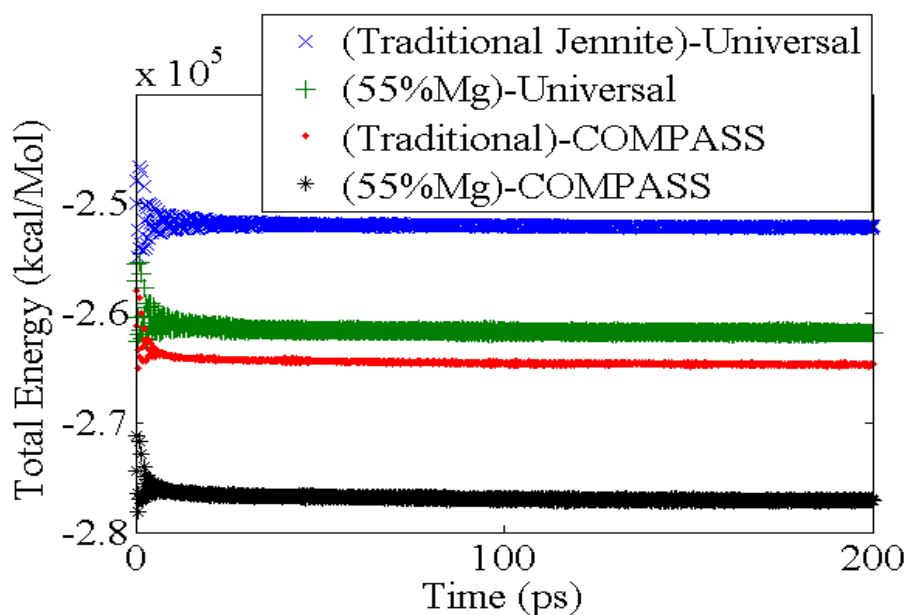


Figure 24. Total energy profile for 64 unit cell traditional and modified Jennite (55%Mg) using COMPASS and universal forcefields.

From *figure 24*, the values of the total energy for the traditional Jennite and the 55% modified Jennite when Universal forcefield was used is higher than the values obtained when COMPASS forcefield was used. Other modified structures were also studied using the same MD simulation analysis with both forcefields. Similar result is obtained when 33% modified Jennite (*figure 25*) and 83% modified Jennite (*figure 26*) were used.

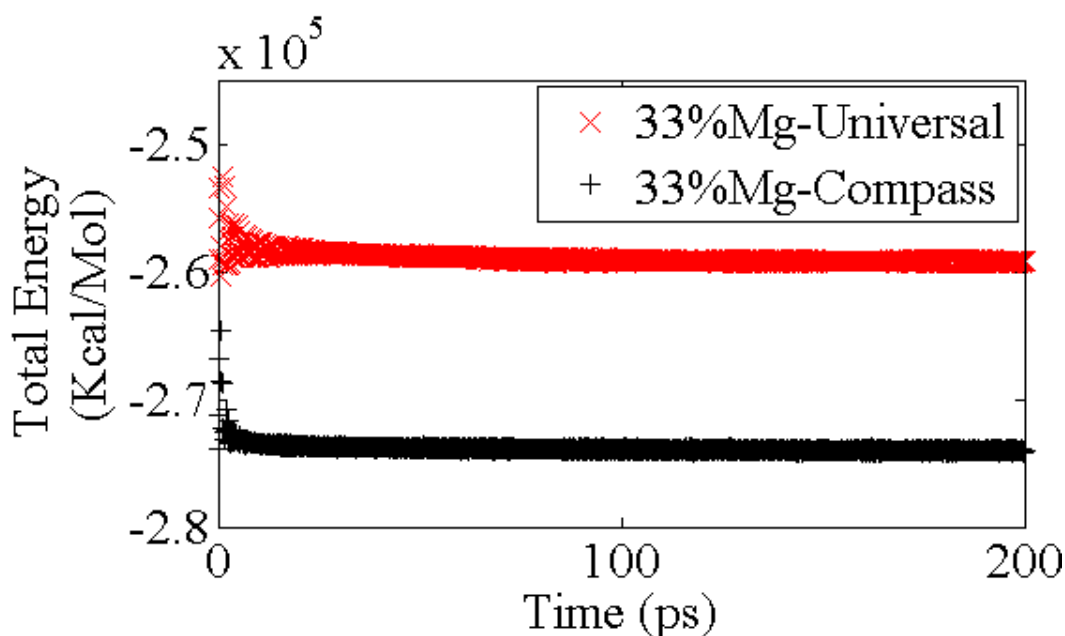


Figure 25. Total energy profile for 64 unit cell traditional and modified Jennite (33%Mg) using COMPASS and UNIVERSAL forcefields.

In all the cases, it was also observed that the COMPASS forcefield profile appears smoother with less noise fluctuations when both forcefield were plotted on the same scales *figures 24-26*. Based on these, COMPASS forcefield was chosen and used in the material property determinations as discussed in Chapter 4.

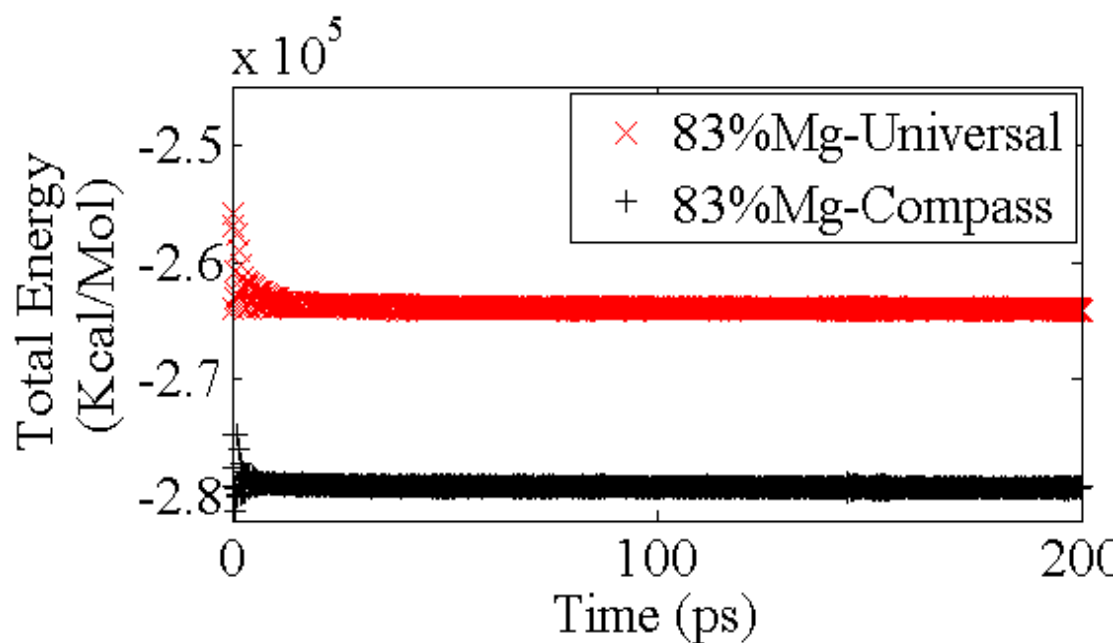


Figure 26. Total energy profile for 64 unit cell traditional and modified Jennite (83%Mg) using COMPASS and universal forcefields.

3.4.5 MD parameters summary. Following the above discussions, in summary, the parameters used for the mechanical property determination and shear deformation studies to understand the influence of Magnesium ion exchanges in the current work are;

- Dynamic time: 200 ps
- Thermostat: *Nosé*
- Barostat: Parinello
- Cell size: 64 unit cell
- Forcefield: COMPASS

CHAPTER 4

Results and Discussions

The focus of the present work is to understand the effect of magnesium ion exchange in traditionally calcium based C-S-H on mechanical stiffness properties and the shear deformation behavior following the material modeling methodology outlined in chapter 2. These are now presented and discussed in this chapter.

4.1 Elastic Stiffness Modulus

The MD modeling analysis parameters obtained and discussed in chapter 3 were used to investigate the influence of the Magnesium inclusion and ion exchange using the 64 unit cell structure of C-S-H Jennite structure at a temperature of 298K. The elastic modulus, mechanical properties for the traditional calcium based and the various magnesium based molecular configurations of C-S-H Jennite were obtained. *Figure 27* shows the initial and final molecular structures - after dynamics simulations on the systems.

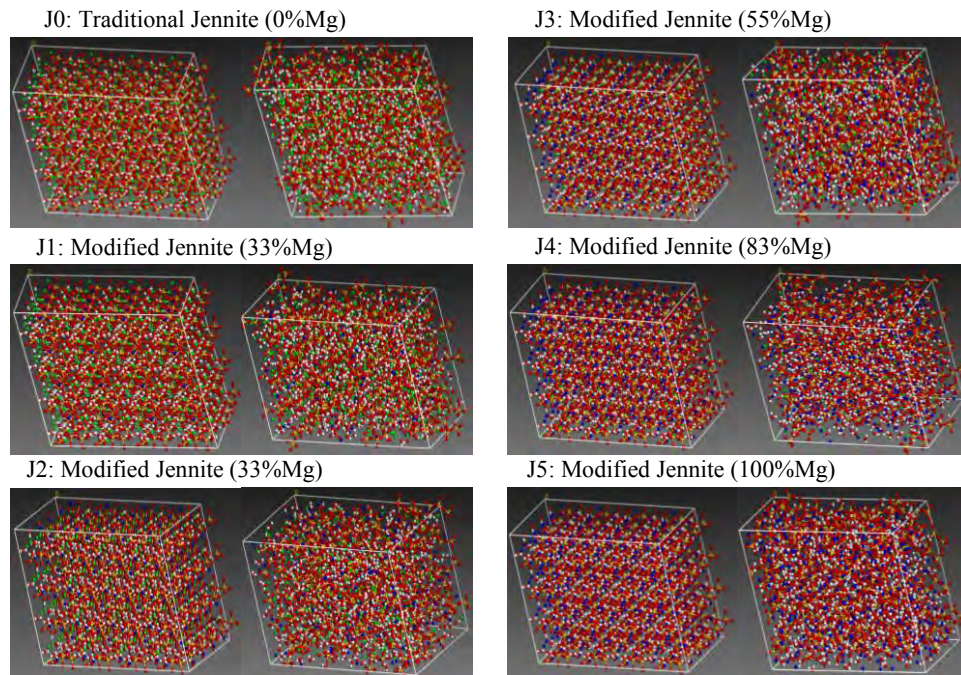


Figure 27. Initial and final Jennite structures – Traditional and Mg Ion Exchanged C-S-H

Figure 28 shows the average total energy for various magnesium modified C-S-H structures as a function of various magnesium percentages in the modified C-S-H structures.

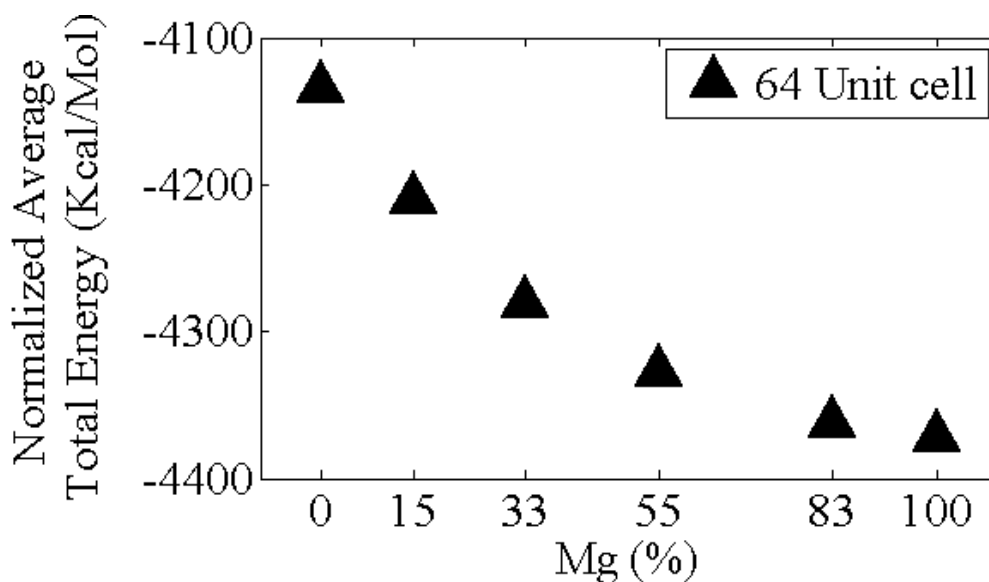


Figure 28. Change in total energy per mole for various Mg ion exchange percentages

The elastic moduli was determined using Hill's averages for the traditional and Magnesium ion exchanged 64 unit cell C-S-H Jennite structures. Figure 29 shows the variation in the predicted elastic moduli with COMPASS forcefield following the MD based material modeling methodology.

Latter studies, involving Calcium ion replacement of all 1 to 9 calcium atoms was also performed to obtain mechanical stiffness properties for other calcium replacement percentages of 7%, 23%, 43% , 68%Mg, and 100% Mg. In addition to this; statistical analysis with 95% confidence level was performed to obtain the number of different variations of each modified structures (with respect to location of the calcium ion replaced) that is required to have a 95% confidence level, and was analyzed. Appendix A2 shows the table of all variants obtained.

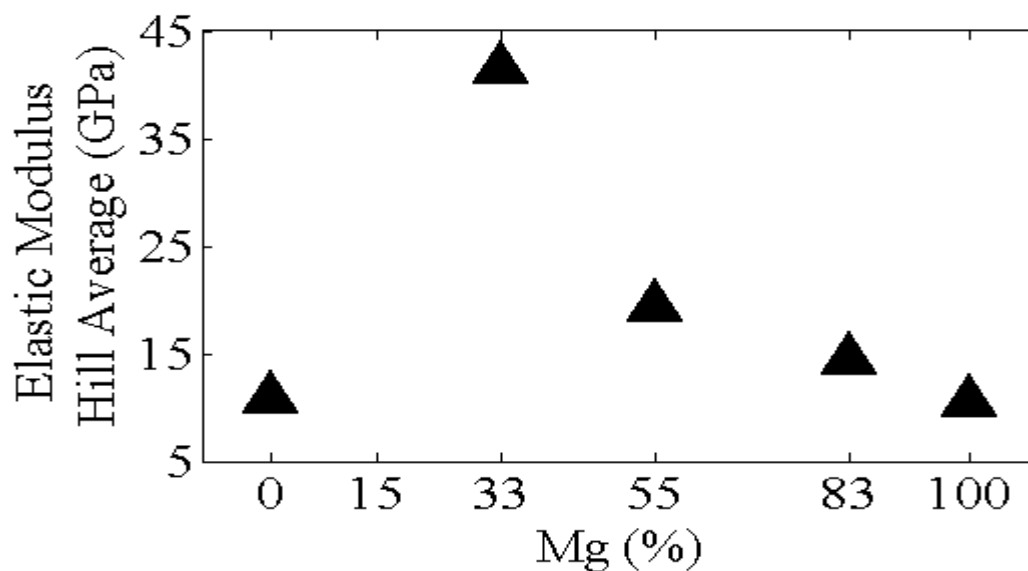


Figure 29. Predicted elastic modulus (Hill Average) for various Mg ion exchange percentages of 64 unit cell C-S-H Jennite structures-COMPASS forcefield.

Figure 30 shows the mean values of the normalized average total energies for all the Mg ion exchange percentages in C-S-H Jennite structure. The errors associated with the energies are very small and not visible from *figure 30*. Appendix A3 show the table of the result of the total energies and the corresponding error associated with each Mg modified structure following the statistical analysis of the atom locations employed for the magnesium exchange.

In the same manner, the various variants of the Mg modified Jennite were also used to obtain the elastic stiffness modulus, and *figure 31* shows the mean values of the elastic modulus versus the %Mg.

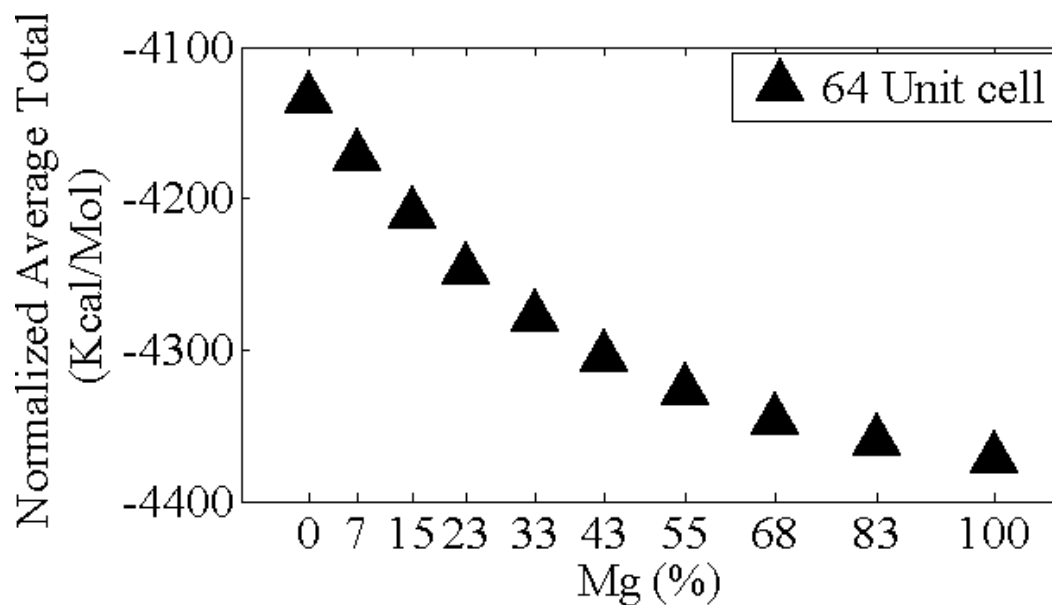


Figure 30. Total energy per mole for various Mg ion exchange percentages.

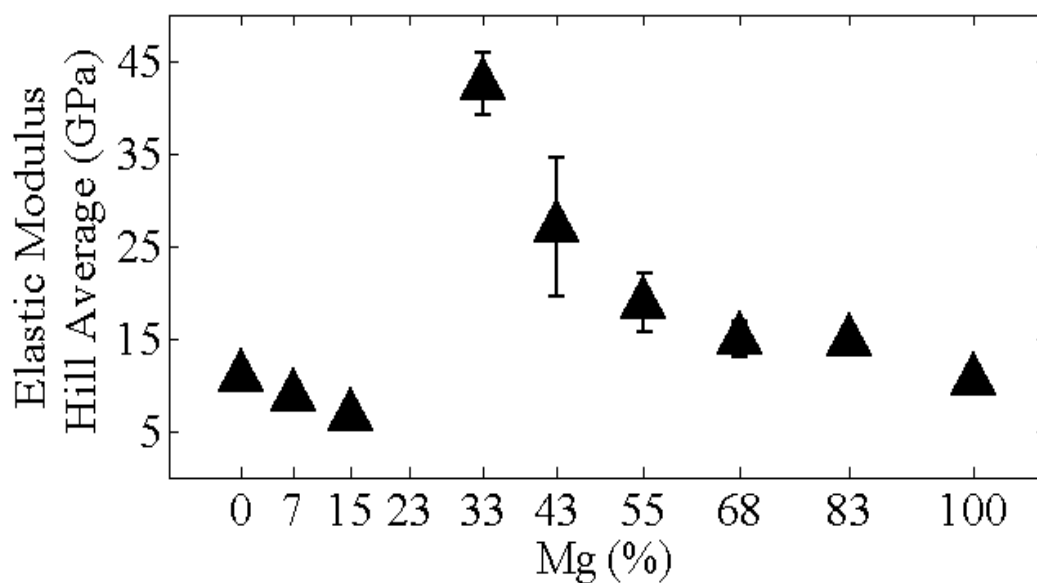


Figure 31. Predicted elastic modulus (Hill Average) for various Mg ion exchange with the variants and associated errors-COMPASS forcefield.

The variation in the predicted elastic modulus values presented in *figure 29* shows a sharp increase in the elastic modulus of Jennite from the traditional for 33% magnesium ion exchange,

followed by reduction in the elastic modulus as the percentage of the magnesium increases further.

The values of the predicted mechanical and other material properties depend on the forcefield that defines the energy of the molecular level interactions. A slightly different result with higher values was observed when universal forcefield was used to determine the elastic moduli. *Figure 32* shows the variation in the predicted modified elastic modulus for different magnesium ion exchange percentages using universal forcefield.

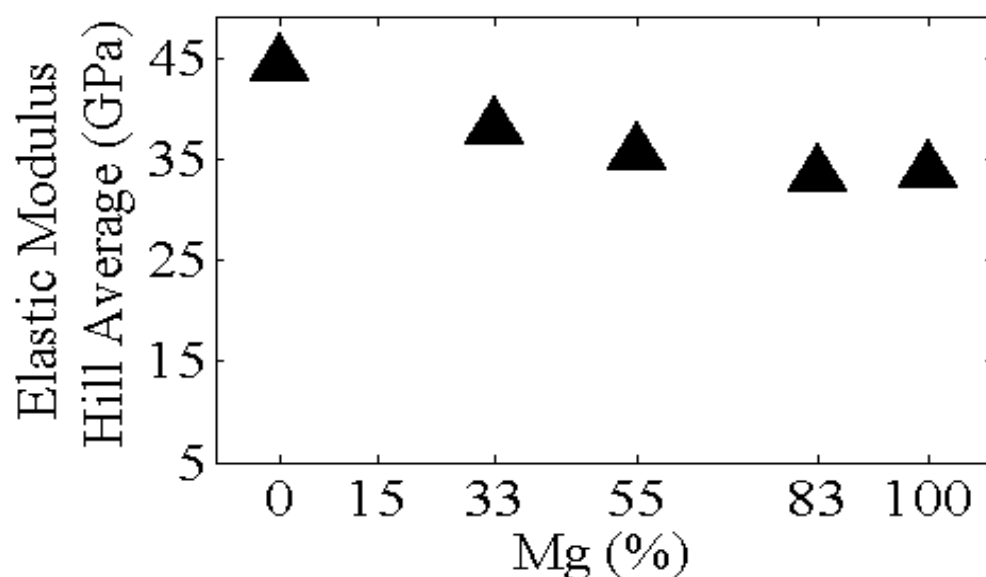


Figure 32. Predicted elastic modulus (Hill Average) for various Mg ion exchange percentages of 64 unit cell C-S-H Jennite structures-Universal forcefield.

The corresponding predicted bulk and shear modulus and the as well as the Poisson's ratio were obtained and are presented in *figures 33-35* below. Negative values obtained for the predicted bulk moduli and Poisson's ratios are based on the mechanics based theories of defined effective bulk modulus from compliance matrix as discussed in Chapter 2 and needs further investigation.

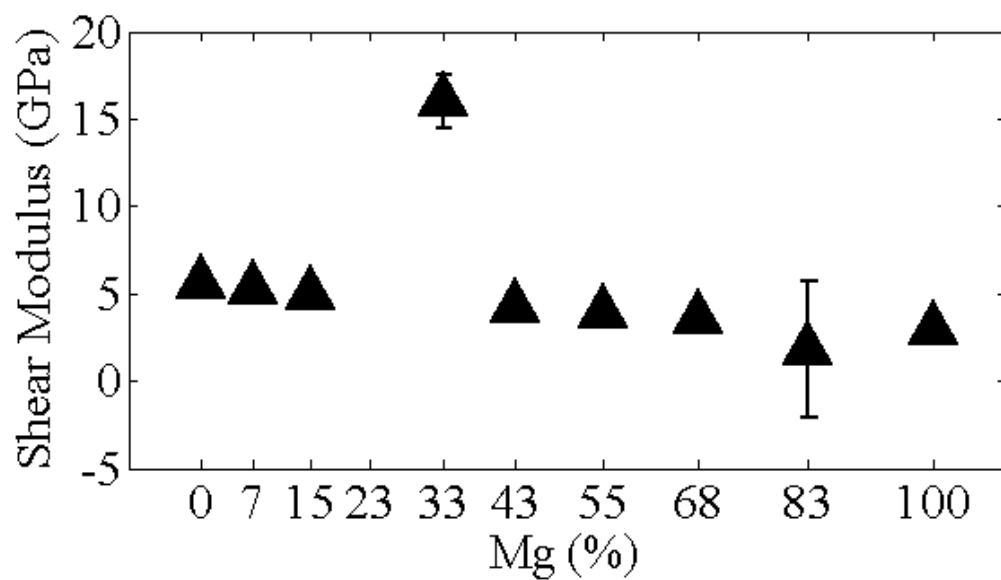


Figure 33. Predicted shear modulus (Hill Average) variations for various magnesium ion exchange percentages studied.

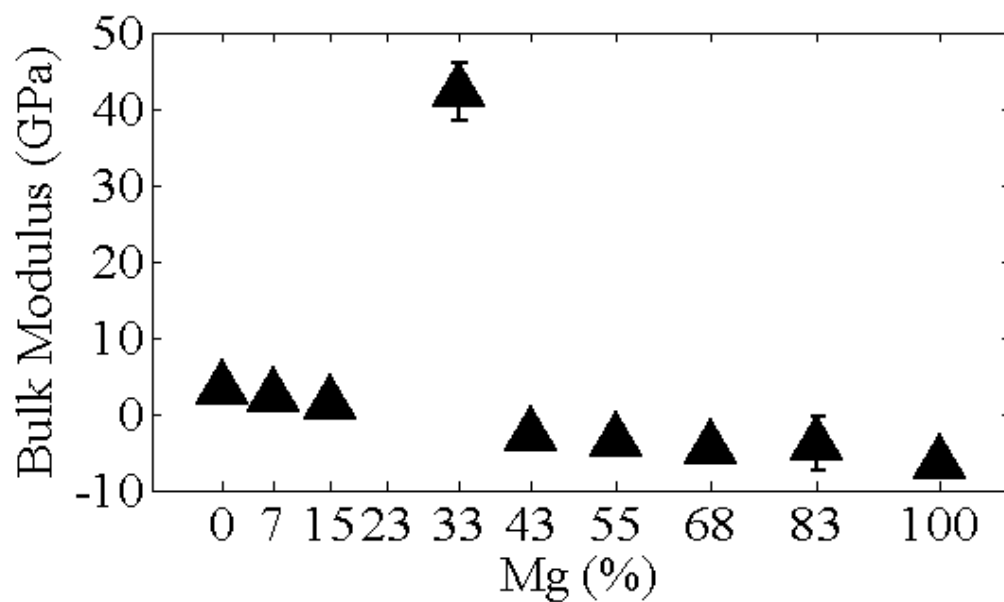


Figure 34. Predicted bulk modulus (Hill Average) variations for various magnesium ion exchange percentages studied.

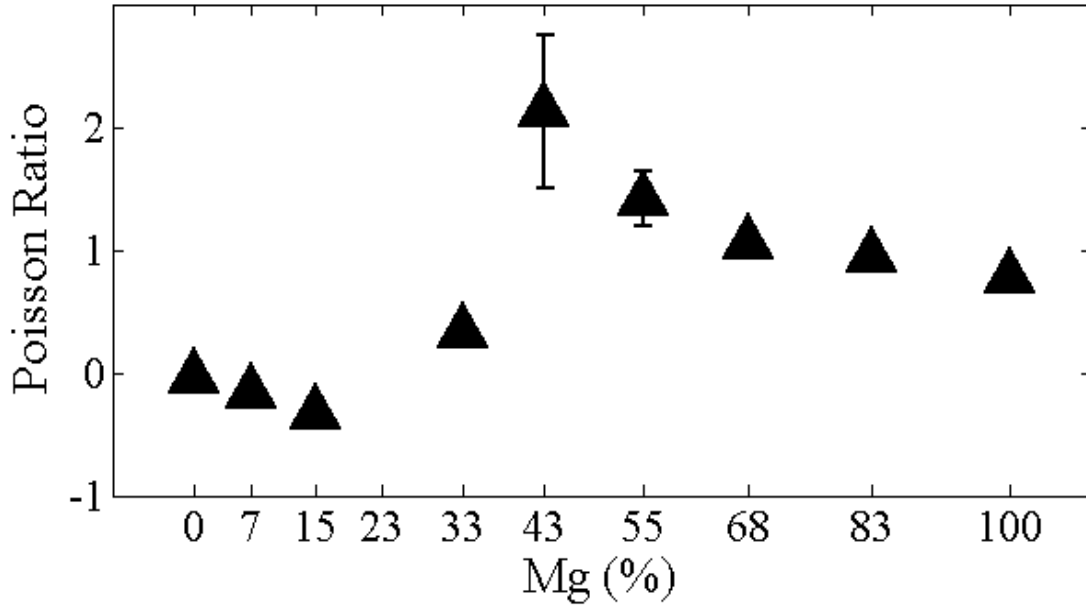


Figure 35. Predicted Poisson ratio (Hill Average) variations for various Magnesium ion exchange percentage studied.

4.1.1 Mechanical properties summary. Elastic modulus investigation showed that material chemistry does affect structural material stiffness modulus properties, and varies as the amount of Mg inclusion increases. These predicted material properties are based on MD simulations and material chemistry level modeling and thus provides an effective computational methodology to understand the expected variations due to material chemistry changes such as due to Magnesium ion exchange of C-S-H Jennite. Further investigation is needed to explain some of the non-physical computational modeling values noted in the predicted values of bulk modulus and Poisson's ratio that are based on mechanics based approximations following the compliance matrix definitions in MD simulation analysis.

The prior MD material modeling predictions are based on the time averaged values of the modulus values from derivatives of energy as defined in chapter 2 for effective values of material stiffness modulus. Engineering scale properties of interest is the stress-strain

deformation behavior and effective prediction of estimated stress-strain behavior due to material chemistry changes in the systems, such as those discussed due to Magnesium exchange in C-S-H Jennite. In the present work, the influence of magnesium exchange on shear deformation of C-S-H Jennite molecular structure is studied. Details of the shear deformation with emphasis on the Magnesium ion exchanged C-S-H Jennite is presented next.

4.2 Shear Deformation

Shear deformation was implemented by imposing a constant volume angular deformation change on each crystallographic plane of the triclinic C-S-H Jennite structure and the Magnesium modified systems. In the shear deformation process, the C-S-H molecular structures were subjected first to NPT conditions. Then, they were subjected to an incremental angular change making sure the volume remains constant defining the shear deformation process as outlined in chapter 2. The resulting structure was relaxed after which an NVT dynamic analysis for each of the deformed structural configuration was performed to obtain the corresponding stress value following the Virial definition of shear stress. The shear deformation process was applied to all three triclinic faces of C-S-H Jennite as shown in *figure 36*.

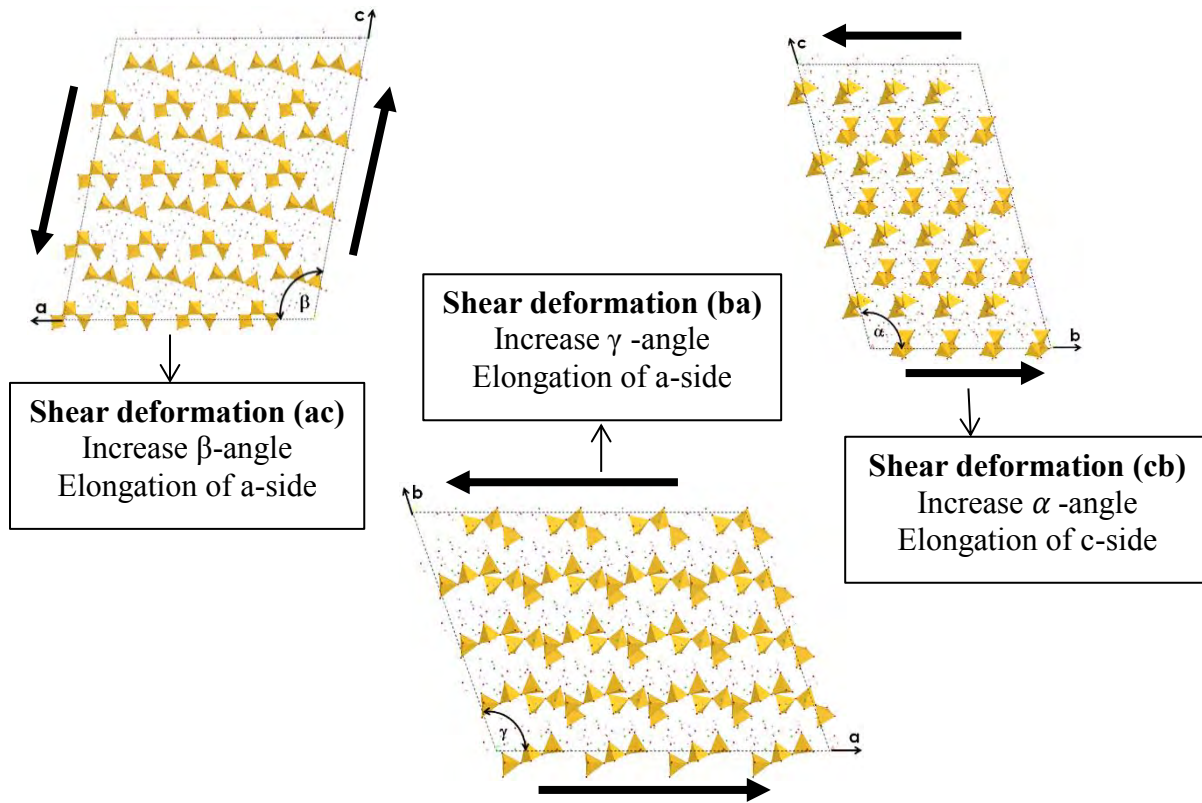


Figure 36. Shear deformation modeling along three crystallographic planes of triclinic C-S-H structure.

The schematics presented *Figure 37* shows the procedure of the MD modeling analysis for the shear deformation. To define the complete shear deformation process, the original and quasi-static deformation of the triclinic structure was performed for 75 different sheared configurations. Each shear deformed configuration provides the corresponding shear stress, associated strain for each of the deformed configuration due to shearing along the three surfaces of the triclinic traditional and modified C-S-H structures.

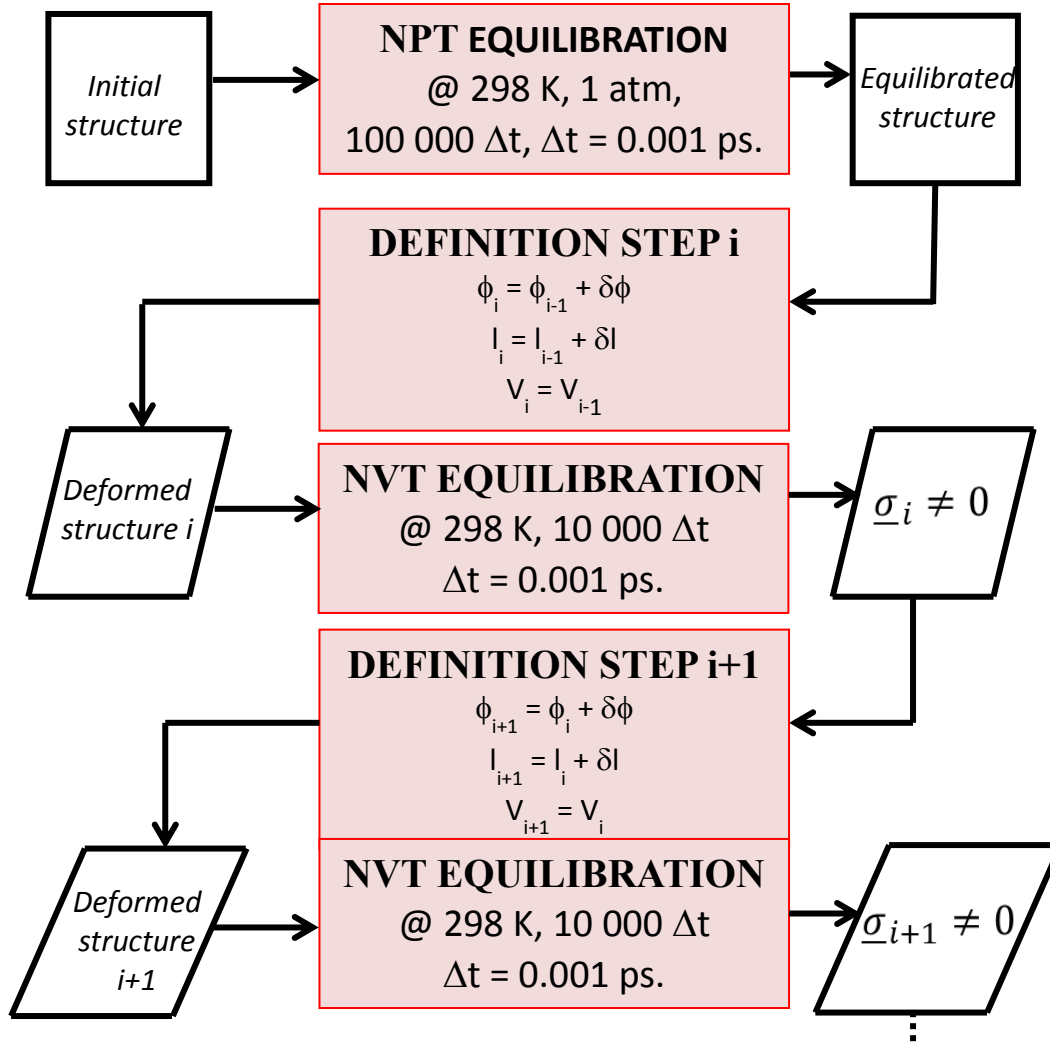


Figure 37. MD implementation of shear deformation. Showing an NPT relaxation of the initial structure, followed by an incremental angular change - the deformation step, corresponding NVT equilibration of the deformed structure to obtained the shear stress of the deformed structure and continuation of the iterative process.

In the present work, two of the Magnesium ion exchange modified structures were analyzed (33%Mg and 83%Mg) in addition to the traditional Jennite which had been obtained earlier in our research group [50]. Shear stress-strain deformation on the three shearing planes *cb*, *ba* and *ac* of the triclinic C-S-H system were studied and compared.

4.2.1 Shear deformation, *cb*-plane. *Figures 38-40* shows the MD modeling predicted shear stress-strain curves for the shear deformation along the *cb*-plane for the traditional C-S-H, 33% magnesium modified C-S-H and 83% magnesium modified C-S-H Jennite structures respectively.

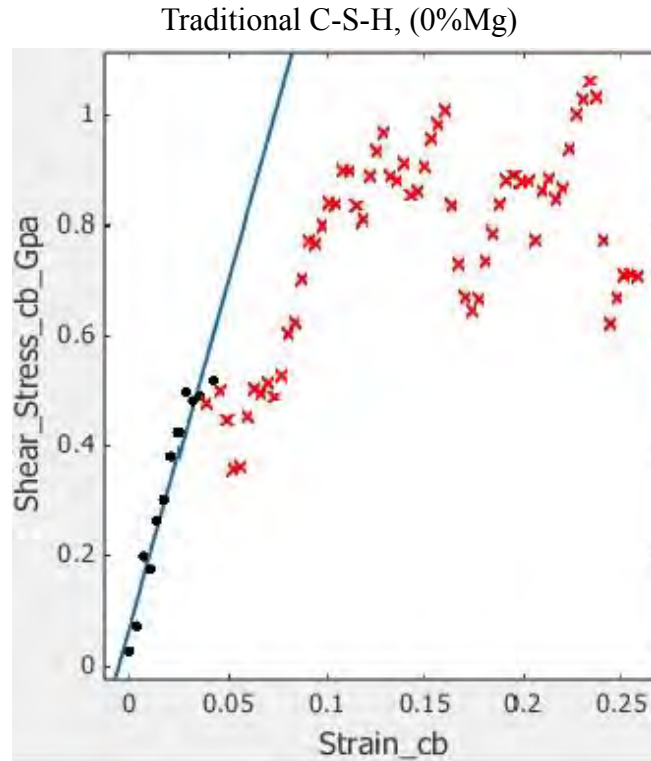


Figure 38. Predicted Shear Stress-strain deformation behavior for shearing along the *cb*-plane for traditional Jennite. Ref [50]

Employing the predicted stress-strain deformation behavior, shear modulus was obtained, as the slope of the linear region of the shear stress – strain deformation behavior shown in *figure 38-40*. The ultimate shear stress was defined as the maximum stress observed within the shear strain of the shearing deformation studied.

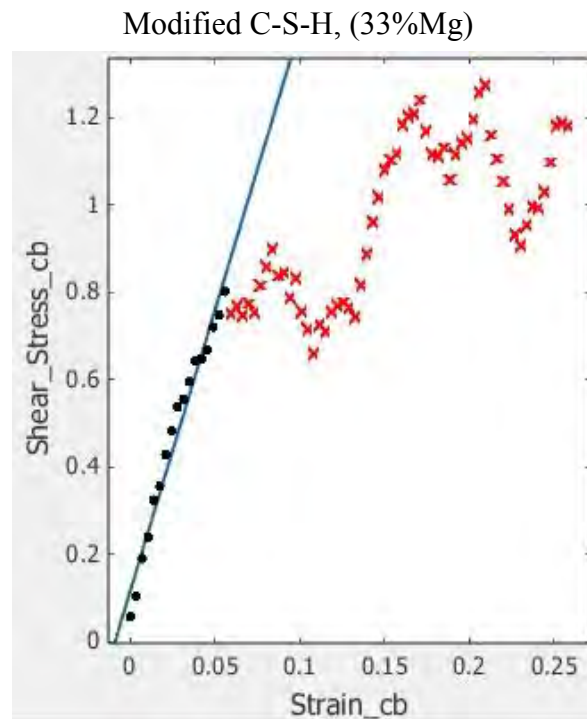


Figure 39 . Predicted Shear Stress-strain deformation behavior for shearing along the *cb*-plane for 33% magnesium modified Jennite

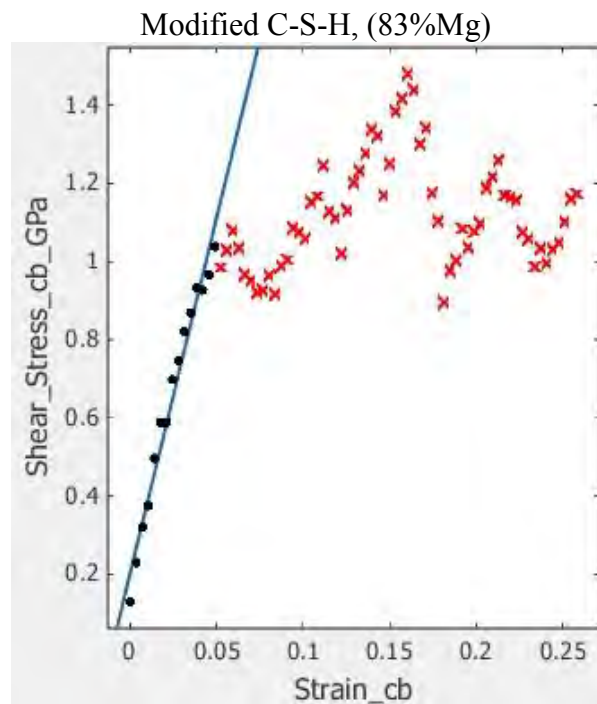


Figure 40. Predicted Shear Stress-strain deformation behavior for shearing along the *cb*-plane for 83% magnesium modified Jennite

The MD material modeling predicted values for shear modulus, strength and ultimate shear stress is presented in *table 5*. These engineering material properties for traditional C-S-H and magnesium modified Jennite have been solely obtained from MD modeling analysis of the material chemistry structure and provides an effective material modeling methodology to understand the estimated variations in the stress – strain deformation behavior due to material chemistry changes.

Table 5

Shear Modulus, Strength and Maximum Shear Deformation of cb-plane

| Plane- CB | 0%Mg | 33%Mg | 83%Mg |
|-----------------------|----------|-------------|--------------|
| Shear Modulus (GPa) | 11.0±2.4 | 12.88± 1.21 | 18.19 ± 1.75 |
| Shear Strength (GPa) | 0.5193 | 0.8014 | 1.038 |
| Ultimate Stress (GPa) | 1.1 | 1.275 | 1.48 |

The plot of the shear moduli and the ultimate shear stress is also presented in *figures 41* and *42*. It is observed that as the percentage of Magnesium increases, these two predicted material properties also show an increase for shear deformation of *cb-plane*.

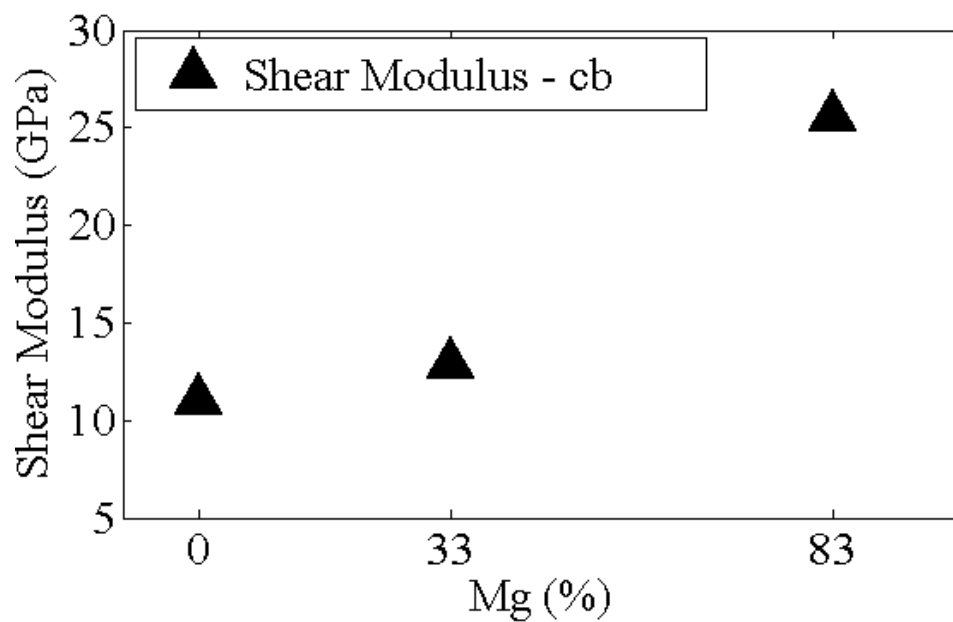


Figure 41. Shear Modulus variations due to Mg Ion Exchange, *cb*-plane

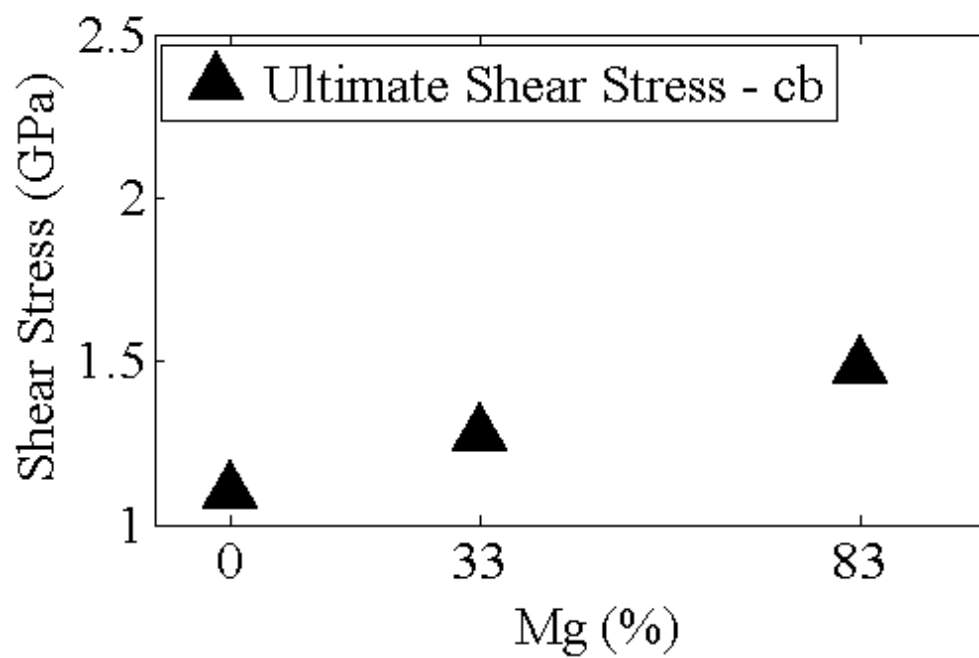


Figure 42. Ultimate shear stress variations due to Mg Ion Exchange, *cb*-plane

Shear deformation of the traditional and Magnesium modified C-S-H Jennite along other crystallographic planes is presented next.

4.2.2 Shear deformation, *ba*-plane. Shear stress – strain deformation behavior due to shearing along the crystallographic *ba*-plane is presented in *figures 43-45* for traditional and Magnesium modified C-S-H.

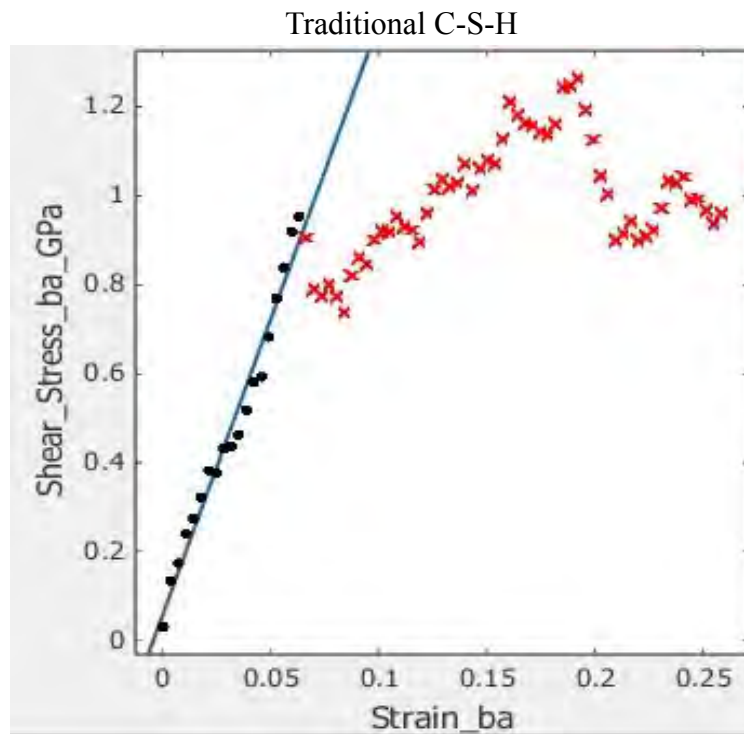


Figure 43. Predicted Shear Stress-strain deformation behavior for shearing along the *ba*-plane for traditional Jennite. Ref [50]

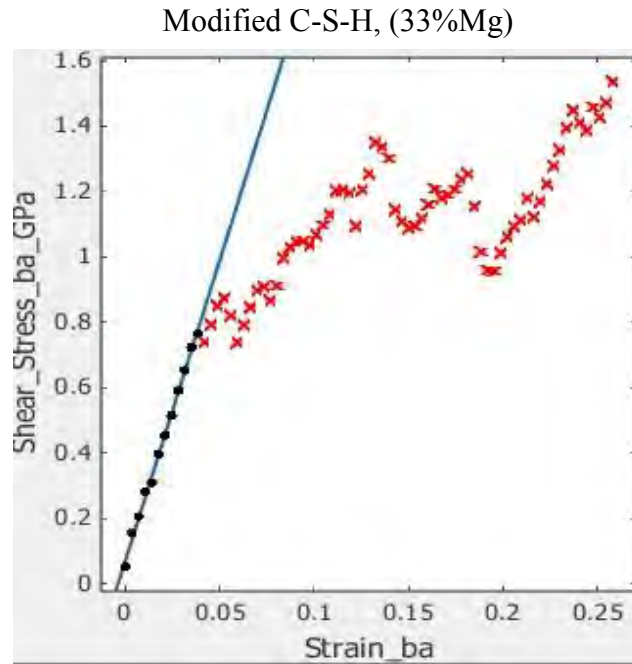


Figure 44. Predicted Shear Stress-strain deformation behavior for shearing along the ba -plane for 33% magnesium modified Jennite

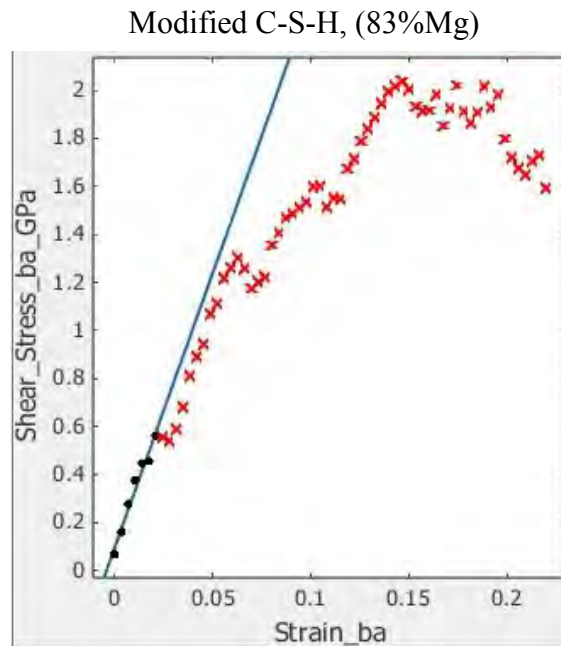


Figure 45. Predicted Shear Stress-strain deformation behavior for shearing along the ba -plane for 83% magnesium modified Jennite

The corresponding shear moduli and ultimate shear stress obtained for shear deformation along *ba*-plane is presented in figures 46 and 47.

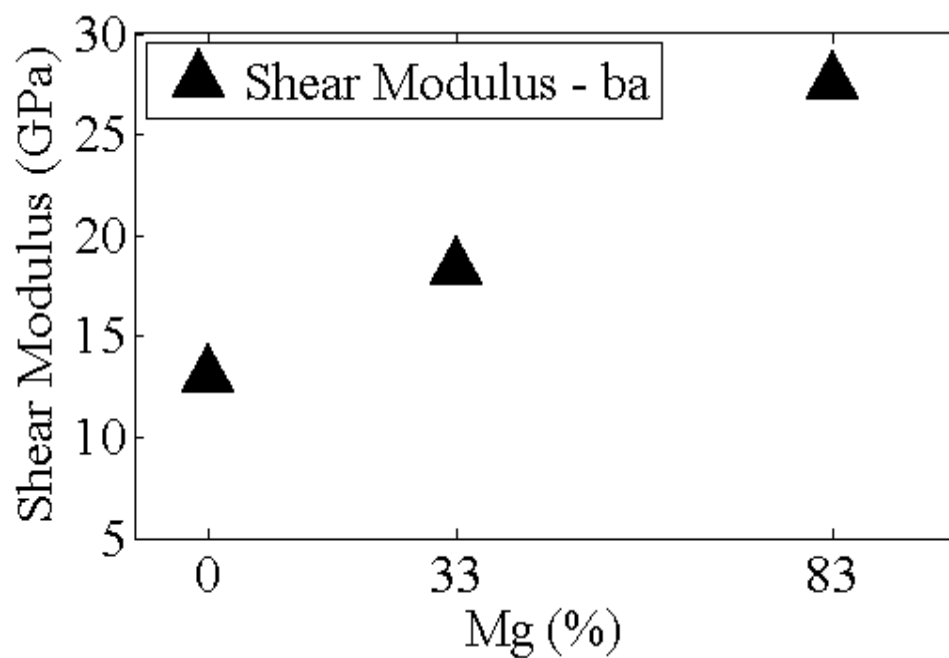


Figure 46. Shear Modulus variations due to Mg Ion Exchange, *ba*-plane

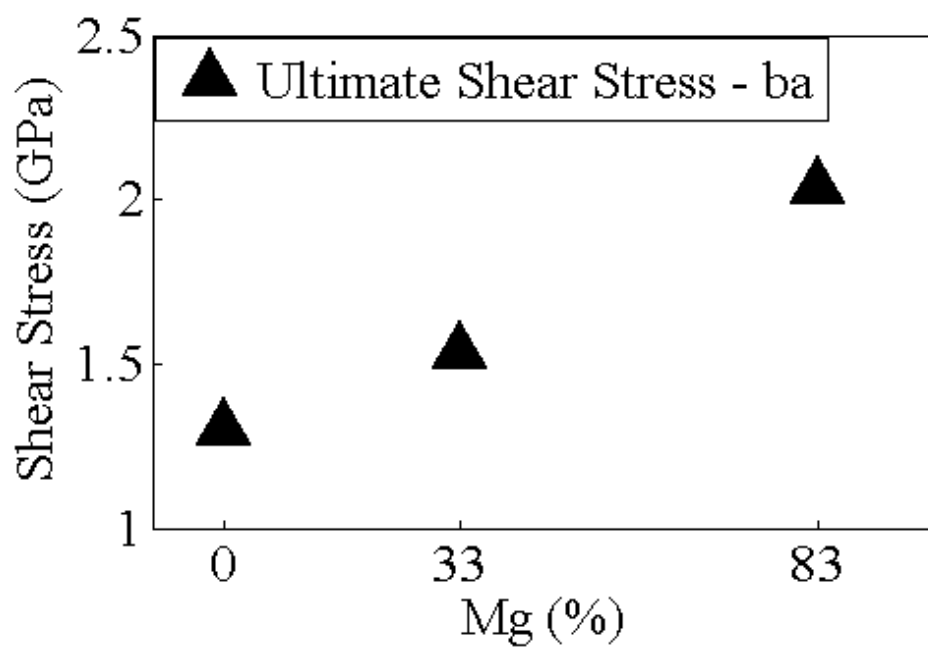


Figure 47. Ultimate shear stress variations due to Mg Ion Exchange, *ba*-plane

4.2.3 Shear deformation, *ac*-plane. Shear stress – strain deformation behavior due to shearing along the crystallographic *ac*-plane is presented in *figures 48-50* for traditional and Magnesium modified C-S-H.

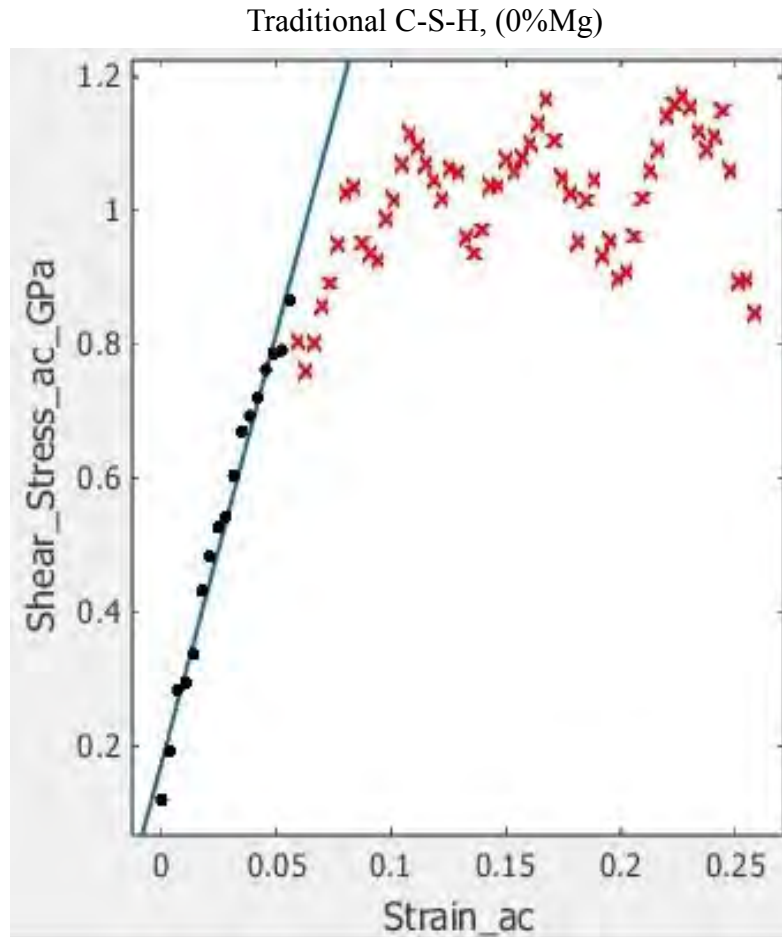


Figure 48. Predicted Shear Stress-strain deformation behavior for shearing along the *ac*-plane for traditional Jennite. Ref [50]

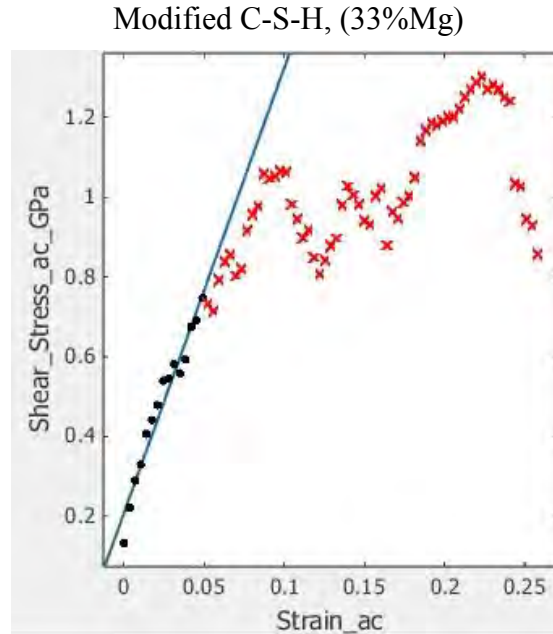


Figure 49. Predicted Shear Stress-strain deformation behavior for shearing along the *ac*-plane for 33% magnesium modified Jennite.

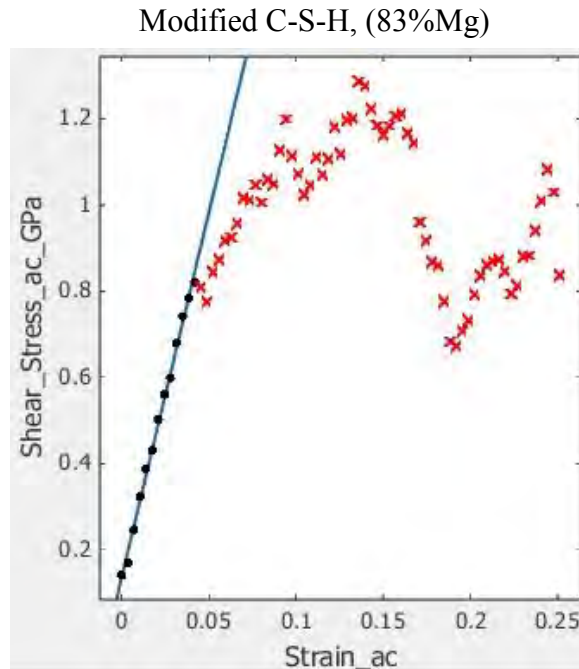


Figure 50. Predicted Shear Stress-strain deformation behavior for shearing along the *ac*-plane for 83% magnesium modified Jennite

The corresponding shear moduli and ultimate shear stress obtained for shear deformation stress – strain curves along *ac*-plane is presented in *figures 51* and *52*.

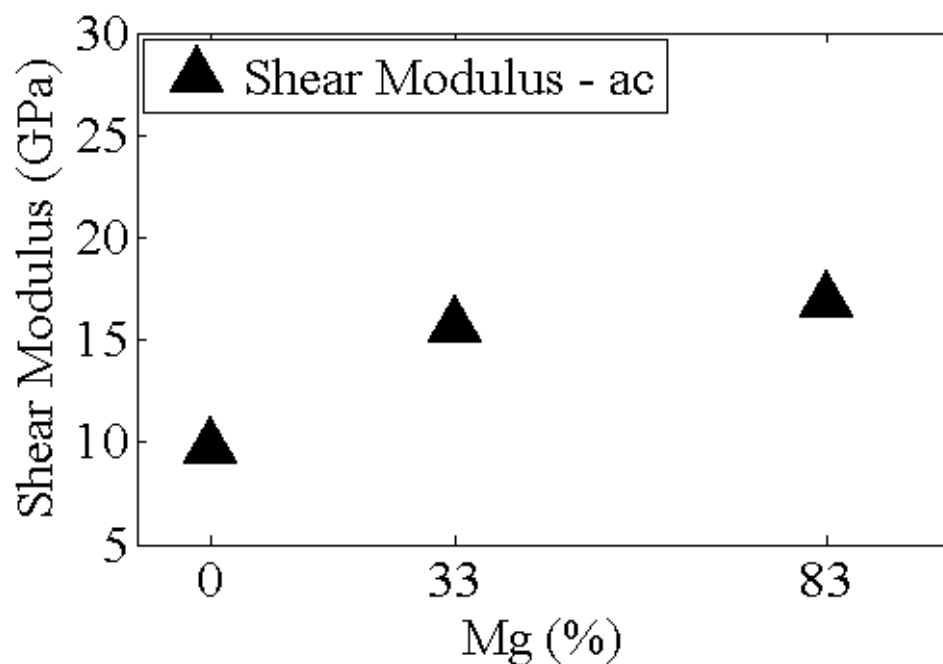


Figure 51. Shear Modulus variations due to Mg Ion Exchange, *ac*-plane

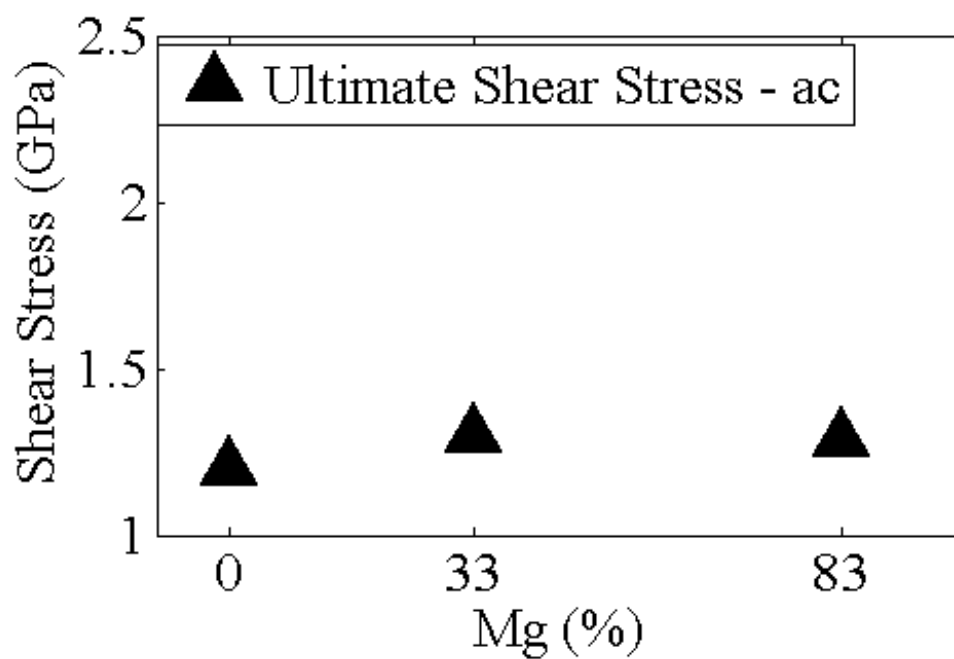


Figure 52. Ultimate shear stress variations due to Mg Ion Exchange, *ac*-plane

4.2.4 Shear deformation analysis results summary. The results discussed earlier from MD material modeling methodology for shear deformation along the three crystallographic planes of triclinic C-S-H structure show the following changes in the predicted material properties.

- Predicted shear modulus for shear deformation along all three crystallographic planes increases as the %Mg increases
- The predicted ultimate shear strength before material failure increases as the %Mg increases

Table 6 summarizes the predicted shear modulus values for shear deformation along the three crystallographic planes of traditional and Magnesium ion exchange modified C-S-H configuration studied. The corresponding ultimate shear strength obtained from the shear deformation behavior along the three crystallographic planes of triclinic C-S-H molecular system is presented in *Table 7*.

Table 6

Predicted Shear Modulus (GPa) all planes

| Shear Modulus (GPa) | | | |
|---------------------|----------|-----------|------------|
| % Mg | 0% | 33% | 83% |
| <i>ac</i> -Plane | 9.7±1.1 | 15.66±1.9 | 16.91±0.7 |
| <i>cb</i> -Plane | 11.0±2.4 | 12.88±1.2 | 18.19±1.75 |
| <i>ba</i> -Plane | 13.1±1.0 | 18.38±0.7 | 27.55±3.6 |

Table 7

Ultimate Shear Stress (GPa) all planes

| Ultimate Shear Stress (GPa) | | | |
|-----------------------------|-----|-------|-------|
| % Mg | 0% | 33% | 83% |
| Plane - ac | 1.2 | 1.302 | 1.287 |
| Plane - cb | 1.1 | 1.275 | 1.48 |
| Plane - ba | 1.3 | 1.536 | 2.038 |

Next section discusses a closer look at the shear deformation process and the atom by atom deformation study. The traditional Jennite and two modified Jennite structure were analyzed below and is required to understand the shear deformation and failure captured in the stress-strain curves.

4.3 Shear Deformation Atom Trajectory Study

The shear deformation response was studied by tracking the positions of the atoms as the deformation proceeds and to observe the movement of each atom as the stress is applied to the structure. In order to do this, the atoms in the initial structure were grouped into 10 different sections or layers. C-S-H molecular structure shows calcium oxide layers with free water and silica chains interspersed between these layers. Each group/section is designated as layers 1 to 10, with the topmost layer being the tenth layer. The location of CaO molecules was used to obtain the centroid of the associated CaO (Ca) molecules. The locations of the centroids of the CaO atoms in a single layer were consequently used to determine the centroid of each layer. In the present analysis, the centroid is independent of the atomic mass of the constituent atoms. So

that when Ca is replaced with Mg, the effect of mass is not taken into account. The displacement each centroid is tracked, as the material is deformed. The actual displacement of the centroid versus strain curves was obtained for each layer. Also a hypothetical linear elastic behavior curve, which assumes that the material continues to behave elastically throughout the strain region was also plotted for each layers. This was done for the traditional Jennite and the 33% and 83% magnesium modified Jennite for all the crystallographic planes. The strain region on the displacement-strain curves where there is non-linear movement of the layer centroid was correlated to the strain region when non-linear deformation starts to manifest in their respective stress-strain curves. The results of *ba*-planes is compared and presented next.

4.3.1 Shear deformation, atom trajectory study, *ba*-plane. The movement of the centroid of each layer along the x-axis as the strain is increased is presented. *Figures 53 and 54* show the displacement-strain curves along the *ba*-plane, for layers 3-6 and layers 7-10 respectively for the traditional Jennite. *Figures 56 and 57* shows the displacement-strain curves for 33 % modified Jennite along the *ba*-plane. Also, *Figures 59 and 60* show those for the 83% modified Jennite, along the *ba*-plane. The figures (53 and 54) also show the hypothetical continued linear displacement behavior of each material with strain as they undergo shear deformation. The hypothetical curve assumes that the material behaves linearly throughout the strain region. The actual/observed behavior is different from the hypothetical behavior, the deformations in most cases follow linear deformation but as the strain level increases, they began to exhibit deviation from the linear behavior. The strain values when there is a significant change in linear to non-linear behavior, depicted by either the change in slope or deviation from the hypothetical curve is observed and compared with the strain values at highest stress in the stress-strain curves.

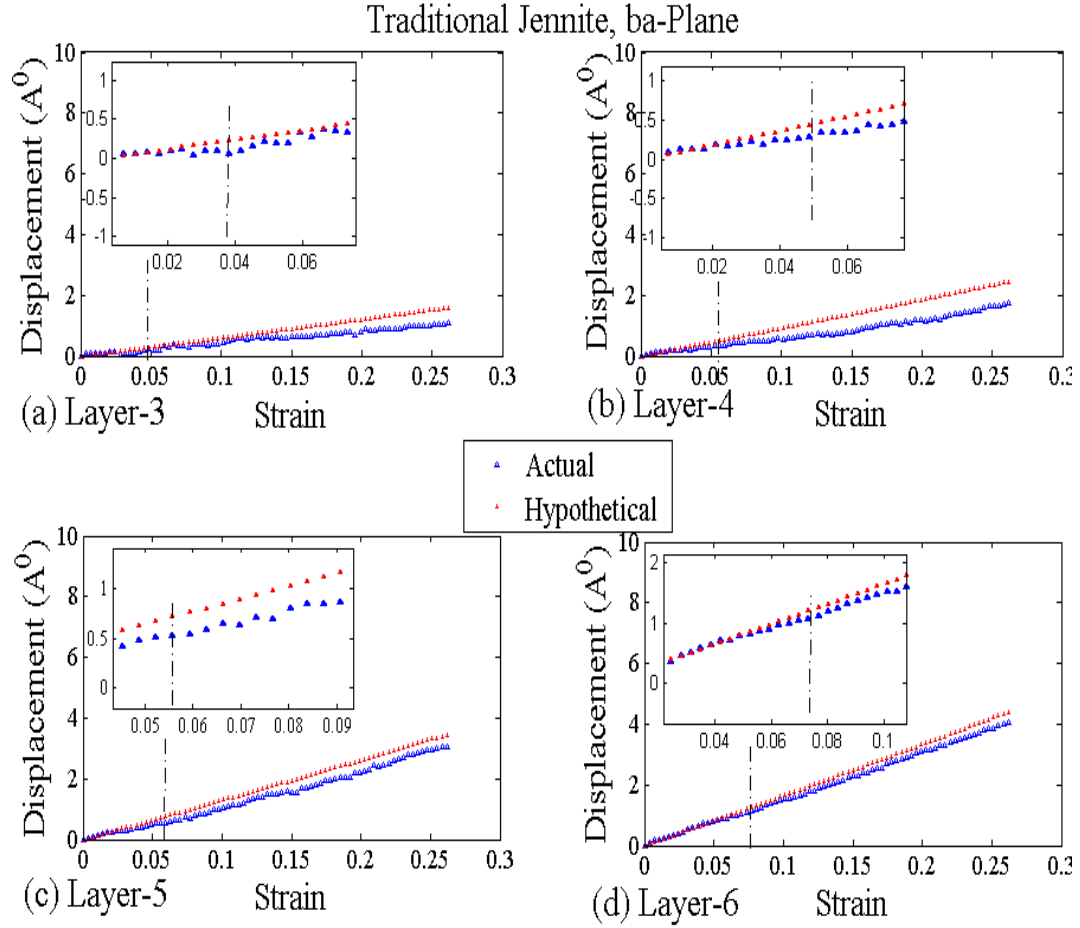


Figure 53. Atomic Centroid Displacement-Strain Curves for Layers 3-6 along x-axis for Traditional Jennite when sheared along *ba*-plane.

From Figures 53 and 54, and as expected, the first few bottom layers (3-5) appear to move only slightly along the x-axis compared to the upper layers (7-9) for all the Jennite types. The atomic centroid movement of the first four layers for all the Jennite appears to move slightly less than the centroids of the topmost six layers.

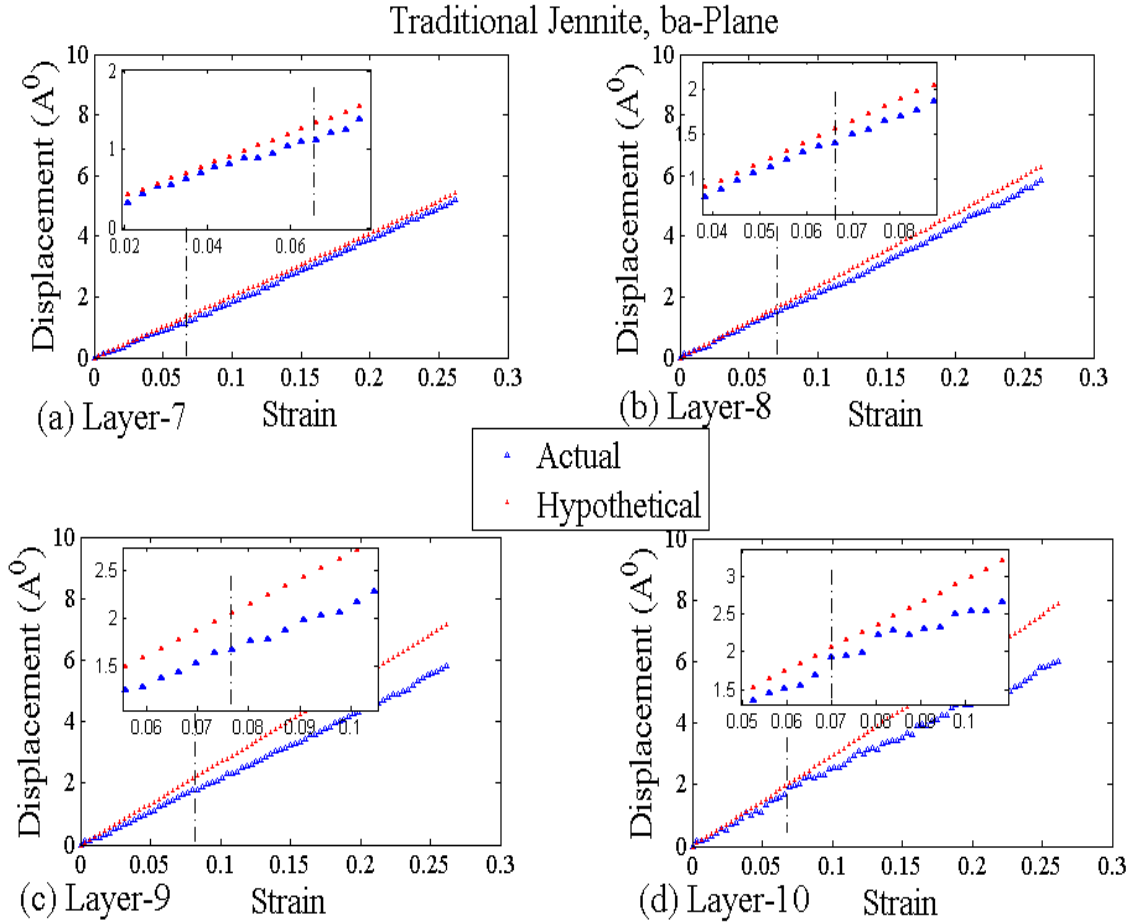


Figure 54. Atomic Centroid Displacement-Strain Curves for Layers 7-10 along x-axis for Traditional Jennite when sheared along ba -plane

The expanded inset in the figures shows vertical lines drawn through the location where the non-linear behavior is found. This is found to be strain of about 0.04 for layer-3. The strain values for layers 4-6 in *Figure 53* are 0.05, 0.055, and 0.075, while those for layers 7-10 in *Figure 54* are: 0.065, 0.068, 0.077 and 0.07. From the stress-strain curve of *figure 55*, the traditional Jennite experiences the highest stress and transition to non-linear behavior within the strain range of 0.04 to about 0.076, this values corresponds to the strain region in the displacement-strain curves (*Figures 53 and 54*) where non-linear displacement of the atom is found.

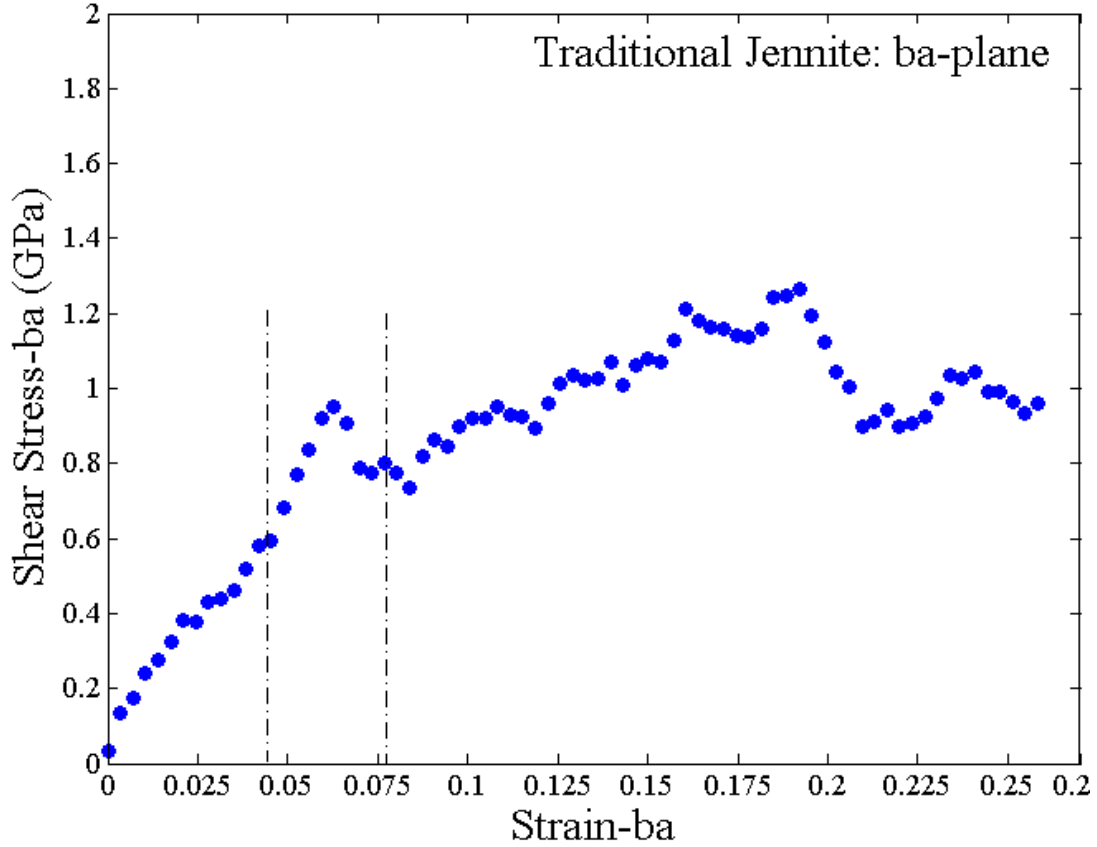


Figure 55. Stress-Strain Curve for Traditional Jennite when sheared along the ba -Plane

This displacement of the atom hence gives the region where the material starts to yield and shows a linear to non-linear transition due to the applied deformation.

Similarly for the 33%Mg modified Jennite, the non-linear deformation starts occurring at a strain between (0.06, 0.055, 0.048, 0.074, 0.07, 0.047, 0.056 and 0.068) for layers 3-10 respectively as depicted in *Figures 56 and 57* below.

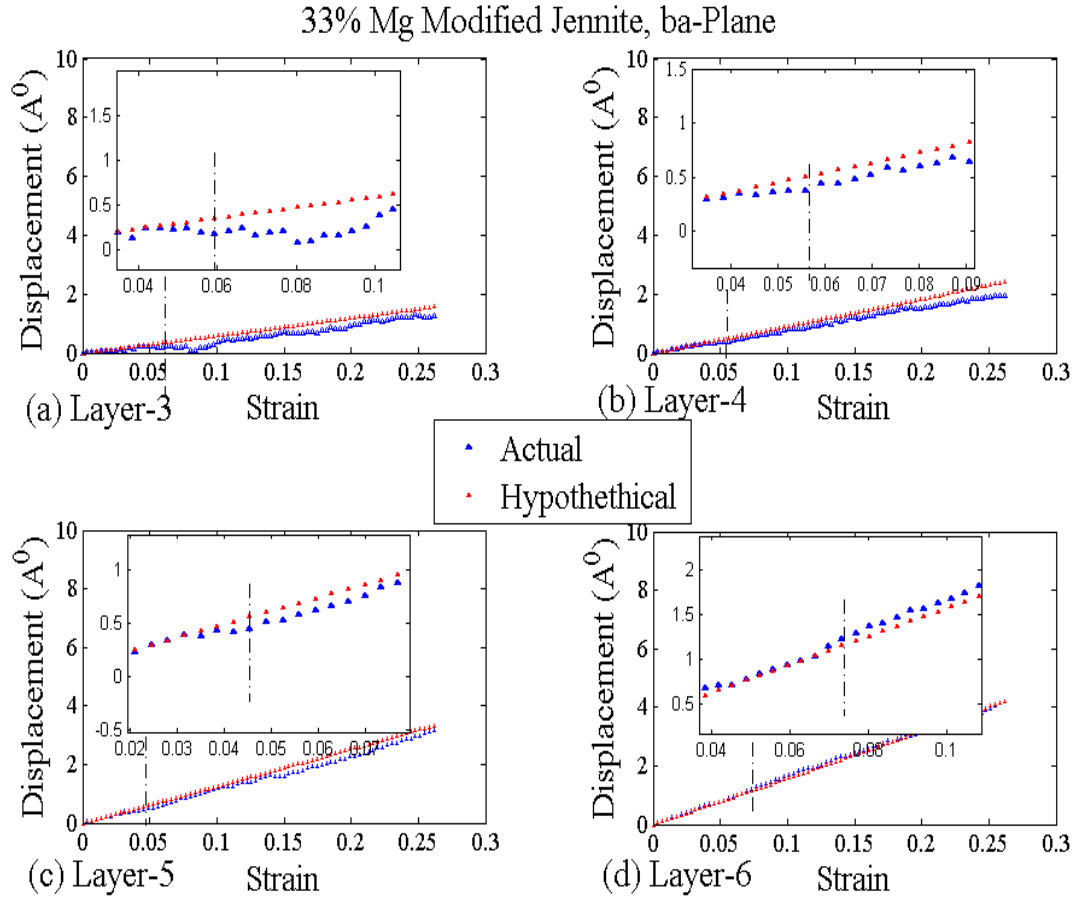


Figure 56. Atomic Centroid Displacement-Strain Curves for Layers 3-6 along x-axis for 33% Magnesium Modified Jennite when sheared along *ba*-plane

The strain values from the displacement-strain curves above were also found to correspond to the strain at the yield region in the stress-strain curve (0.04-0.076) for the *ba*-plane of the 33% modified Jennite as shown in Figure 58.

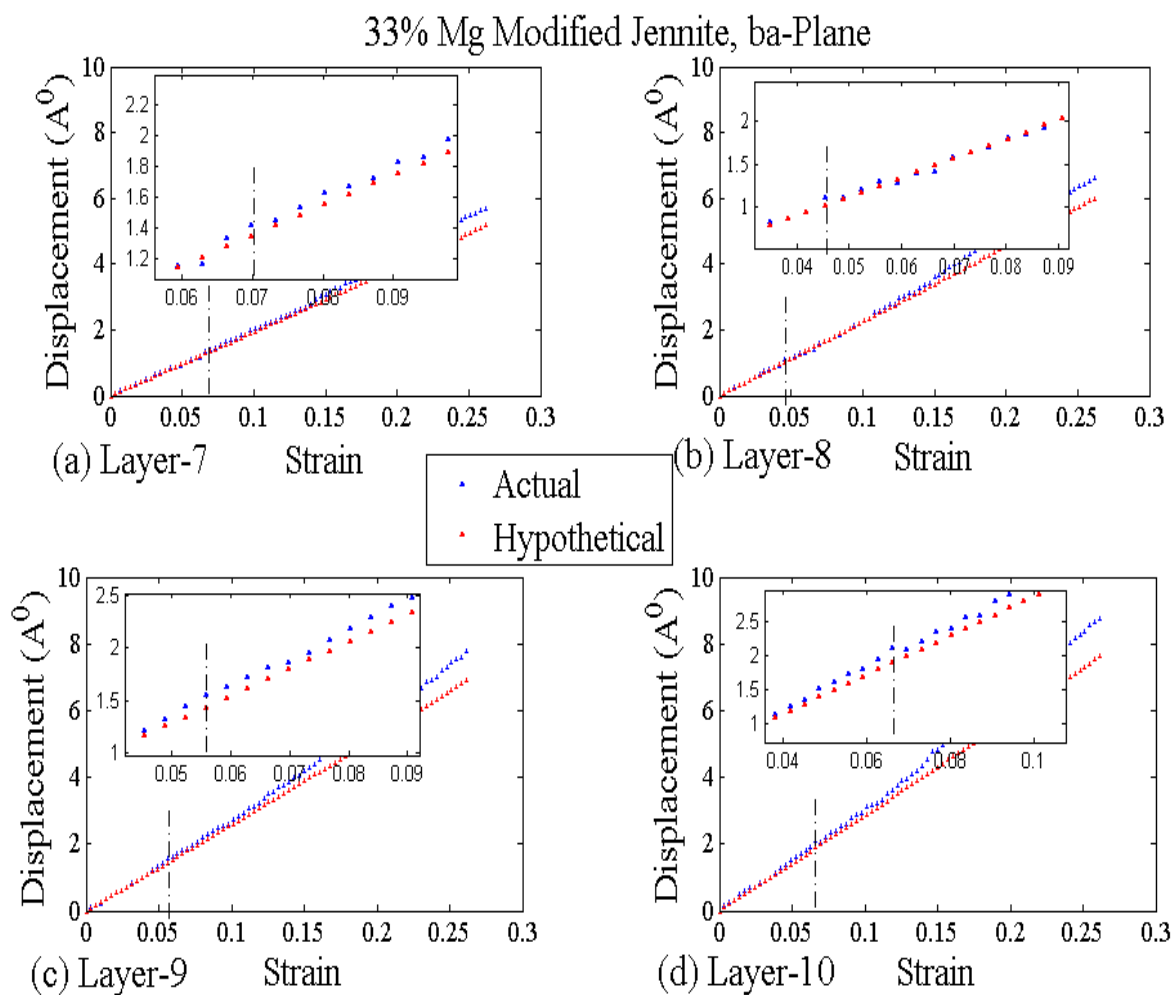


Figure 57. Atomic Centroid Displacement-Strain Curves for Layers 7-10 along *x*-axis for 33% Magnesium Modified Jennite when sheared along *ba*-plane

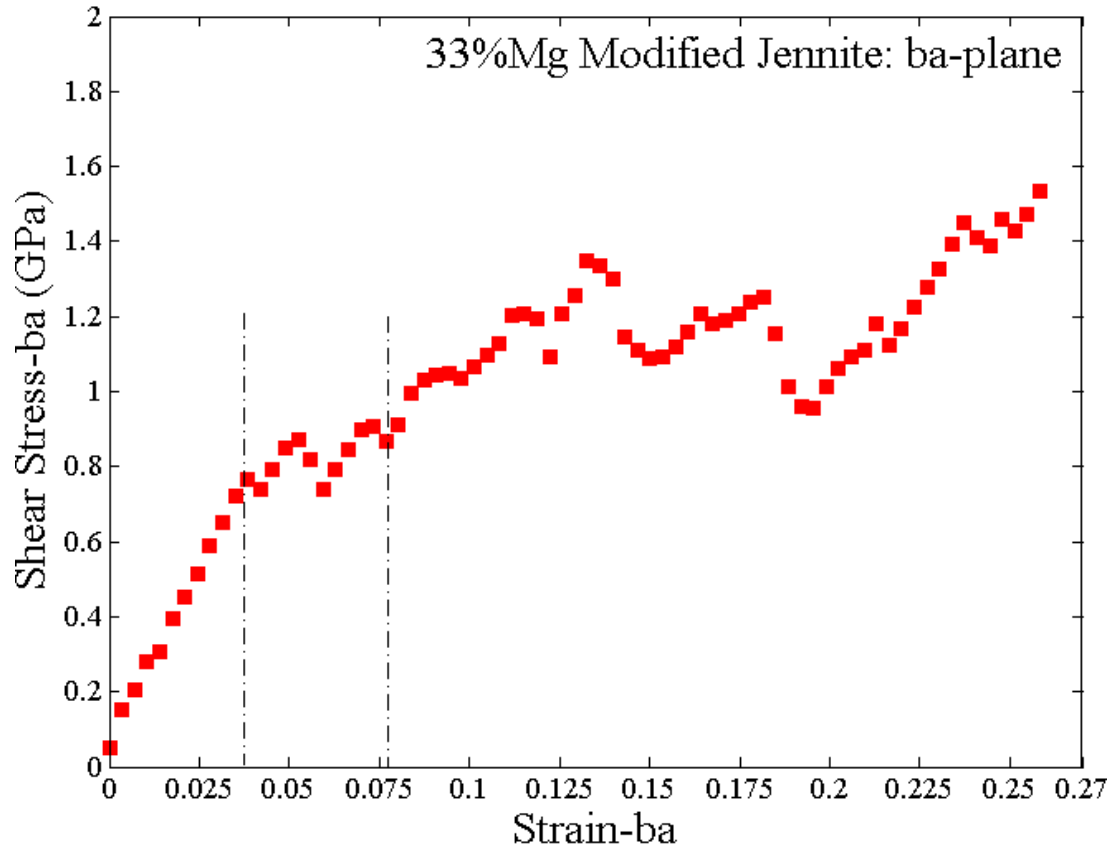


Figure 58. Stress-Strain Curve for 33% Mg Modified Jennite when sheared along the *ba*-Plane

Lastly, 83% traditional Jennite also experience a similar strain values, first there was slight non-linear deformation around values of 0.035-0.05 in most of the layers. However there was a return to linearity before a final non-linear deformation at a later strain values of; 0.055, 0.06, 0.057, 0.07, 0.064, 0.068, 0.07 and 0.08 for layers 3 -10 respectively (*Figures 59 and 60*). The same observation can be noticed in the stress-strain curve as depicted in *Figure 61*.

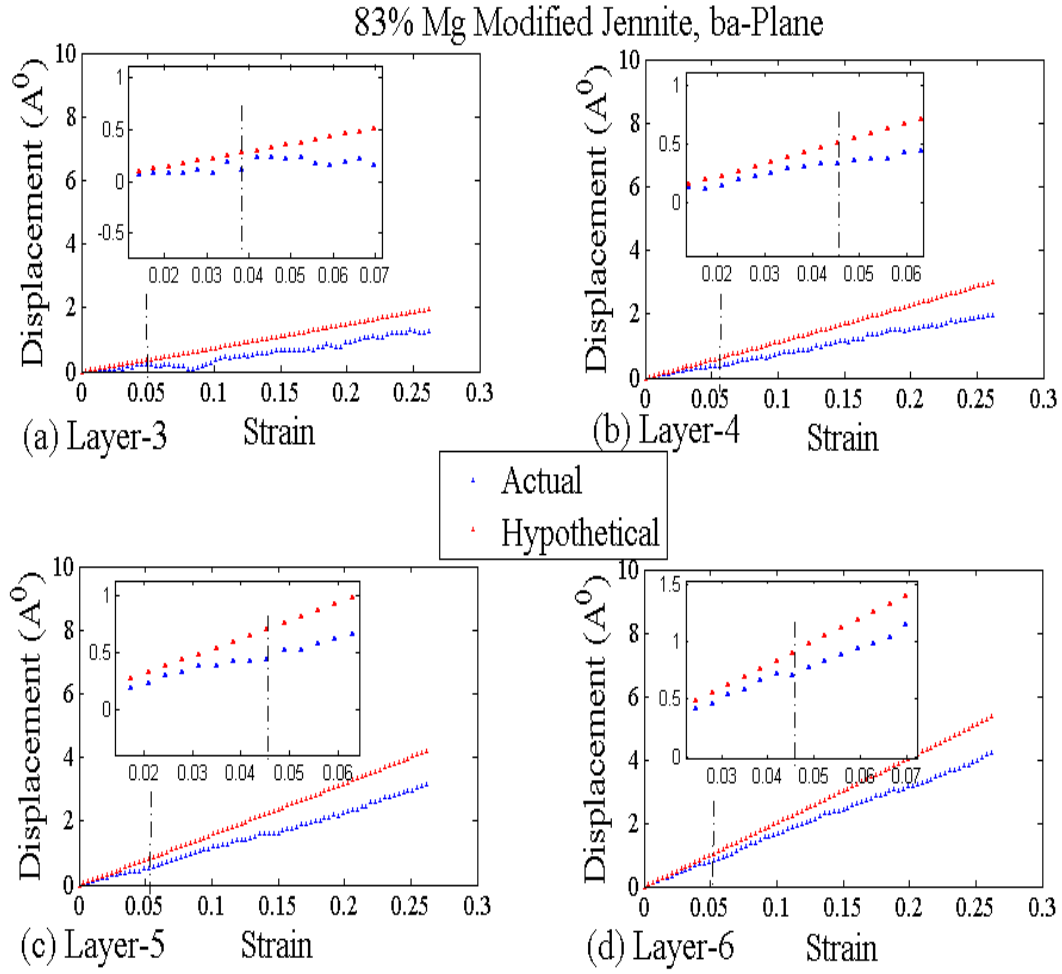


Figure 59. Atomic Centroid Displacement-Strain Curves for Layers 3-6 along *x*-axis for 83% Magnesium Modified Jennite when sheared along *ba*-plane

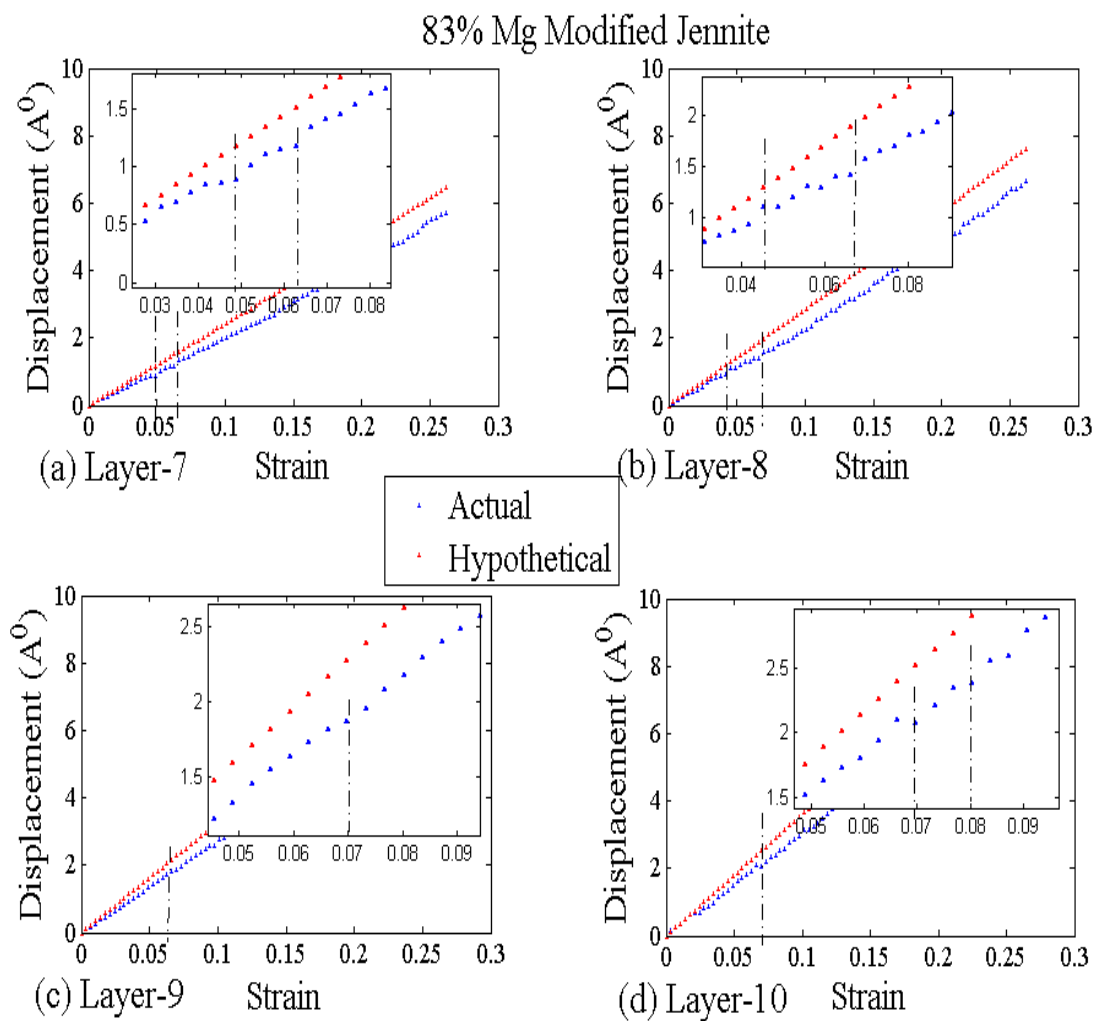


Figure 60. Atomic Centroid Displacement-Strain Curves for Layers 7-10 along x-axis for 83% Magnesium Modified Jennite when sheared along *ba*-plane

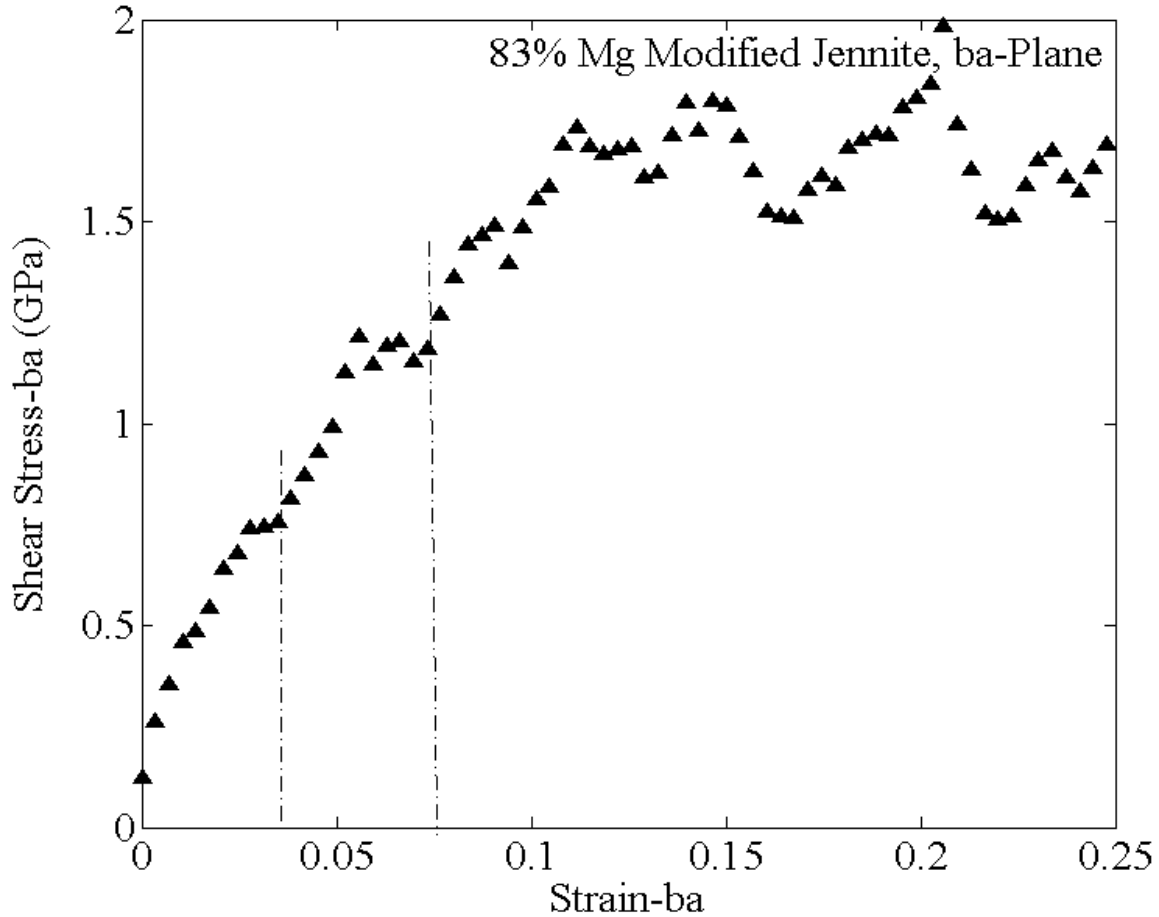


Figure 61. Stress-Strain Curve for 83% Mg Modified Jennite when sheared along the *ba*-Plane

In general, the strain values in the stress strain curve falls between 0.04-0.076, which is similar to those from the displacement strain curve for all the layers considered. From the observations, it can be seen that the movement of the atoms can give information about the strain region where the material starts behaving in-elastically and a transition from linear to non-linear behavior occurs.

The same analyses were done for *cb*-plane and *ac*-plane, the displacement-strain curves for layers 3-10 for 33% Mg modified Jennite for *cb*-plane and 83% Mg modified Jennite for *ac*-plane can be found in Appendices B1 and B2 respectively.

CHAPTER 5

Discussion and Future Research

5.1 Discussion of Results

From the results, we have been able to establish that material chemistry of traditional C-S-H Jennite will be affected by ionic replacement of the Ca ions by Mg ions. By including Magnesium in increasing proportion in the C-S-H Jennite, the total energy of the structure was observed to decrease with the increase in the amount of Magnesium added. By carrying out the computational mechanical stiffness property evaluation on the structures, the elastic modulus of the system structures were determined. It was found to decrease as the amount of Magnesium in the molecular structure increased. COMPASS force field and UNIVERSAL force field tends to describe the same behavior of the total energy of the molecular system, although the values obtained using UNIVERSAL force field were found to be higher. It should be noted that experimental determination of these elastic properties is a complex task. What we have been able to establish here is that material chemistry play important role in the elastic stiffness properties of the C-S-H Jennite structure. The trends have been established by using the two force fields, but there is a need to further improve the fidelity of the elastic stiffness modulus with further studies and comparative verification and validations.

Results obtained from the study of the influence of Magnesium on shear deformation, shows that by deforming the traditional and modified C-S-H Jennite, the shear modulus obtained from the stress-strain curves shows an increasing trend as the amount of Magnesium in the system increases. We refer to the peak stress value of the stress-stress curves as the ultimate shear stress that can be absorbed by the materials within 0.025 strain, and any further deformation results in failure. The ultimate shear stress values were seen to increase as the

amount of Magnesium in the systems increases. We can also establish here that material chemistry definitely affects the engineering scale properties of the cement structure. The present results are based on an assuming that structure of the modified C-S-H Jennite remains triclinic , even though Magnesium ion are smaller than Calcium ions. Present study clearly demonstrated that computational material modeling following molecular dynamics analysis methodology is an effective way to predict and understand the effect of material chemistry, and additive changes on the stiffness and deformation characteristics in cementitious materials. Such methodology is also extendable to others.

5.2 Recommendations for Future Work

Future research should validate the results obtained in the present work by using the other mineral forms of C-S-H Jennite such as Tobermorite 14A⁰. It is also recommended that if computational capacities allows, a larger system size should be used to validate results. Since all results were obtained with material chemistry structure and computational molecular dynamics, future attempts should investigate potential experimental scale relevant validations using nano-indentation and investigate potential methods for low length scale characterization for further validations and comparisons.

References

1. Accelrys. *Engineering New Materials with Nano-Science*. Available from: <http://accelrys.com/events/webinars/webinar-archive.html#materials>.
2. Manzano, H., et al., *Impact of chemical impurities on the crystalline cement clinker phases determined by atomistic simulations*. *Crystal Growth & Design*, 2011. **11**(7): p. 2964-2972.
3. Van Oss, H.G., *Background facts and issues concerning cement and cement data*, 2005.
4. Taylor, H.F., *Cement chemistry*. 1997: Thomas Telford.
5. Mindess, S., J.F. Young, and D. Darwin, *Concrete*. 2003.
6. Nonat, A., *The structure and stoichiometry of CSH*. *Cement and Concrete Research*, 2004. **34**(9): p. 1521-1528.
7. Richardson, I., *The calcium silicate hydrates*. *Cement and Concrete Research*, 2008. **38**(2): p. 137-158.
8. Bernard, O., F.-J. Ulm, and E. Lemarchand, *A multiscale micromechanics-hydration model for the early-age elastic properties of cement-based materials*. *Cement and Concrete Research*, 2003. **33**(9): p. 1293-1309.
9. Zaoui, A., *Continuum micromechanics: survey*. *Journal of Engineering Mechanics*, 2002. **128**(8): p. 808-816.
10. Maekawa, K., T. Ishida, and T. Kishi, *Multi-scale modeling of concrete performance*. *Journal of Advanced Concrete Technology*, 2003. **1**(2): p. 91-126.
11. Martín-Sedeño, M.C., et al., *Aluminum-rich belite sulfoaluminate cements: clinkering and early age hydration*. *Cement and Concrete Research*, 2010. **40**(3): p. 359-369.
12. Hewlett, P., *Lea's chemistry of cement and concrete*. 2003: Butterworth-Heinemann.

13. Stephan, D. and S. Wistuba, *Crystal structure refinement and hydration behaviour of $3\text{CaO} \cdot \text{SiO}_2$ solid solutions with MgO , Al_2O_3 and Fe_2O_3* . Journal of the European Ceramic Society, 2006. 26(1): p. 141-148.
14. Jansang, B., A. Nonat, and J. Skibsted. *Modelling of guest-ion incorporation in the anhydrous calcium silicate phases of Portland cement by periodic density functional theory calculations*. in CONMOD–2010, 3rd RILEM Conference on Concrete Modelling. 2010.
15. Churakov, S.V., *Hydrogen bond connectivity in jennite from ab initio simulations*. Cement and Concrete Research, 2008. 38(12): p. 1359-1364.
16. Bernard, F., S. Kamali-Bernard, and W. Prince, *3D multi-scale modelling of mechanical behaviour of sound and leached mortar*. Cement and Concrete Research, 2008. 38(4): p. 449-458.
17. Nakarai, K., et al., *Enhanced thermodynamic analysis coupled with temperature-dependent microstructures of cement hydrates*. Cement and concrete research, 2007. 37(2): p. 139-150.
18. Grondin, F., et al., *Multi-scales modelling for the behaviour of damaged concrete*. Cement and Concrete Research, 2007. 37(10): p. 1453-1462.
19. Landman, U., *Materials by numbers: Computations as tools of discovery*. Proceedings of the National Academy of Sciences of the United States of America, 2005. 102(19): p. 6671-6678.
20. Griebel, M., S. Knapek, and G. Zumbusch, *Numerical simulation in molecular dynamics*. 2007: Springer.

21. Rapaport, D.C., *The art of molecular dynamics simulation*. 2004: Cambridge university press.
22. Doolen, G.D., *Lattice gas methods: theory, applications, and hardware*. 1991: MIT press.
23. Bird, G.A., *Molecular gas dynamics and the direct simulation of gas flows*. 1994.
24. Maitland, G.C., et al., *Intermolecular forces: their origin and determination*. 1981: Clarendon Press Oxford.
25. Cramer, C.J., *Essentials of computational chemistry: theories and models*. 2013: John Wiley & Sons.
26. Israelachvili, J.N., *Intermolecular and surface forces: revised third edition*. 2011: Academic press.
27. Allen, M.P. and D.J. Tildesley, *Computer simulation of liquids*. 1987.
28. Rappé, A.K., et al., *UFF, a full periodic table force field for molecular mechanics and molecular dynamics simulations*. Journal of the American Chemical Society, 1992. **114**(25): p. 10024-10035.
29. Sun, H., *COMPASS: An ab initio force-field optimized for condensed-phase applications overview with details on alkane and benzene compounds*. The Journal of Physical Chemistry B, 1998. **102**(38): p. 7338-7364.
30. Accelrys, *Materials Studio*, 2012.
31. Hünenberger, P.H., *Thermostat algorithms for molecular dynamics simulations*, in *Advanced Computer Simulation*. 2005, Springer. p. 105-149.
32. Zhao, Y., *Brief introduction to the thermostats*, Tech. Rep. Research-Cerca con Google.

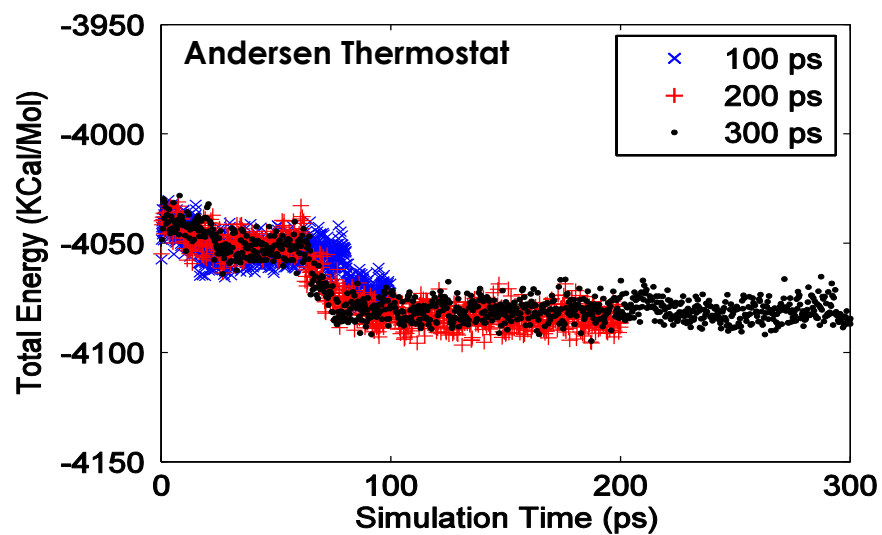
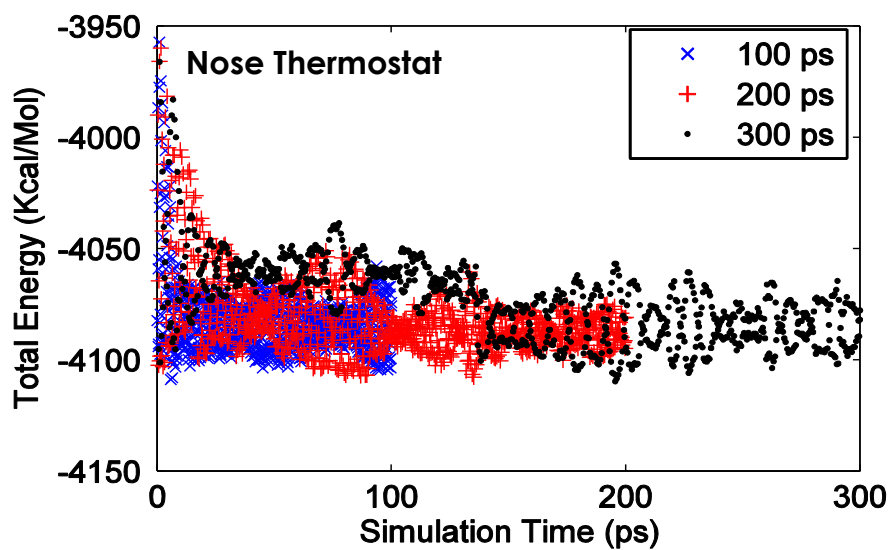
33. Bussi, G. and M. Parrinello, *Stochastic thermostats: comparison of local and global schemes*. Computer Physics Communications, 2008. **179**(1): p. 26-29.
34. Andersen, H.C., *Molecular dynamics simulations at constant pressure and/or temperature*. The Journal of chemical physics, 2008. **72**(4): p. 2384-2393.
35. *Different Ensembles in Molecular Dynamics Simulations*. 3/12/14; Available from: <http://faculty.uml.edu/vbarsegov/teaching/bioinformatics/lectures/MDEnsemblesModified.pdf>.
36. *Simulation of Biomolecules*. 3/11/2014; Available from: <http://www.grs-sim.de/cms/upload/Carlioni/Presentations/Strodel3.pdf>.
37. Nosé, S., *A molecular dynamics method for simulations in the canonical ensemble*. Molecular physics, 1984. **52**(2): p. 255-268.
38. Nosé, S., *A unified formulation of the constant temperature molecular dynamics methods*. The Journal of Chemical Physics, 1984. **81**(1): p. 511-519.
39. Berendsen, H.J., et al., *Molecular dynamics with coupling to an external bath*. The Journal of chemical physics, 1984. **81**(8): p. 3684-3690.
40. Press, W.H., *Numerical recipes 3rd edition: The art of scientific computing*. 2007: Cambridge university press.
41. Born, M., *von Karman Th. Phys. Zeit*, 1912. **13**: p. 297.
42. Frenkel, D. and B. Smit, *Understanding molecular simulation: from algorithms to applications*. Vol. 1. 2001: Academic press.
43. Münster, A., *Statistical thermodynamics*. 1969.

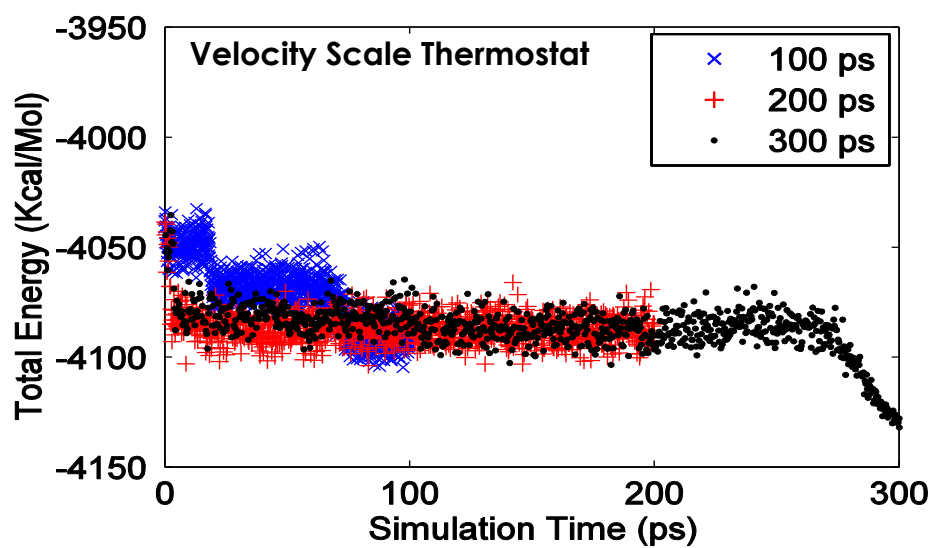
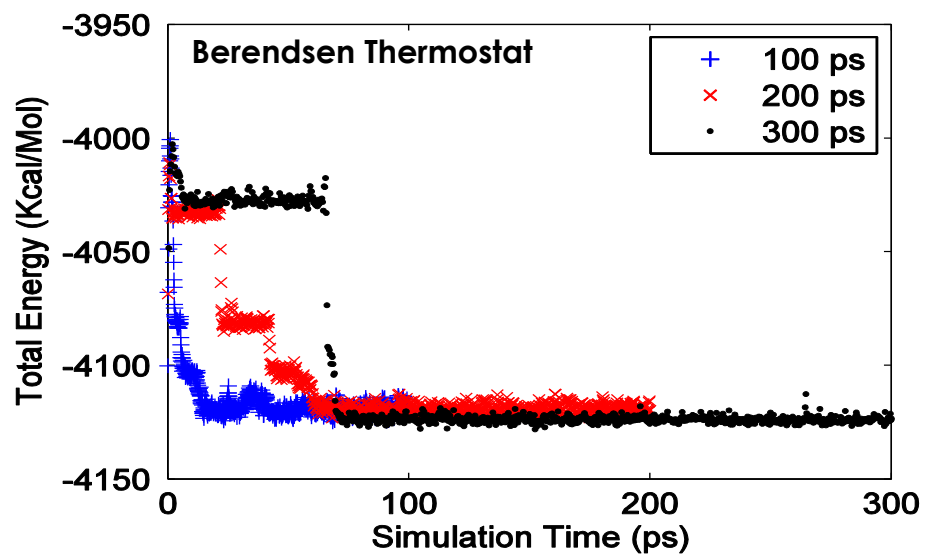
44. Cheung, P., *On the calculation of specific heats, thermal pressure coefficients and compressibilities in molecular dynamics simulations*. Molecular Physics, 1977. **33**(2): p. 519-526.
45. Weiner, J.H., *Statistical mechanics of elasticity*. 2012: Courier Dover Publications.
46. Bland, D.R., *Nonlinear dynamic elasticity*. Vol. 42. 1969: Blaisdell Waltham.
47. Hill, R., *The elastic behaviour of a crystalline aggregate*. Proceedings of the Physical Society. Section A, 1952. **65**(5): p. 349.
48. Beer, F.P., et al., *Mechanics of Materials*. Sixth ed. 2012: McGraw-Hill, New York.
49. Liu, Y., et al., *First principles study the stability and mechanical properties of MC (M= Ti, V, Zr, Nb, Hf and Ta) compounds*. Journal of Alloys and Compounds, 2014. **582**: p. 500-504.
50. Mohamed A, M. Ram, and R. John, 2013.
51. Gard, J. and H. Taylor, *The crystal structure of foshagite*. Acta Crystallographica, 1960. **13**(10): p. 785-793.
52. Posr, J.E., *Crystal structure of hillebrandite: A natural analogue of calcium silicate hydrate (CSH) phases in Portland cement*. American Mineralogist, 1995. **80**: p. 841-844.
53. Hejny, C. and T. Armbruster, *Polytypism in xonotlite $\text{Ca}_6\text{Si}_6\text{O}_{17}(\text{OH})_2$* . Zeitschrift für Kristallographie/International journal for structural, physical, and chemical aspects of crystalline materials, 2001. **216**(7/2001): p. 396-408.
54. Gard, J. and H. Taylor, *Okenite and nekoite (a new mineral)*. Mineral. Mag, 1956. **31**: p. 5-20.

55. MERLINO, S., E. BONACCORSI, and T. ARMBRUSTER, *The real structures of clinotobermorite and tobermorite 9 Å OD character, polytypes, and structural relationships*. European Journal of Mineralogy, 2000. **12**(2): p. 411-429.
56. Henmi, C. and I. Kusachi, *Monoclinic tobermorite from Fuka, Bitchu-cho, Okayama Prefecture, Japan*. J. Min. Petr. Econ. Geol, 1989. **84**: p. 374-379.
57. Merlino, S., E. Bonaccorsi, and T. Armbruster, *Tobermorites: Their real structure and order-disorder (OD) character*. American Mineralogist, 1999. **84**: p. 1613-1621.
58. Merlino, S., E. Bonaccorsi, and T. Armbruster, *The real structure of tobermorite 11 Å normal and anomalous forms, OD character and polytypic modifications*. European Journal of Mineralogy, 2001. **13**(3): p. 577-590.
59. Bonaccorsi, E., S. Merlino, and A.R. Kampf, *The crystal structure of tobermorite 14 Å (plombierite), a C-S-H phase*. Journal of the American Ceramic Society, 2005. **88**(3): p. 505-512.
60. Bonaccorsi, E., S. Merlino, and H. Taylor, *The crystal structure of jennite, $\text{Ca}_9\text{Si}_6\text{O}_{18}(\text{OH})_6 \cdot 8\text{H}_2\text{O}$* . Cement and Concrete Research, 2004. **34**(9): p. 1481-1488.
61. Gard, J., et al., *A reexamination of jennite*. American Mineralogist, 1977. **62**(3-4): p. 365-368.
62. MinDat.org. *Jennite*. [cited 2014; Available from: <http://www.mindat.org/min-2087.html>].
63. Mineralogical-Society-of-America, *Jennite*.

Appendix A1

Energy versus Time for NVT dynamics of 1 unit cell modified Jennite (54.8%Mg) using UNIVERSAL forcefield.





Appendix A2

Spatial location of Calcium atom in Jennite.

| Ca position identity | | | |
|--|----------|----------|----------|
| S/N: Spatial Location of Ca | X | Y | Z |
| 1 | -0.373 | 2.779 | 0.227 |
| 2 | 2.621 | 5.851 | 0.525 |
| 3 | 3.500 | 0.409 | 0.551 |
| 4 | 9.118 | 0.423 | -0.024 |
| 5 | 3.965 | 5.001 | 5.517 |
| 6 | 8.446 | 5.099 | 5.931 |
| 7 | 7.310 | 5.319 | 6.677 |
| 8 | 0.779 | 3.222 | 8.302 |
| 9 | 3.423 | 0.852 | 8.955 |

\

The number of sampled variation based on 95% confidence level

| %Mg | No of Mg | No of Ca | No of possibilities | Sampled size |
|--------|----------|----------|---------------------|--------------|
| 0% | 0 | 9 | ${}^9C_0=1$ | 1 |
| 7.08% | 1 | 8 | ${}^9C_1=9$ | 4 |
| 14.80% | 2 | 7 | ${}^9C_2=36$ | 5 |
| 23.27% | 3 | 6 | ${}^9C_3=84$ | 6 |
| 32.67% | 4 | 5 | ${}^9C_4=126$ | 6 |
| 43.12% | 5 | 4 | ${}^9C_5=126$ | 6 |
| 54.81% | 6 | 3 | ${}^9C_6=84$ | 6 |
| 67.97% | 7 | 2 | ${}^9C_7=36$ | 5 |
| 82.80% | 8 | 1 | ${}^9C_8=9$ | 4 |
| 100% | 9 | 0 | ${}^9C_9=1$ | 1 |

$$SS = \frac{\frac{Z^2 * P * (1-P)}{C^2}}{1 + \frac{\frac{Z^2 * P * (1-P) - 1}{C^2}}{\text{Population Size}}}$$

Appendix A3

The Magnesium modified Jennite, the variants and the mean averages of Total Energies and Elastic stiffness modulus are presented.

| J-14.8%Mg -- 64unit cell structure | | | |
|---|--------------------|------------------------------|---------------|
| Variant Name | Ca replaced | Average TE (Kcal/Mol) | E(GPa) |
| J15-i | 1,5 | -4212.42 | 6.504627 |
| J15-j | 2,6 | -4211.7 | 7.616457 |
| J15-k | 3,7 | -4207.3 | 6.445543 |
| J15-l | 4,8 | -4209.48 | 6.984129 |
| J15-m | 1,9 | -4211.5 | 5.609928 |
| AVERAGE = | | -4210.48 | 6.632137 |
| STD DEV = | | 1.867129 | 0.66163 |

| J-(23.27%Mg) -- 64 unit cell structure | | |
|---|--------------------|------------------------------|
| Variant Name | Ca replaced | Average TE (Kcal/Mol) |
| J23-i | 1,2,4 | -4250.69 |
| J23-j | 1,2,3 | -4247.81 |
| J23-k | 4,6,9 | -4251.55 |
| J23-l | 3,8,9 | -4243.57 |
| J23-m | 4,6,7 | -4241.46 |
| J23-n | 1,5,8 | -4245.6 |
| J23-previous | 2,3,7 | -4246.56 |
| AVERAGE = | | -4246.75 |
| STD DEV = | | 3.363506 |

| J-(32.7%Mg) -- 64 unit cell structure | | | |
|--|--------------------|------------------------------|---------------|
| Variant Name | Ca replaced | Average TE (Kcal/Mol) | E(GPa) |
| J32-i | 1,2,8,6 | -4284.06 | 40.43001 |
| J32-j | 3,5,7,9 | -4274.06 | 45.98485 |
| J32-k | 1,2,4,9 | -4278.11 | 46.72645 |
| J32-l | 3,5,4,8 | -4274.56 | 38.22898 |
| J32-m | 6,7,1,5 | -4280.47 | 41.11704 |
| AVERAGE = | | -4278.25 | 42.49747 |
| STD DEV = | | 3.737928 | 3.299879 |

| J-(43.21%Mg) -- 64 unit cell structure | | | |
|---|--------------------|------------------------------|---------------|
| Variant Name | Ca replaced | Average TE (Kcal/Mol) | E(GPa) |
| J43-i | 1,2,3,4,5 | -4304.306205 | |
| J43-j | 1,3,6,8,9 | -4292.287899 | |
| J43-k | 2,6,7,8,9 | -4301.330568 | |
| J43-l | 1,4,5,6,7 | -4300.503784 | |
| J43-m | 2,3,5,6,8 | -4303.081435 | |
| J43-n | 1,3,4,7,9 | -4302.097487 | 19.60885334 |
| J43-Previous | 2,4,5,6,8 | -4304.86911 | 34.53704037 |
| AVERAGE = | | -4301.210927 | 27.07294686 |
| STD DEV = | | 3.916679392 | 7.464093511 |

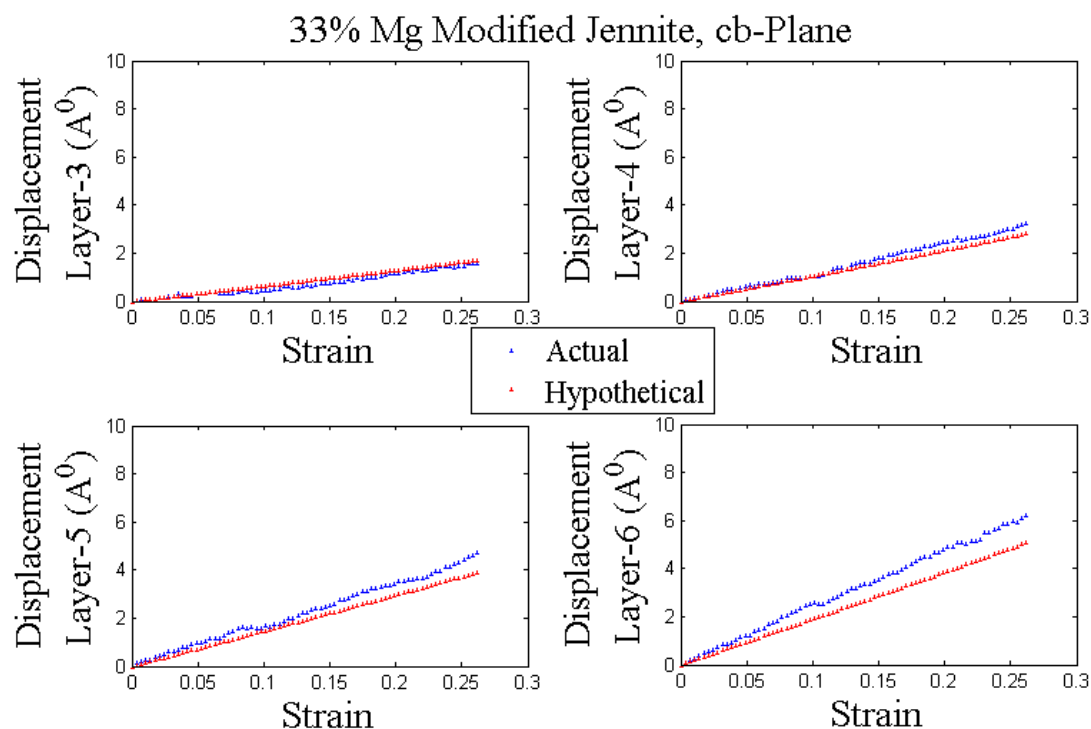
| J-(54.8%Mg) -- 64 unit cell structure | | | |
|--|--------------------|-----------------------------|---------------|
| Variant Name | Ca replaced | Average TE(Kcal/Mol) | E(GPa) |
| J55-i | 1,2,4,7,8,9 | -4328.670814 | 18.21657314 |
| J55-j | 1,2,4,6,8,9 | -4327.079064 | 19.86393489 |
| J55-k | 2,3,5,6,7,9 | -4318.831345 | 19.43865362 |
| J55-l | 1,2,6,7,8,9 | -4329.254849 | 13.69626296 |
| J55-m | 1,3,4,5,7,8 | -4327.839037 | 17.24501927 |
| J55-n | 1,2,4,6,7,9 | -4328.162613 | 24.59421684 |
| AVERAGE = | | -4326.63962 | 18.84244345 |
| STD DEV = | | 3.556345346 | 3.263649791 |

| J-(67.97%Mg) -- 64 unit cell structure | | | |
|---|--------------------|------------------------------|---------------|
| Variant Name | Ca replaced | Average TE (Kcal/Mol) | E(GPa) |
| J68-i | 2,3,4,6,7,8,9 | -4348.358954 | 15.55705204 |
| J68-j | 1,3,4,5,7,8,9 | -4343.537117 | 15.24017854 |
| J68-k | 1,2,3,4,5,6,8 | -4348.308332 | 12.6434633 |
| J68-l | 1,2,4,5,7,8,9 | -4347.734238 | 15.36978749 |
| J68-m | 1,2,3,5,6,7,9 | -4347.420075 | 12.65037346 |
| J68-Previous | 1,2,4,6,7,8,9 | -4345.533912 | 18.05476625 |
| AVERAGE = | | -4346.815438 | 14.91927018 |
| STD DEV = | | 1.742156381 | 1.865084387 |

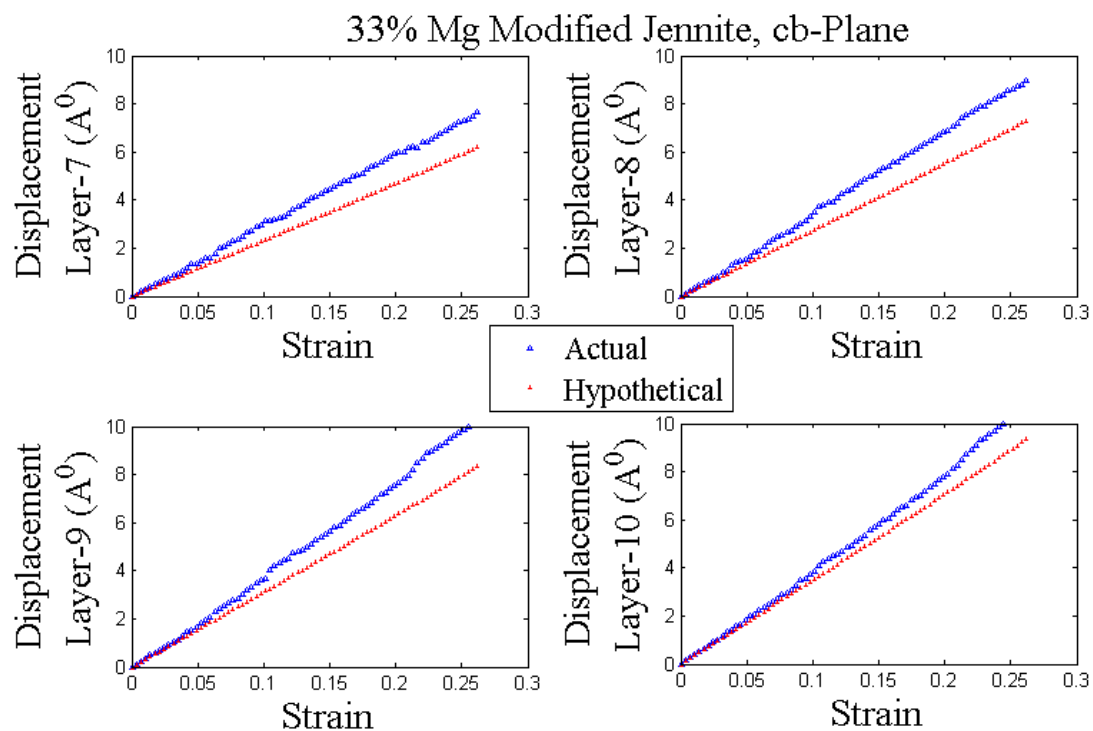
| J-(82.9%Mg) -- 64 unit cell structure | | | |
|--|--------------------|------------------------------|-------------|
| Variant Name | Ca replaced | Average TE (Kcal/Mol) | E |
| J83-i | 2,3,4,5,6,7,8,9 | -4361.005939 | 10.2259845 |
| J83-j | 1,3,4,5,6,7,8,9 | -4361.090475 | 14.53332378 |
| J83-k | 1,2,3,5,6,7,8,9 | -4359.934655 | 14.75545451 |
| J83-l | 1,2,3,4,6,7,8,9 | -4360.238779 | 15.53425973 |
| J83-m | 1,2,3,4,5,6,8,9 | -4359.450767 | 14.1900116 |
| J83-previous | 1,2,4,5,6,7,8,9 | -4361.676025 | 14.3991761 |
| AVERAGE = | | -4360.47814 | 13.9397017 |
| STD DEV = | | 0.802252931 | 1.713958498 |

Appendix B1

Figures showing the atomic centroid displacement-strain curves for layers 3-10 along for 33% Magnesium Modified Jennite when sheared along *cb*-plane.



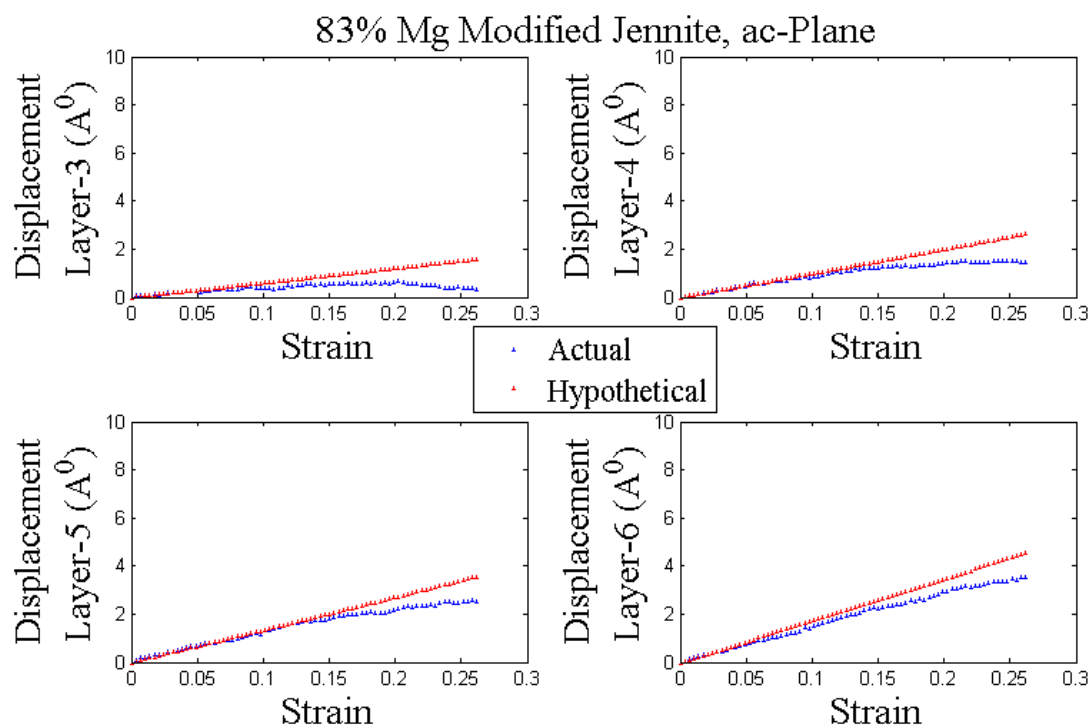
Atomic Centroid Displacement-Strain Curves for Layers 3-6 for 33% Mg modified when sheared along *cb*-plane.



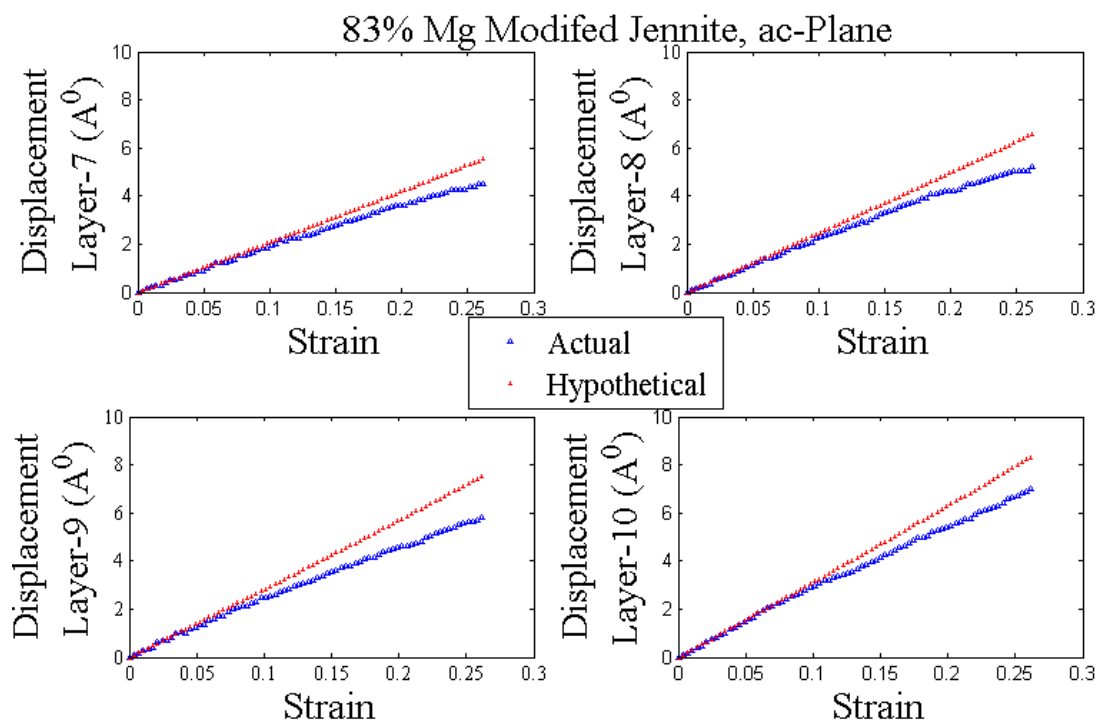
Atomic Centroid Displacement-Strain Curves for Layers 7-10 for 33% Mg modified when sheared along *cb*-plane.

Appendix B2

Figures showing the atomic centroid displacement-strain curves for layers 3-10 along for 83% Magnesium modified Jennite when sheared along *ac*-plane.



Atomic Centroid Displacement-Strain Curves for Layers 3-6 for 83% Mg modified when sheared along *ac*-plane.



Atomic Centroid Displacement-Strain Curves for Layers 7-10 for 83% Mg modified when sheared along *ac*-plane.

*Appendix C1***Shear deformation code**

```
#BIOSYM btcl 3

#

# Input File For Discover Generated By Materials Studio

# Input Client Model Document:

# Job: Disco Dynamics #

autoEcho on

#

# Begin Forcefield Section

begin forcefield = compass

    # Nonbond section:

    forcefield nonbond +separate_coulomb \

    vdw \

        summation_method = ewald \

        ewald_accuracy = 1.e-003 \

        update_width = 3.00 \

    coulomb \

        summation_method = ewald \

        ewald_accuracy = 1.e-003 \

        update_width = 3.00 \

        dielectric_value = 1.0000

# End Forcefield Section

#Stage Name: minimize
```

```

minimize \
    iteration_limit = 1000 \
execute frequency = 10 \
command = (print output +energy_summary)

# Dynamics Section: NPT equilibration
minimize
dynamics \
time = 100000.00 \
timestep = 1.00 \
ensemble = NPT \
temperature = 298.00 \
    press_choice = stress \
sxx = -0.00003 \
syy = -0.00003 \
szz = -0.00003 \
deviation = 5000.00 \
execute frequency = 100.00 \
command = (print table file = uc64-SbaNPT.tbl +average +batch_average batch_size = 100 +cell
+energy +state +stress +strain) \
execute frequency = 1000.00 \
command = (print archive filename = uc64-SbaNPT.arc +coordinates) \
execute frequency = 1000.00 \
command = (writeFile dynamics_restart filename = uc64-SbaNPT.xdyn)
writeFile coordinate filename = uc64-SbaNPT.car

```

```

# Cell parameters

set cP_list [cellParameter]

set cP_a [lindex $cP_list 0]

set cP_b [lindex $cP_list 1]

set cP_c [lindex $cP_list 2]

set cP_alpha [lindex $cP_list 3]

set cP_beta [lindex $cP_list 4]

set cP_gamma [lindex $cP_list 5]

$a = $cP_a

$b = $cP_b

$c = $cP_c

$alpha = $cP_alpha

$beta = $cP_beta

$gamma = $cP_gamma


$pi = 16.0*atan(1.0/5.0) - 4*atan(1.0/239.0)

$Calp = cos($alpha*$pi/180)

$Cbet = cos($beta*$pi/180)

$Cgam = cos($gamma*$pi/180)

$vol0 = $a*$b*$c*sqrt(1-$Calp*$Calp-$Cbet*$Cbet-$Cgam*$Cgam+2*$Calp*$Cbet*$Cgam)


# Deformation of the system

for (set i 1) ($i <= 75) (incr i 1) (

    $gamma = $gamma+0.2

    $Cgam = cos($gamma*$pi/180)

    $b = $vol0/($a*$c*sqrt(1-$Calp*$Calp-$Cbet*$Cbet-$Cgam*$Cgam+2*$Calp*$Cbet*$Cgam))

```

```
cellParameter $a $b $c $alpha $beta $gamma
```

```
writeFile coordinate filename = uc64-SbaNVT_def_$i.car
```

```
    # Dynamics Section: NVT equilibration
```

```
minimize
```

```
dynamics \
```

```
time = 10000.00 \
```

```
timestep = 1.00 \
```

```
    initial_temperature = 298.00 \
```

```
ensemble = NVT \
```

```
temperature = 298.00 \
```

```
deviation = 50000.00 \
```

```
execute frequency = 10.00 \
```

```
command = (print table file = uc64-SbaNVT_$i.tbl +average +batch_average batch_size = 10 +cell  
+energy +state +stress +strain) \
```

```
execute frequency = 100.00 \
```

```
command = (print archive filename = uc64-SbaNVT_$i.arc +coordinates) \
```

```
execute frequency = 100.00 \
```

```
command = (writeFile dynamics_restart filename = uc64-SbaNVT_$i.xdyn)
```

```
writeFile coordinate filename = uc64-SbaNVT_dyn_$i.car
```

```
)
```


Appendix C2

```

%% COMPILE ALL THE DATA CORRESPONDING TO THE INDIVIDUAL TRAJ.AC

clc; clear; close all;

set(0,'DefaultFigureWindowStyle','docked');

natoms = 68*64;           % THIS VALUE MUST BE AJUSTED FOR EACH SYSTEM

endoftext = 6537;

nmbofrows = 1000;

nmbofcolms = 51;

avedata = zeros(70,27);

for ii=1:75

filename = sprintf('../Sh64J8Sac/uc64-SacNVT_%d.tbl',ii);

fid = fopen(filename);

    tmp1 = fscanf(fid,'%c',endoftext);

tmpdata = zeros(nmbofrows,nmbofcolms);

data = zeros(nmbofrows,26);

%FROM MATERIALS STUDIO [1.timestep (even).RunningAve (odd).BatchAve]

%[1.timestep 2/3.TotalEnr 4/5.KinEnr 6/7.PotEnr 8/9.Temp 10/11.Press

%12/13.Dens 14/15.Vol 16/17.a 18/19.b 20/21.c 22/23.alpha 24/25.beta

%26/27.gamma 28/29.Sxx 30/31.Syy 32/33.Szz 34/35.Syz 36/37.Sxz

%38/39.Sxy 40/41.exx 42/43.eyy 44/45.ezz 46/47.eyz 48/49.exz 50/51.exy]

for i=1:nmbofrows

tmpdata(i,:) = fscanf(fid,'%g',[1 nmbofcolms]);

end

fid = fclose(fid);

%Selecting only the BATCH data (Odd columns)

%[1.timestep 2.TotalEnr 3.KinEnr 4.PotEnr 5.Temp 6.Press 7.Dens 8.Vol

%9.a 10.b 11.c 12.alpha 13.beta 14.gamma 15.Sxx 16.Syy 17.Szz 18.Syz

%19.Sxz 20.Sxy 21.exx 22.eyy 23.ezz 24.eyz 25.exz 26.exy 27.stn]

```

```

data(:,1) = tmpdata(:,1);

for i=2:26

data(:,i) = tmpdata(:,2*i-1);

end

%Changing the sign of the stress values. Accordint to AM

data(:,15:20) = (-1.0)*data(:,15:20);

%Normalization of extensive quantities (Energies)

data(:,2) = data(:,2)/natoms;

data(:,3) = data(:,3)/natoms;

data(:,4) = data(:,4)/natoms;


%Plots for the energy of current trajectory

    figure(ii); plot(data(:,1),data(:,2),'ko','MarkerSize',3);

tmp = mean(data(:,2)); axis([0 10e3 (tmp+0.025*tmp) (tmp-0.025*tmp)]);

xlabel('time [fs]'); ylabel(sprintf('Energy traj. %d',ii));


%AVERAGES FOR EACH DEFORMATION STEP

    n = size(data,1);

    if (ii==1)

avedata(ii,1) = data(n,1)/1000; %Divide by 1000 to plot in [ps]

    else

avedata(ii,1) = data(n,1)/1000 + avedata(ii-1,1);

    end

avedata(ii,2:26) = mean(data(101:1000,2:26));

    end

closeall;

for i=2:26

    figure(i); hold on; plot(avedata(:,1),avedata(:,i),'ko','MarkerSize',3);

```

```

xlabel('time [ps]'); ylabel(sprintf('avedata(%d)',i));

switch i

case 2; ylabel('E [GPa]');

case 8

tmp = mean(data(:,8)); axis([0 800 (tmp-0.025*tmp) (tmp+0.025*tmp)]);
ylabel('Volume');

case 15

ylabel('Sxx [GPa]');

saveas(gcf,'Sxx-t','eps'); saveas(gcf,'Sxx-t','png');

case 16

ylabel('Syy [GPa]');

saveas(gcf,'Sy-t','eps'); saveas(gcf,'Syy-t','png');

case 17

ylabel('Szz [GPa]');

saveas(gcf,'Szz-t','eps'); saveas(gcf,'Szz-t','png');

case 18

ylabel('Syz [GPa]');

saveas(gcf,'Syz-t','eps'); saveas(gcf,'Syz-t','png');

case 19

ylabel('Sxz [GPa]');

saveas(gcf,'Sxz-t','eps'); saveas(gcf,'Sxz-t','png');

case 20

ylabel('Sxy [GPa]');

saveas(gcf,'Sxy-t','eps'); saveas(gcf,'Sxy-t','png');

end

end

% SHEAR STRAIN (ac)

```

```

avedata(:,27) = (avedata(:,13)-avedata(1,13))*pi/180;

%% PLOT THE DATA OF INTEREST

% FOR THE (beta,a) SHEARING SYSTEM: tau(ac) vs. gamma(ac)

figure (27); hold on; set(gca,'LineWidth',2.0); set(gca,'FontSize',18);
plot(avedata(:,27),avedata(:,2),'ko','MarkerSize',4,'MarkerFaceColor','k');
axis ([0 0.3 -69.6 -69.3]);

%title('Total energy vs. Shear strain, \gamma_{ac}','FontSize',22);
xlabel('\gamma_{ac}','FontSize',22,'LineWidth',2.5);
ylabel('E [kcal*mol^{(-1)}'],'FontSize',22,'LineWidth',2.5);
saveas(gcf,'uc64-Eac-stn','eps'); saveas(gcf,'uc64-Eac-stn','png');

% TRACTION ON a PLANE

alp = avedata(1,12); bet = avedata(1,13); gam = avedata(1,14);
nor = [1 0 0];

drt = [cosd(bet) cosd(alp)*sind(gam) sqrt(1 - (cosd(bet))^2 -
(cosd(alp)*sind(gam))^2)];

n = size(avedata(:,1),1);
tra = zeros(n,3); %(x y z)

% from avedata: [15.Sxx 16.Syy 17.Szz 18.Syz 19.Sxz 20.Sxy]
for i=1:n
    tra(i,1) = avedata(i,15)*nor(1) + avedata(i,20)*nor(2) +
avedata(i,19)*nor(3);

    tra(i,2) = avedata(i,20)*nor(1) + avedata(i,16)*nor(2) +
avedata(i,18)*nor(3);

    tra(i,3) = avedata(i,19)*nor(1) + avedata(i,18)*nor(2) +
avedata(i,17)*nor(3);
end

```

```

% shear (ac): component of the traction on plane a along c-dir: (tra*c)

shr = zeros(n,1);

for i=1:n
    shr(i) = tra(i,1)*drt(1) + tra(i,2)*drt(2) + tra(i,3)*drt(3);
end

figure (28); hold on; set(gca,'LineWidth',2.0); set(gca,'FontSize',18);
plot(avedata(:,27),shr,'ko','MarkerSize',4,'MarkerFaceColor','k');
axis ([0 .3 min(shr)-0.25 max(shr)+0.25]);
%title('Shear stress (ac) vs. Shear strain (ac)','FontSize',22);
xlabel('\gamma_{ac}','FontSize',22,'LineWidth',2.5);
ylabel('\tau_{ac} [GPa]','FontSize',22,'LineWidth',2.5);
saveas(gcf,'uc64-Sac-stn','eps'); saveas(gcf,'uc64-Sac-stn','png');

figure (29); hold on; set(gca,'LineWidth',2.0); set(gca,'FontSize',18);
plot(avedata(:,27),shr,'ko','MarkerSize',4,'MarkerFaceColor','k');
plot(avedata(:,27),avedata(:,19),'ko','MarkerSize',4,'MarkerFaceColor','y');
axis ([0 .3 min(shr)-0.25 max(shr)+0.25]);
%title('Shear stress (ac) vs. Shear strain (ac)','FontSize',22);
xlabel('\gamma_{ac}','FontSize',22,'LineWidth',2.5);
ylabel('\tau [GPa] ','FontSize',22,'LineWidth',2.5);
legend(gca,'\tau_{ac}','\tau_{xz}','Location','NorthWest');
saveas(gcf,'uc64-SacSxz-stn','eps'); saveas(gcf,'uc64-SacSxz-stn','png');

```